

Synthesis of molybdenum-based catalysts on carbon support for partial  
hydrogenation reaction of biodiesel



A Thesis Submitted in Partial Fulfillment of the Requirements  
for the Degree of Master of Engineering in Chemical Engineering

Department of Chemical Engineering

FACULTY OF ENGINEERING

Chulalongkorn University

Academic Year 2019

Copyright of Chulalongkorn University

การสังเคราะห์ตัวเร่งปฏิกิริยาที่มีองค์ประกอบของโมลิบดีนัมบนตัวรองรับคาร์บอนเพื่อใช้ในปฏิกิริยา  
พาร์เซียลไฮโดรจิเนชันของไปโอดีเซล



วิทยานิพนธ์นี้เป็นส่วนหนึ่งของการศึกษาตามหลักสูตรปริญญาวิศวกรรมศาสตรมหาบัณฑิต  
สาขาวิชาวิศวกรรมเคมี ภาควิชาวิศวกรรมเคมี  
คณะวิศวกรรมศาสตร์ จุฬาลงกรณ์มหาวิทยาลัย  
ปีการศึกษา 2562  
ลิขสิทธิ์ของจุฬาลงกรณ์มหาวิทยาลัย



ดลฤดี จารุวัฒน์ : การสังเคราะห์ตัวเร่งปฏิกิริยาที่มีองค์ประกอบของโมลิบดีนัมบนตัวรองรับคาร์บอนเพื่อใช้ในปฏิกิริยาพาร์เซียลไฮโดรจีเนชันของไบโอดีเซล. ( Synthesis of molybdenum-based catalysts on carbon support for partial hydrogenation reaction of biodiesel) อ.ที่ปรึกษาหลัก : ศ. ดร.สุทธิชัย อัสสะบารุงรัตน์, อ.ที่ปรึกษาร่วม : ดร.สุมิตรา จรสรโรจน์กุล, ผศ. ดร.อภิรักษ์ณ์ เอียดเอื้อ

ในปัจจุบันไบโอดีเซลเป็นพลังงานทางเลือกที่ใช้ทดแทนเชื้อเพลิงฟอสซิลเป็นจำนวนมาก กระบวนการพาร์เซียลไฮโดรจีเนชันเป็นหนึ่งในกระบวนการที่ใช้เพิ่มคุณภาพของน้ำมันไบโอดีเซล ในงานวิจัยนี้ได้ทำการผลิตตัวรองรับถ่านกัมมันต์จากไบโอดีเซลด้วยกระบวนการไฮโดรเทอร์มัลคาร์บอนไนเซชันและกระบวนการกระตุ้นทางเคมี ถ่านกัมมันต์ที่ได้มีพื้นผิวสูง 1323.38 ตารางเมตรต่อกรัม ซึ่งได้จากกระบวนการกระตุ้นด้วยโพแทสเซียมไฮดรอกไซด์ที่มีความเข้มข้น 4 โมลาร์ ที่อุณหภูมิ 900 องศาเซลเซียส งานวิจัยนี้ทำการศึกษาชนิดตัวเร่งปฏิกิริยาโมลิบดีนัม นิกเกิล คอปเปอร์ เหล็ก โมลิบดีนัม-นิกเกิล โมลิบดีนัม-คอปเปอร์ โมลิบดีนัม-เหล็ก โดยตัวเร่งปฏิกิริยาถูกเตรียมด้วยกระบวนการกลั่นระเหยภายใต้สุญญากาศ จากการทดลองพบว่าตัวเร่งปฏิกิริยาโมลิบดีนัม-นิกเกิลมีการกระจายตัวของอนุภาคโลหะมากที่สุด เมื่อทำการทดสอบตัวเร่งปฏิกิริยาไปใช้ในกระบวนการพาร์เซียลไฮโดรจีเนชันของน้ำมันไบโอดีเซลถั่วเหลืองที่อุณหภูมิ 100 องศาเซลเซียส ความดัน 4 บาร์ พบว่าตัวเร่งปฏิกิริยาโมลิบดีนัม-นิกเกิลบนตัวรองรับคาร์บอนมีความสามารถในการทำปฏิกิริยาสูงสุด โดยมีค่าการแปลงกรดไขมันชนิดไม่อิ่มตัวที่มีพันธะคู่ 2 และ 3 ตำแหน่ง 19 เปอร์เซ็นต์ หลังจากการทำปฏิกิริยาสามารถเพิ่มค่าความเสถียรการเกิดออกซิเดชันของน้ำมันเป็น 14.56 ชั่วโมง นอกจากนี้ จุดหมอกและจุดไหลเทมีค่า 13 และ 10 องศาเซลเซียส ตามลำดับ

สาขาวิชา วิศวกรรมเคมี  
ปีการศึกษา 2562

ลายมือชื่อนิสิต .....

ลายมือชื่อ อ.ที่ปรึกษาหลัก .....

ลายมือชื่อ อ.ที่ปรึกษาร่วม .....

ลายมือชื่อ อ.ที่ปรึกษาร่วม .....

# # 6170172521 : MAJOR CHEMICAL ENGINEERING

KEYWORD: Activation, Hydrothermal carbonization, Catalyst, Cattail leave,  
Partial hydrogenation, Biodiesel, Activated carbon

Dolrudee Jaruwat : Synthesis of molybdenum-based catalysts on carbon support for partial hydrogenation reaction of biodiesel. Advisor: Prof. SUTTICHAJ ASSABUMRUNGRAT, Ph.D. Co-advisor: Sumittra Charojrochkul, Ph.D., Asst. Prof. APILUCK EIAD-UA, Ph.D.

Nowadays, biodiesel is a renewable energy, which can decrease fossil fuel. It helped reducing air pollution. Partial Hydrogenation is one process which improves the biodiesel quality. In this research, activated carbon was produced from cattail leave via hydrothermal carbonization and chemical activation. The activated carbon was treated with 4 M of potassium hydroxide at 900°C, which exhibits 1323.38 m<sup>2</sup>g<sup>-1</sup> of S<sub>BET</sub>. Several type of catalysts (Mo, Ni, Cu, Fe, MoNi, MoCu, and MoFe) were studied in this research, which were prepared using a rotary evaporation technique. The experiments reveal that MoNi/C catalyst indicate the highest dispersion of metal particle. The catalyst performance was evaluated by partial hydrogenation of soybean FAME, 100°C and 4 bar. MoNi/C catalyst provided the best activity, which exhibits 19% conversion of C18:2 and C18:3 with less trans-C18:1 and C18:0. The oxidation stability was less after the hydrogenation of reaction, it was found to increase by 14.56 h. Moreover, the cold flow properties were determined in which the cloud point was 13 °C and the pour point was 10 °C.

Field of Study: Chemical Engineering

Academic Year: 2019

Student's Signature .....

Advisor's Signature .....

Co-advisor's Signature .....

Co-advisor's Signature .....

## ACKNOWLEDGEMENTS

Firstly, I would like to thank the Department of Chemical Engineering, Chulalongkorn University, College of Nanotechnology, King Mongkut's Institute of Technology Ladkrabang, National Metal and Materials Technology Center (MTEC), Thailand Graduate Institute of Science and Technology (TGIST) for all the support to this research to be achieved.

Secondly, I would like to express my sincere gratefulness of gratitude to my advisor Professor Dr. Suttichai Assabumrungrat, for instruction, many supports, and instructional me to do such a useful project. I would like to express my special gratitude to my co-advisor Dr. Sumittra Charojrochkul for suggestions, and valuable information. I would like to express my thankfulness to my co-advisor Assistant Professor. Dr. Apiluck Eaid-Ua for his suggestion, kind advice, and supports, since being an undergraduate student.

Thirdly, my grateful thanks to my family and friends for their love, supports, encouraging me and share my problems or just listen while doing this project. Finally, The authors would like to acknowledge the funding given by The Thailand Graduate Institute of Science and Technology (TG-33-09-61-062M) for their financial support in this project.

จุฬาลงกรณ์มหาวิทยาลัย  
CHULALONGKORN UNIVERSITY

Dolrudee Jaruwat

## TABLE OF CONTENTS

	Page
.....	iii
ABSTRACT (THAI).....	iii
.....	iv
ABSTRACT (ENGLISH).....	iv
ACKNOWLEDGEMENTS.....	v
TABLE OF CONTENTS.....	vi
CONTENT OF TABLES.....	ix
CONTENT OF FIGURES.....	x
CHAPTER 1.....	1
1.1 Motivation.....	1
1.2 Research objectives.....	3
1.3 Scope of research work.....	3
1.4 Implementation plan.....	4
1.5 Schematic diagram of research methodology.....	5
CHAPTER 2.....	6
2.1 Vegetable oils.....	6
2.2 Biodiesel technology.....	7
2.3 Transesterification.....	9
2.4 Hydrogenation of polyunsaturated FAMES.....	12
2.5 Heterogeneous catalyst.....	14
2.6 Bimetallic catalysts.....	15

2.7 Activated carbon .....	16
2.8 Activated carbon production .....	17
2.9 Biomass conversion technology.....	19
2.10 Pore characteristic of activated carbon.....	20
2.11 Literature reviews.....	22
CHAPTER 3.....	31
3.1 Preparation of activated carbon .....	31
3.2 Catalyst preparation .....	34
3.3 Transesterification of soybean oil.....	36
3.4 Experimental set up for partial hydrogenation.....	36
3.5 Test of catalyst in partial hydrogenation of soybean FAME .....	37
CHAPTER 4.....	39
4.1 Synthesis of activation carbon .....	39
4.2 Preparation of metal catalyst impregnated on AC.....	57
4.3 Reaction study in partial hydrogenation process .....	64
CHAPTER 5.....	73
5.1 Conclusions .....	73
5.2 Recommendation.....	74
APPENDIX.....	75
APPENDIX A.....	76
A.1 Specification data of soybean oil .....	76
A.2 Chemical property of soybean oil.....	77
A.2 Chemical property of soybean biodiesel.....	77
APPENDIX B.....	79



B.1 Temperature profile of stainless steel horizontal tube reactor.....	79
APPENDIX C.....	80
C.1 Weight hourly space velocity (WHSV).....	80
C.2 C18:2 conversion.....	80
C.3 Trans C18:1 to cis C18:1 ratio.....	80
APPENDIX D.....	81
D.1 Calculation of volume of H <sub>2</sub> adsorption on catalyst.....	81
D.2 Calculation of metal active sites.....	81
D.3 Calculation of metal dispersion.....	81
APPENDIX F.....	83
F.1 Calculation of average crystallite size.....	83
APPENDIX G.....	84
G.1 International conference.....	84
REFERENCES.....	84
VITA.....	93

## CONTENT OF TABLES

<b>Table 1.1</b> Implementation plan.....	4
<b>Table 2.1</b> Fatty acid composition of pure edible vegetable oils.....	6
<b>Table 2.2</b> Properties of biodiesel from vegetable oil.....	7
<b>Table 2.3</b> Properties of typical catalyst supports.....	15
<b>Table 2.4</b> Properties of materials used in the production of activated carbons.....	17
<b>Table 2.5</b> The composition of lignocellulose in biomass.....	23
<b>Table 2.6</b> Physical properties of the support and Pd catalyst.....	23
<b>Table 2.7</b> FAME compositions, TOFs, and ratio of trans/cis C18:1 of Pd/MCM-41-SiO <sub>2</sub> and Pd/MCM-41-silatrane.....	24
<b>Table 2.8</b> Physical properties of activated carbon from olive stones.....	28
<b>Table 2.9</b> Physical properties and dye absorption of activated carbon.....	29
<b>Table 2.10</b> Effect of activation condition and physical properties of activated carbon.....	29
<b>Table 4.1</b> Ultimate and proximate of cattail leave and hydrochar.....	39
<b>Table 4.2</b> Functional group of lignocellulose.....	40
<b>Table 4.3</b> Textural properties of activated carbon.....	44
<b>Table 4.4</b> Textural properties of activated carbon.....	49
<b>Table 4.5</b> Ultimate and proximate analysis of AC with base activation.....	57
<b>Table 4.6</b> Characteristics of catalysts.....	63
<b>Table 4.7</b> FAMEs composition and some fuel properties of soybean FAME and biodiesel product after reaction with monometallic catalyst.....	65
<b>Table 4.8</b> FAMEs composition and some fuel properties of soybean FAME and biodiesel product after reaction with bimetallic catalyst.....	68
<b>Table 4.9</b> FAMEs composition and some fuel properties of soybean FAME and biodiesel product after reaction with MoNi/C catalyst.....	70
<b>Table A.1</b> Specification of soybean oil.....	76
<b>Table A.2</b> Specification of the EAS-ERIA BDF standard.....	78

## CONTENT OF FIGURES

<b>Figure 1.1</b>	Schematic diagram of research methodology.....	5
<b>Figure 2.1</b>	The pathway of the acid-catalyzed transesterification.....	11
<b>Figure 2.2</b>	Reaction pathway of (a) overall (b) 3-steps transesterification reaction...	12
<b>Figure 2.3</b>	Partial and full hydrogenation of polyunsaturated FAME.....	14
<b>Figure 2.4</b>	Types of physisorption isotherms according to the IUPAC classification..	21
<b>Figure 2.5</b>	Composition of biodiesel feed and H-FAME derived from batch (B) and continuous-flow (C) reactors at different conversions of C18:2 and C18:3.....	25
<b>Figure 3.1</b>	Schematic diagram of Horizontal tube furnace for chemical activation of Cattail leave to produce activated carbon.....	31
<b>Figure 3.2</b>	Schematic diagram of transesterification in three-necked round-bottomed flask.....	36
<b>Figure 3.3</b>	Schematic diagram of continuous-flow trickle-bed reactor.....	37
<b>Figure 4.1</b>	FTIR spectra of CL and HC.....	41
<b>Figure 4.2</b>	SEM images of (a) CL and (b) HC at 500x magnification.....	41
<b>Figure 4.3</b>	Adsorption isotherms of N <sub>2</sub> on activated carbon at 77 K.....	43
<b>Figure 4.4</b>	FTIR spectra of activated carbon.....	45
<b>Figure 4.5</b>	SEM images of (a) HS500-4, (b) HP500-4 at 500x, (c) KO900-4 and (d) NO900-4.....	46
<b>Figure 4.6</b>	The pore size distribution of activated carbon with basic activation.....	49
<b>Figure 4.7</b>	The pore size distribution of activated carbon with acidic activation.....	50
<b>Figure 4.8</b>	FTIR spectra of activated carbon with acid activation.....	51
<b>Figure 4.9</b>	SEM of activated carbon of (a) HP500-4, (b) HP700-4 at 500x, and (d) HP900-4.....	52
<b>Figure 4.10</b>	FTIR spectra of activated carbon with acid activation with base activation.....	53
<b>Figure 4.11</b>	SEM of activated carbon with base activation.....	54
<b>Figure 4.12</b>	Thermal Gravimetric Analysis of activated carbon.....	55
<b>Figure 4.13</b>	SEM image of activated carbon with various concentration.....	56

<b>Figure 4.14</b> SEM image of mono and bimetallic (a) Mo/C, (b) Ni/C, (c) Cu/C, (d) Fe, (e) MoNi/C, (f) MoCu/C and (g) MoFe catalyst.....	58
<b>Figure 4.15</b> TPR-H <sub>2</sub> profiles of Ni/C, MoNi/C and Mo/C catalyst.....	59
<b>Figure 4.16</b> TPR-H <sub>2</sub> profiles of Cu/C, MoCu/C and Mo/C catalys.....	60
<b>Figure 4.17</b> TPR-H <sub>2</sub> profiles of Fe/C, MoFe/C and Mo/C catalyst.....	61
<b>Figure 4.18</b> XRD patterns of Mo/C, MoCu, Cu/C, MoNi/C, Ni/C, MoFe and Fe/C Catalyst.....	62
<b>Figure 4.19</b> EDS mapping of a) Mo/C, b) Ni/C, c) Cu/C and d) Fe/C, catalyst.....	66
<b>Figure 4.20</b> Effect of Monometallic catalyst on composition of C18.....	67
<b>Figure 4.21</b> Effect of monometallic catalyst on composition of cis and trans C18:1 FAMES.....	69
<b>Figure 4.22</b> Effect of Bimetallic catalyst on composition of C18.....	69
<b>Figure 4.23</b> Effect of Bimetallic catalyst on composition of cis and trans C18:1 FAMES.....	71
<b>Figure 4.24</b> Effect of reaction temperature on composition of C18.....	72
<b>Figure 4.25</b> Effect of reaction temperature on composition of cis and trans C18:1 FAMES.....	77
<b>Figure A.1</b> FTIR spectra of soybean oil.....	77
<b>Figure A.2</b> GC chromatogram of soybean FAME.....	77
<b>Figure B.1</b> Temperature profile of stainless steel horizontal tube reactor Energy used: 4,000 kW/h.....	79
<b>Figure D.1</b> Example of pulse H <sub>2</sub> chemisorption.....	82
<b>Figure F.1</b> Example of the full width at half maximum (FWHM).....	83

## CHAPTER 1

### INTRODUCTION

#### 1.1 Motivation

Nowadays, energy consumption has been greatly expanded especially in transportation and industry. In 2019, almost 30.5% of the vehicle were used diesel fuel in the European Union. Air pollution is released from the diesel engine such as particulate matter (PM), hydrocarbon (HC), carbon dioxides (CO<sub>2</sub>), carbon monoxides (CO), and nitrogen oxides (NO<sub>x</sub>) [1]. There are about 22% of greenhouse gas is released from the transport sector. The International Energy Agency (IEA) estimates that from 2020 to 2035, there will be 8.6 billion tons of carbon dioxide to be released into the atmosphere [2]. Therefore, biodiesel is an alternative energy obtained from biomass, which is environmentally friendly. Also, it can reduce diesel consumption by blending biodiesel into diesel fuel. Currently, 5% biodiesel blends (B5) for diesel engines has been accepted by car manufacturers that there are no problems with engine equipment. The government aims to increase the proportion of biodiesel to 20% according to the standard but increasing the mixing ratio has limitations on fuel properties such as viscosity, density, calorific value, flash point, cloud point, pour point, carbon residue, and oxidation stability.

Fuel properties of vegetable oil are different from diesel fuel because of molecular structure and composition [3]. Polyunsaturated FAMES are present in composite of the feedstock during transesterification. If biodiesel contains high polyunsaturated FAMES, resulting in low stability, which makes the biodiesel unable to be store for long time and affects the overall quality of biodiesel [4]. Acidity and viscosity are the causes of corrosion and clogging of engine parts. Therefore, the hydrogenation reaction or adding hydrogen to the double bond of unsaturated fatty acids could improve the oxidation stability of biodiesel. The complete hydrogenation operates under severe condition, causing poor cold flow properties. A high amount of saturated FAMES exhibits a negative affect on the fuel blockage in the fuel systems of vehicles [5]. Therefore, mild reactions can convert polyunsaturated FAME towards monounsaturated FAME without affecting the cold flow properties. It is

difficult to control the activity and selectivity of the desired product, in which a catalyst can enhance the forward reactions and product formation.

Many researchers report that noble metals (Pd, Pt and Rh) are generally used as catalysts for partial hydrogenation. The disadvantage of noble metals are expensive and selective of C18:0 and TFA. The transition metal (Mn, Fe, Co, Ni, Cu, and Zn) has been employed for partial hydrogenation because it is inexpensive [6]. However, Ni has limited catalysis activity compared to noble metals and operating under high-pressure  $H_2$ . Therefore, a catalyst was promoted by the second metal, which can be improves chemical properties including electronic structure and geometry. Bimetallic surfaces usually show unique properties which did not appear on both monometallic. Bimetallic catalysts can improve activity and selectivity of cis-isomer content in H-FAME. Bimetallic catalyst are attractive in modified a catalytic such as PdPt, PtNi, NiAg and PdMo, which could enhance oxidation stability while maintaining cold flow properties [7]. Moreover, catalyst type is important to conversion of monosaturated FAME.

Another important factor is support material in which inorganic support is commonly used such as zeolite, silica, and alumina. Although the acidity of the support material promotes catalytic activity, it also provided the catalyst deactivation. Acidic supports enhance the formation of coking on catalyst because it is sensitive to carbon compounds in biodiesel. From the above problems, the catalyst has a short lifetime and requires a regeneration. Besides, the inorganic support has a low surface area and a small pore size, which affects the dispersion of the active phase and the mass transport of oil molecules. Activated carbon is one of the materials used as supporting catalyst for partial hydrogenation because of high surface area and large pore diameter for metal distribution and biodiesel yield [8]. The advantages of activated carbon are low coke formation, thermal stability, biodegradable materials, cost-effective and available raw materials such as coconut shell, bagasse, and rice husk [9].

Concerning the above mention paragraph, an application of activated carbon produced from biomass as a catalyst support for partial hydrogenation of soybean biodiesel to H-FAME is a promising alternative. The synthesis of activated carbon

from cattail leave were used as catalyst support for partial hydrogenation of soybean biodiesel. In this study, activated carbon will be synthesized via two-step process hydrothermal and chemical activation using  $H_2SO_4$ ,  $H_3PO_4$ , KOH and NaOH by different temperatures in the range 500-900°C including different concentration (2 M, 4 M and 6 M). Activated carbon will be investigated by FTIR, SEM, Nitrogen-sorption, proximate and ultimate analysis, CHNO. Then the metal catalyst impregnated on the surface of AC will be prepared by rotary evaporation technique using ammonium molybdate solution as based catalyst (MoNi, MoCu and MoFe). The catalyst was characterized using XRD, SEM-EDS, Nitrogen-sorption,  $H_2$ -chemisorption and  $H_2$ -Temperature program reduction. Moreover, a continuous flow trickle-bed reactor will be used to examine the catalytic activity including the conversion of polyunsaturated FAME and selectivity of cis-isomer in partial hydrogenation. The composition of H-FAME and biodiesel feed will be investigated using GC-FID. Finally, the study properties of H-FAME such as oxidation stability, cloud point and pour point has been evaluated.

## 1.2 Research objectives

1.2.1 To develop the mesoporous carbon from cattail leave via hydrothermal and chemical activation for metal catalyst support.

1.2.2 To determine the optimum condition of chemical activation such as temperature, activating agent, and concentration.

1.2.3 To investigate the effect of molybdenum-based catalyst and catalyst ratio on the activity cis-unsaturated FAME selectivity for partial hydrogenation reaction of soybean FAME.

1.2.4 To improve the oxidation stability and cold flow properties of soybean H-FAME derived from partial hydrogenation in a continuous flow reactor.

## 1.3 Scope of research work

1.3.1 Preparation of carbon support material using different condition of chemical activation (temperature, activating agent, and concentration) and characterization of activated carbon using different techniques such as SEM, FTIR, Nitrogen sorption, proximate, and ultimate analysis.





### 1.5 Schematic diagram of research methodology

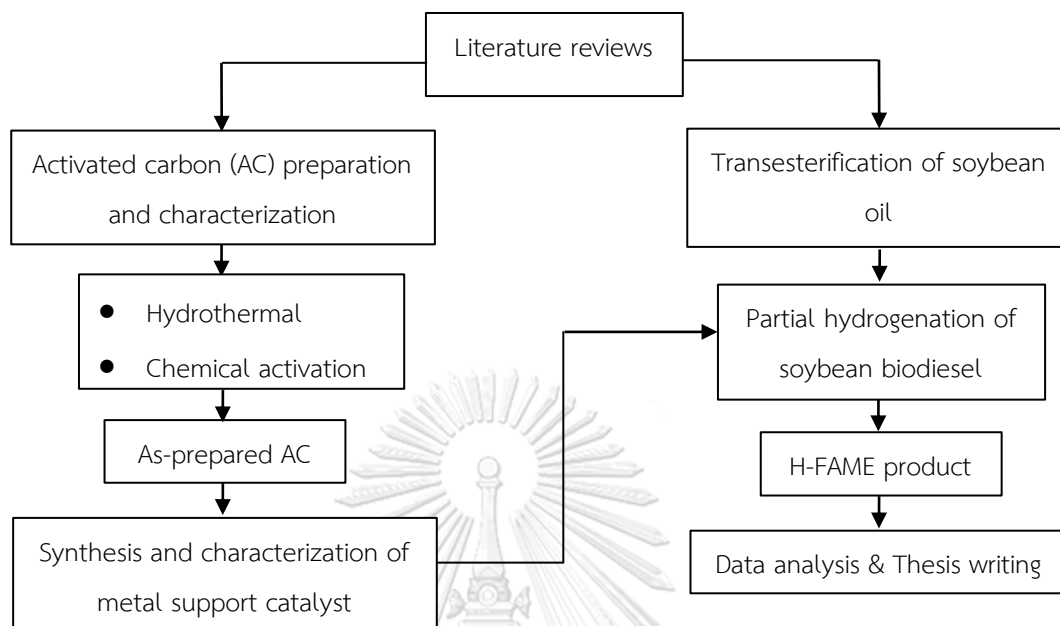


Figure 1.1 Schematic diagram of research methodology

## CHAPTER 2

### THEORY AND LITERATURE REVIEWS

This chapter presents a general explanation of essential knowledge for biomass conversion technology, activated carbon, technology for the activated carbon production, pore characteristic of activated carbon, vegetable oils, biodiesel properties, transesterification of soybean oil, partial hydrogenation of polyunsaturated FAMES, bimetallic catalysts and characterization techniques

#### 2.1 Vegetable oils

The compositions of fatty acid composition are shown in **Table 2.1**. General, the structure of vegetable or animal fat contains triglycerides with saturated and unsaturated fatty acid. The composition of fatty acids mostly has affected by the type and character of geographic conditions in growing plants. Nevertheless, the chain of natural fatty acid has long 8 to 24 carbon atoms. There is also a composition of saturated fatty acids with light carbon and double bonds. The main composition of vegetable oil exhibits the trend of oleic acid (C18:1) > linoleic acid (C18:2) > palmitic acid (C16:0) > stearic acid (C18:0). Also, there is a composition of saturated fatty acids with light carbon (10:0, C12:0 and C14:0) and double bonds, which significantly influence the properties of the fuel used in the engine. The composition of fatty acid are different in each feedstock, which mainly affected the parameter of fuel quality such as density, viscosity, heating value, cold flow properties, oxidative stability, flash point and cetane number. Viscosity of vegetable oil are high levels than petroleum-based diesel because FAMES have large molecular mass and chemical structure [10]. The properties of vegetable oil have already been are summarized in **Table 2.2**.

**Table 2.1** Fatty acid composition of pure edible vegetable oils

Vegetable oil	Lauric (12:0)	Myristic (14:0)	Palmitic (16:0)	Palmitoleic (16:1)	Stearic (18:0)	Oleic (18:1)	Linoleic (18:2)	Linolenic (18:3)	Arachidic (20:0)	Behenic (22:0)	Lignoceric (24:0)	Ref.
Coconut	49.0	8.0	8.0	-	2.0	6.0	2.0	-	-	-	-	[11]
Palm	0.2	1.1	44.0	-	4.5	39.2	10.1	0.4	0.1	-	-	[12]
Soybean	-	0.1	11	-	4	23	54	7.6	-	-	-	[13]
Corn	-	0.1	11	-	2	25	60	1	-	-	-	[13]
Canola	-	0.1	4.1	-	2	61	21	9	-	-	-	[13]
Sunflower	0.5	0.2	4.8	0.8	5.7	20.6	66.2	0.8	0.4	-	-	[2]

Rapeseed	-	-	3.49	-	0.85	64.40	22.30	8.23	-	-	-	[2]
Jatropha	0.1	0.1	14.6	0.6	7.6	44.6	31.9	0.3	0.3	-	-	[2]
Olive	0.6	0.4	10.6	0.6	3.3	17.9	14.7	1.1	0.1	-	-	[14]
Castor	-	-	1.1	1.0	4.1	87.8	4.8	0.5	-	-	-	[15]
Mustard	-	-	3.5	-	1.6	19.7	22.2	13.4	-	-	-	[15]

## 2.2 Biodiesel technology

The first-generation biofuels involve ethanol, obtained from the fermentation and distillation of plant. The chemical transformation generally produce biodiesel by oil extraction from corn, soybean and palm. The first-generation biodiesel had a disadvantageous effect on world food plants. After that, non-edible feedstock was used to replace the edible oil in the second-generation such as lignocellulose materials (wood and husks) and non-edible oils. These feedstocks still desire a large agriculture area, but it has affected to arable land [16].

Although vegetable oil can reduce exhaust emissions (particulate matter (PM), hydrocarbon (HC), carbon dioxides (CO<sub>2</sub>), carbon monoxides (CO) and nitrogen oxides (NO<sub>x</sub>)) lead to reduce air pollution when compared with fossil fuel. Furthermore, biodiesel can employ in diesel engines with greater efficiency as performed with standard diesel fuel. However, vegetable oils have a higher viscosity, lower volatility and higher polyunsaturated characteristic which cannot directly use in the diesel engine because the atomization of vegetable oil into spray within the injector is quite poor [3]. Properties of biodiesel from the different feedstock are shown in **Table 2.2**.

**Table 2.2** Properties of biodiesel from vegetable oils

Vegetable oil	Kinematic viscosity (cSt, 40 °C)	Viscosity index	Clogged fuel filters (°C)	Cloud Point (°C)	Pour Point (°C)	Oxidation stability (h, 110 °C)	Ref.
Coconut	3.18	-	-1	-4	1	8.01	[17]
Palm	1.79	203.6	12	15	13	23.56	[17]
Soybean	4.37	257.8	-3	1	1	4.08	[17]
Cotton seed	4.11	-	1	7	6	1.85	[2]
Canola	4.53	236.9	-10	-9	-3	7.08	[17]
Sunflower	4.44	-	-3	3.4	-	0.90	[2]

Rapeseed	4.60	-	-	-6	1, -3	7.6	[17]
Jatropha	5.11	194.6	10	-6	10	4.84	[17]
Olive	4.50	-	-6	0	-	3.3	[2]
Peanut	4.42	-	-	0	-8	2	[2]
Beef tallow	4.82	-	14	12	9	3.2	[2]

### 1) Oxidation stability

Oxidation stability is one of the significant parameters in determining the performance of biodiesel fuel, which indicates the degradation during storage or use. Oxidation stability depends on the amount of FAME, i.e., linolenic FAME (18:3) and linoleic FAME (18:2). Biodiesel consists of double bonds in FAME in which a high reactivity with  $O_2$  results in low oxidation stability compared to fossil diesel. Furthermore, oxidation stability affects the various fuel properties, such as acid number, peroxide value, kinematic viscosity, density, iodine value and polymer content. Nevertheless, trans-unsaturated FAME are more sensitive to oxidation when compare with cis-unsaturation FAME. In particular, the polyunsaturated FAME consists of the higher amount of reactive bis-allylic sites than the monounsaturated FAME, which influences the lower oxidation stability than monounsaturated FAME. The bis-allylic protons are energetically sensitive to radicals and can be oxidize with oxygen to generate oxygen compounds (peroxides and hydroperoxides) which lead to problems with engine operation such as coke deposition in the engine, corrosion and blocking of the fuel injection system of the engine, etc. Besides, the oxidation stability of biodiesel can be improved by adding natural or synthetic antioxidant additives. According to EN 14112 method, the least probable time of oxidation stability is 3 h for biodiesel, while in ASTM D6751 the standard is not no notified. [18, 19]

### 2) Cold flow property

Cold flow properties (CFPs) indicate the flow performance of fuel at low temperatures, which depend mainly on content of saturated FAME. Biodiesel with a more significant amount of saturated FAME commonly shows poor cold flow property. In comparison, biodiesel with a higher amount of unsaturated FAME

generally gives excellent cold flow property. Furthermore, other factors affect cold flow properties such as molecular weight, branch, and polar groups in FAME. Including, the transesterification reaction with the long-chain alcohol enhances the cold flow property of biodiesel. The cold flow properties depends on 3 features : the cloud point (CP), pour point (PP), and cold filtering plugging point (CFPP) [20]

#### Cloud point (CP)

Cloud point (CP) is the least probable temperature that wax begins to form in fuel. It is the origin of the formation of crystals, resulting in appearance of clouds in fuel. Usually, the cloud point is determined as the temperature of the sample, while the smallest cluster of wax crystals is first observed during cooling under prescribed conditions. The formed crystals clog within strainers and filters result in restricting the fuel flow. Thus, by increasing the temperature, the cloud can dissolve better. The standard method for defining cloud point for biodiesel is assigned in ASTM D2500 between  $-3\text{ }^{\circ}\text{C}$  to  $12\text{ }^{\circ}\text{C}$  [21, 22].

#### Pour point (PP)

Pour point is the lowest temperature that liquid fuel loses flow properties. The cluster of crystallite agglomerate in the gel after freezing at low temperature for a long time. Usually, the pour point is lower than the cloud points. Biodiesel has a higher pour point and cloud points than diesel fuel. In addition, the method in preventing crystal growth is by adding polymers which inhibits the crystal formation. The main disadvantage of additive is the extra cost. ASTM D97 is a standard for defining the value of pour point for biodiesel [21, 22].

### 2.3 Transesterification

Transesterification has been widely accepted in several years for the conversion of triglyceride in vegetable oil into biodiesel or fatty acid methyl ester in overcoming the problems of direct use of vegetable oil. Biodiesel has similar properties as fossil-based diesel because the viscosity of the product is diminished compared to feedstock/vegetable oils. Transesterification is the reaction of triglyceride molecule with the homogeneous catalyst and short-chain alcohols (methanol and ethanol), which transforms into biodiesel and glycerol. The most

frequently used alkaline catalysts are potassium and sodium hydroxides because alkaline-catalyzed transesterification reactions are much faster than acid-catalyzed esterification reactions. Moreover, one of the main factors of the transesterification is alcohol to vegetable oil molar ratio because excess of alcohol promotes the formation of the products. Hence, the ideal alcohol to oil ratio has to be appropriate process [23].

#### 1) Homogeneous Catalyst

##### 1.1.1 Acid-catalyzed transesterification Reactions

The vegetable oil with higher FFA content (>2%) suitable for esterification by acid catalyst because it can reduce the amount of FFAs compare to alkaline catalysts. Although the acid catalyst promotes high fatty acid methyl yield, it desires a higher operating temperature, slow reaction time and difficult separation. The catalyst often uses the bronsted acids, especially hydrochloric, sulfuric and sulfonic acid. The mechanism of acid esterification is shown in **Figure 2.1**. In the first step, Carbocation (II) generated from the carbonyl group protonation of the ester. Then, carbocation (II) reacts with alcohol into tetrahedral intermediate (III) followed by the removal of glycerol molecule from the new ester (IV) and catalyst. Moreover, formation of carboxylic acids occurs by reaction of carbocation (II) with water, which provide alkyl ester yield reduction. Hence, water-free raw materials is preferred to avoid carboxylic acid formation. Typically, raw materials with an acidity of fewer than 2.0-4.0 mg KOH/g is required to undergo esterification reaction before transesterification [23].

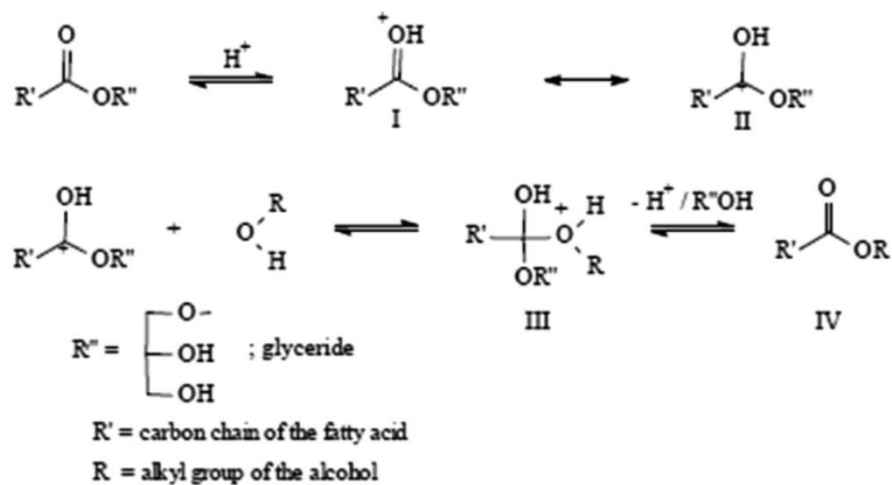


**Figure 2.1** The pathway of the acid-catalyzed transesterification of vegetable oils [23].

### 1.1.2 Base-catalyzed transesterification Reactions

Feedstock with a small of FFAs commonly reacts with a base catalyst, called transesterification. This reaction provides high ester yield because the corrosion of the alkaline catalyst is less compared to the acid catalyst. Consequently, transesterification reactions are required in industry. Potassium and sodium hydroxide are applied as catalysts for base-catalyzed transesterification reactions. Furthermore, problems of transesterification are several times washing to remove glycerol and catalyst in biodiesel. The mechanism of transesterification is shown in **Figure 2.2**. The first step, the reaction of vegetable oil and short alcohol generate alkoxide with protonated catalyst (Eq. 15.1), combination of alkoxide and nucleophilic on carbonyl moiety of triglyceride has formed a tetrahedral intermediate (Eq. 15.2) followed by the production of alkyl ester and formation of anion, which correspond to diglyceride (Eq. 15.3), and deprotonation of the catalyst regenerates the active species (Eq. 15.4), which is ready for the start of reaction cycle [23].

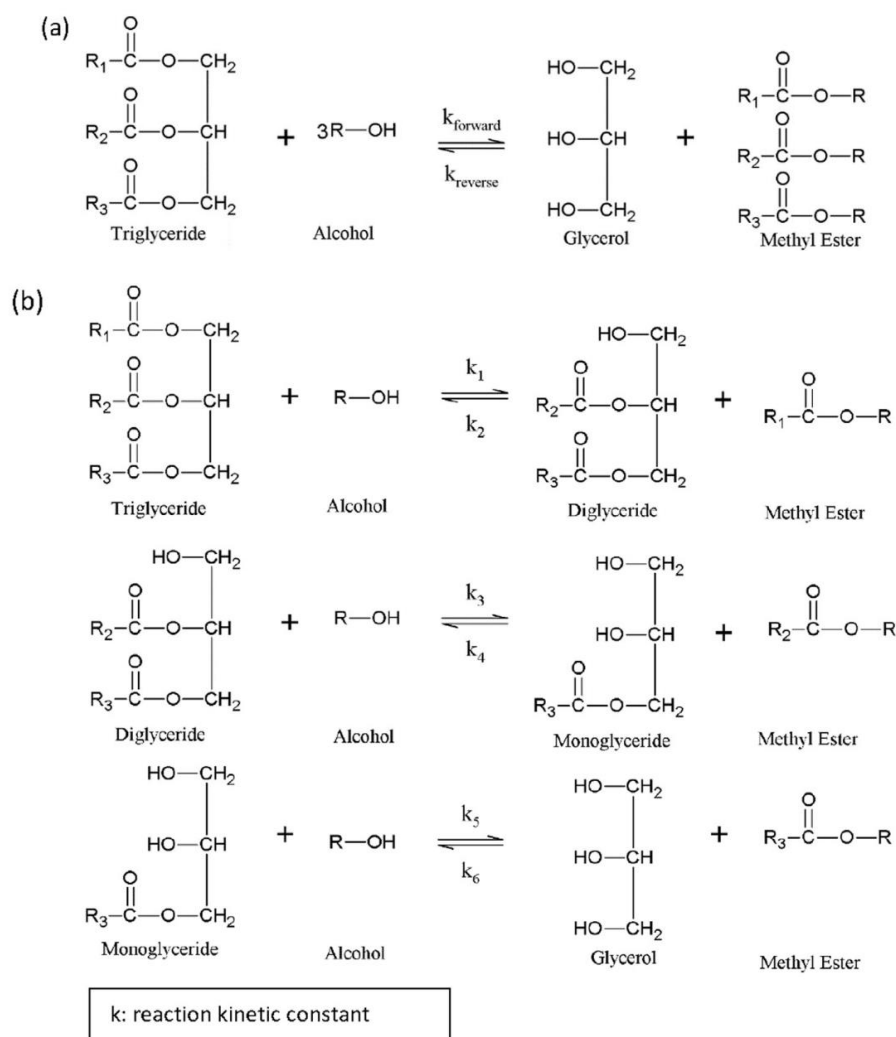


**Figure 2.2** Reaction pathway of (a) overall (b) 3-steps transesterification reaction [23].

## 2) Heterogeneous catalyst

Many researchers study solid-phase catalysts for transesterification catalysts to resolve the problem of the homogeneous catalyst. The advantages of the heterogeneous catalyst are easy separation from the product and repeated use. The major solid catalysts applied in transesterification reactions such as Hb-Zeolite, ZnO,  $\text{TiO}_2/\text{ZrO}_2$ ,  $\text{Al}_2\text{O}_3/\text{ZrO}_2$ , zeolites, alkaline earth oxides,  $\text{CaTiO}_3$ ,  $\text{KF}/\text{Al}_2\text{O}_3\text{CaMnO}_3$ ,  $\text{SnCl}_2$ ,  $\text{CaO}$ , and  $\text{MgO}$  etc.

## 2.4 Hydrogenation of polyunsaturated FAMES

In Figure 2.3 shown polyunsaturated FAMES (C18:3 and C18:2) can convert toward monounsaturated (C18:1) or saturated methyl esters (C18:0) via C=C



hydrogenation or into fatty alcohols by the C=O hydrogenation. Full hydrogenation of FAMEs provided the removal of oxygen and the appearance of new hydrocarbons. Hydrogenation reaction can produce with or without catalysts based on the requisite properties of the products. It is difficult to control the selectivity of hydrogenation reactions without a catalyst because catalysts can control the selection of the desired product. The catalyst will absorb with the H<sub>2</sub> molecules and promote the reaction. Many researchers reported that metal group VIII metals like Ni, Co, Pd, Pt and Rh as catalysts commonly use for partial hydrogenation of C=C double bond in FAME. Usually, catalysts classify into two types, which are homogeneous catalysts and heterogeneous catalysts based on the bulk phase of reactants. Homogeneous catalysts are normally in the fluid phase, which is the same phase as the precursor and the products. Homogeneous catalysts appearance better activity and cis-isomer selectivity in hydrogenation reactions. The advantages of homogeneous catalysts are higher activity and selection of cis-C18: 1 in hydrogenation reactions. Behr A et al. [24] reported that using Na<sub>2</sub>CO<sub>3</sub> and Na<sub>2</sub>PdCl<sub>2</sub> catalysts for the hydrogenation of sunflower oil, with homogeneous selectivity of cis-C18:1 up to 93%. Moreover, Ru (II) catalyst was used for hydrogenation reaction, which can promote the activity and the selectivity of cis-isomer compared to solid catalyst Ni [25]. Another way, the hydrogenation reaction using heterogeneous catalysts, which promoted the molecules of hydrogen and double bond of FAME to adsorb on the catalyst surface. Hydrogen molecule will dissociate toward 2 atomic hydrogens and then 1 atom of hydrogen added into the C=C of fatty acid in a reversible step. After that, the second hydrogen atom was added into the double bonds of fatty acids, resulting in the hydrogenation reaction irreversible. The advantage of heterogeneous catalysts is comfortable a reusable catalyst from the products, in which solid catalysts are more favored compared to homogeneous catalysts. Furthermore, Solid catalysts can operate under high-temperature reactions because it is highly resistant to extreme conditions [7]. The heterogeneous catalysts are select from transition metal with high melting points such as Sc, V, Mn, Fe, Ti, Co, Ni, Cr, Cu, and Zn. Many researchers studied the hydrogenation reaction using noble metals such as Pd, Ru, Rh and Pt.

The research revealed that the catalysts were ordered according to the hydrogenation activity as follows: Pd > Rh > Pt > Ru > Ni, respectively [26].

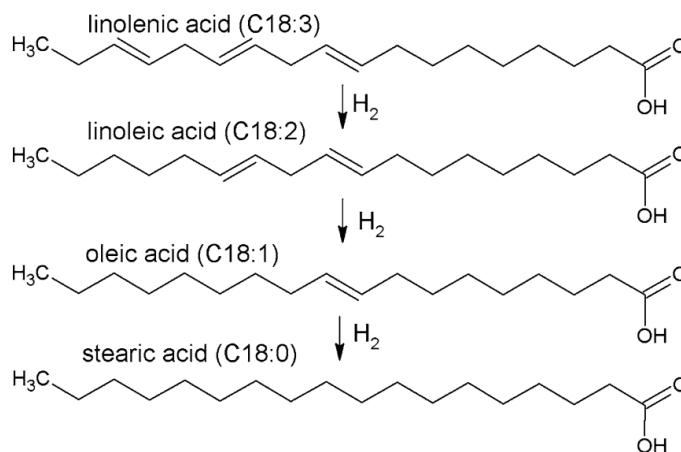


**Figure 2.3** Partial and full hydrogenation of polyunsaturated FAME.

## 2.5 Heterogeneous catalyst

Heterogeneous catalysts have the advantage of easy separating the products, without wastewater from product washing and reducing operating costs. Moreover, the solid catalyst can recover to regeneration, which is suitable for industrial production. Heterogeneous catalyst is separate phases with the reactants, in this case, the catalyst is a solid phase, while the reactant is liquid or gas. Therefore, heterogeneous catalysts have been considered for continuous reactors because of high mechanical properties and product yield. The solid catalysts are composed of two main components. The first part is called active site, which is dispersed on support material for surface reaction (i.e. metal, metal oxide, metal sulfide). Including, acid sites normally present in bifunctional catalysts such as zeolite, Al<sub>2</sub>O<sub>3</sub>, and Al<sub>2</sub>O<sub>3</sub>/SiO<sub>2</sub>. The second component, the support phase is a significant necessity for industrial processes because of the high surface area and dispersion of the active site. Although, the support material is porous with high thermal stability, the geometry and dimension of catalyst particles may have affected the pressure drop and heat and mass transfer. Hence, choosing support must consider the pore size, support interaction, accessibility of the reactants and operating condition to suitability of the application. The properties of typical catalyst supports are shown in

**Table 2.3.** These include  $\text{Al}_2\text{O}_3$ ,  $\text{SiO}_2$ , activated carbon,  $\text{TiO}_2$ ,  $\text{MgO}$ , zeolites and  $\text{Al}_2\text{O}_3/\text{SiO}_2$ . They have a different property depend on the synthesis process and material structure, which affect to anisotropic mechanical, density, strength, and thermal stability. However, the structure of the support material improves the yield of the product and catalyst deactivation resistibility. The improvement of catalysts is essential to enhance the conversion reactions [27, 28].

**Table 2.3** Properties of typical catalyst supports [27].

Support	Crystallographic	Surface area (m <sup>2</sup> /g)	Properties	Applications	Ref.
$\text{Al}_2\text{O}_3$	$\alpha$ and $\gamma$	400	Thermal stable, three-way catalyst	Steam reforming and many other catalysis	[27]
$\text{SiO}_2$	Amorphous	1000	Thermal stable	Hydrogenation and other other catalysis	[27]
Carbon	Amorphous	1000	Unstable in oxide	Hydrogenation	[27]
$\text{TiO}_2$	Anatase	150	Limited thermal stability	Selective catalytic reduction	[27]
$\text{MgO}$	FCC	200	Rehydration may be problematic	Steam reforming catalysis	[27]
Zeolite	Various (ZSM-5)	-	Highly defined pore system, shape selective	Bifunctional catalysis	[27]
$\text{SiO}_2/\text{Al}_2\text{O}_3$	Amorphous	800	Medium strong acid sites	Dehydrogenation catalysis, Bifunctional catalysis	[27]

## 2.6 Bimetallic catalysts

Bimetallic catalysts consist of two various metals, which possibility each is miscible or immiscible as macroscopic bulk alloys. The bimetallic catalyst is superior over the monometallic catalyst because the combination of active and inactive metal can improve catalytic performance of reaction. Therefore, the selection of metal types must be considered appropriate for the catalytic processes. Generally, the property of alloy metallic differs from the bulk metallic such as geometric ensemble and electronic ligand lead to change to derive new features with enhanced selectivity, activity, and stability. Bimetallic catalysts have been modified electronic and chemical properties because of two significant reasons. (i) the generation of heteroatom bonds converts the electronic behavior on surface, exhibiting improvement of their electronic structure by the ligand effect. (ii) the geometry of the bimetallic structure usually is different from the monometallic. For

example, Cu abundantly covers on the surface, while Ni alloys diffuse in Cu. Furthermore, the surface component of binary alloys may be changed by the reaction atmosphere [27].

## 2.7 Activated carbon

Carbon material is widely employed in the application such as water treatment, air and gas treatment, food industry, catalysis and pharmaceutical, mineral industries since it is high porosity and surface area (500-1500 m<sup>2</sup>/g). Activated carbon is most attractive for eliminating pollutants such as heavy metals, dyes, detergents. Biomass or agricultural waste are used as feedstock for produced via thermal process. Many studies have reported that activated carbon is produced from rice husk, sawdust, palm shells, soft wood, corn cobs, and coconut shells, lignite coal and bituminous coal etc. At present, activated carbon are applied in heterogeneous catalysis as supports or direct catalysts because activated carbons have complicated surface chemistry that consist of a several of functional groups. The activated carbons have connected between pores and channels within a strong skeleton of the disordered sheet of carbon atoms that promote a highly porous structure among the carbon sheet [29].

The choice of the feedstock for activated carbon production considers from the following criteria: (i) abundant availability and cheap; (ii) Low inorganic content; (iii) low decompose in storage; and (iv) ease of activation. **Table 2.4** presents the properties of materials used in the production of activated carbons. The yield of activated carbons from coal is ordinarily higher than for biomass materials, above 30 wt.%. Although the industry generally produces activated carbon from peat, lignite, and different coal types depending on availability and cost, these precursors affect the environment. Lignocellulose materials such as wood, sawdust, nutshells, and fruit stones are mostly used as precursors about 45 wt% of the entire feedstock because activated carbon products presence low inorganic matter and low ash content, but the relatively high volatile matter must be controlled of the production process [30, 31].

**Table 2.4** Properties of materials used in the production of activated carbons [31].

Raw material	Carbon (wt.%)	Volatile (wt.%)	Density (wt.%)	Ash (wt.%)	Texture of activated carbon	Ref.
Soft wood	40-45	55-60	0.4-0.5	0.3-1.1	Soft, large-pore volume	[31]
Hard wood	40-42	55-60	0.55-0.8	0.3-1.2	Soft, large-pore volume	[31]
Lignin	35-40	58-60	0.3-0.4	-	Soft, large-pore volume	[31]
Nutshell	40-45	55-60	1.40	-	Hard, large-pore volume	[31]
Lignite	55-70	25-40	1.0-1.35	5-6	Hard, small-pore volume	[31]
Soft coal	65-80	20-30	1.25-1.5	2-12	Medium-hard, medium-pore volume	[31]
Petroleum coke	70-85	15-20	1.35	0.5-0.7	Medium-hard, medium-pore volume	[31]
Semi-hard coal	70-75	10-15	1.45	5-15	Hard, large-pore volume	[31]
Hard coal	85-95	5-15	1.5-1.8	2-15	Hard, large-pore volume	[31]

## 2.8 Activated carbon production

The carbon production method has several processes. The convert of biomass can be synthesis with activation or non-activation method. Initial carbon production desire supplementary treatment before activation treatment for enhancing porosity. Commonly, the biomass can convert via the hydrothermal, template-directed method and including direct thermal treatment. Hydrothermal ordinarily is the reaction of biomass with water under thermal treatment and self-generated pressure. In contrast, the template-directed method impregnates the biomass into the template following by carbonization. Certainly, the template is eliminated with a solvent such as hydrogen fluoride to obtain carbon material with a similar pore size distribution, but the disadvantage is the low interaction between carbon precursor and template [32, 33]. Moreover, direct carbonization or pyrolysis operates under the inert condition, which biomass is straight converted into the porous structure without additional with solvent. Nevertheless, the specific surface area of the activated carbon produce via this method provides the low specific surface area (below 600 or 100 m<sup>2</sup>/g) [34, 35]. Hence, the activation will improve the specific surface area and pore volume of the carbon material.

### 1) Hydrothermal

Hydrothermal is a thermochemical process, which the water uses as the intermediate for converting lignocellulose to hydrochar solid. Moreover, the

hydrothermal also releases the gaseous product, liquid bio-oil. The reaction mechanism relates to hydrolysis, dehydration, decarboxylation, condensation and aromatization reactions. The glycosidic group is decomposed via hydrolysis reaction, in which the water molecule will break cellulose and hemicellulose of the biomass. While almost lignin unchanged because of stable structure. The main hydrothermal process parameters are operating temperature, duration time, and pressure. Usually, hydrothermal are treated at high temperatures (300–800°C) and low temperatures (200–250°C) while the pressure are generated to avoid the evaporation of the water molecules during the reaction. However, low-temperature reaction is more eco-friendly because its power-saving and fewer chemical conversions [36-38].

#### 2.1.1 Activation process

Activation process can improve the quality of activated carbon, which enhances the surface area and pore volume of hydrochar or biomass. The feedstocks are use hydrochar or biomass. The activated process can produce the specific surface area about 4–50 times when compares to non-activated. The activation method can be classified as physical and chemical activation as follows.

##### 1) Chemical activation

Chemical activation is more beneficial than physical activation about high activated carbon yield, shorter duration time and higher porosity since it reduces tar content. Chemical activation generates activated carbon with wider size distributions and higher amount of mesopores since activating agent infiltrate into pore structure, causing the pores to shrink less than physical activation. Lignocellulose is soaked with chemical agents activating and then followed by carbonization at temperatures in the range of 450-900°C to obtain activated carbon. A variety of chemicals commonly uses as activating agents such as zinc chloride ( $ZnCl_2$ ), potassium hydroxide (KOH), sodium hydroxide (NaOH), sulphuric acid ( $H_2SO_4$ ) and phosphoric acid ( $H_3PO_4$ ), which expresses the role of template for pore formation. Chemical activation may have problems with chemical residues in activated carbon [39, 40].

##### 2) Physical activation

Physical activation is a two steps process. The first step, pyrolysis of hydrochar or lignocellulose in the range 600-900°C in absence of  $O_2$  follow by

gasification of the char at the temperature range 600-1200°C in the presence of carbon dioxide (CO<sub>2</sub>), steam or mixing gas. When comparing the performance of the activating gas, it shows that the steam is superior to carbon dioxide. The steam can better entrance and generate the pore since molecule smaller than CO<sub>2</sub>, broad pore size distribution and high surface area. Typically, activated carbon is synthesized by physical activation, which has a microporous structure and narrower pore size distribution [41, 42].

## **2.9 Biomass conversion technology**

Biomass is commonly used as a source for activated carbon because it has non-toxic, biodegradable, and higher surface areas. Biomass is obtained from agricultural wastes such as harvesting and oil extraction. Biomass waste is a useless material that is cheap and affects the environment. Biomass contains carbonate, which can be converted into high-efficiency carbon materials. Typically, biomass is a complicated fiber-matrix composite material composed of biopolymers that the fiber framework consists of crystallite cellulose micro-fibrils, 2-5 nm diameter. The matrix between the micro-fibrils is formed primarily of hemicellulose, and lignin improves the strengthening fiber that reinforces the neighboring cell wall.

### Hemicelluloses

Hemicelluloses compose of polymer chains with short branches and amorphous structures, which are partially solvable or solvable in water. The backbone of hemicelluloses classified as a homopolymer (sugar repeat unit) or a heteropolymer (composite of several sugars). Formulas of the sugar component of hemicelluloses [43].

### Lignin

Lignin is a complicated structure with a large molecular structure, which are cross-linked polymer. Lignin enhances the mechanical strength of wood by sticking the fibers together (reinforcing agent) attaching the cell walls. It is normally connected with the cellulose and hemicellulose to produce lignocellulosic biomass.

### Celluloses

Cellulose is a representative of carbohydrates and polysaccharides, which high molecular weight contain glucose linked to glycosides. The main structure of

plant cell walls is mainly cellulose, such as wood, bark, fruit and grains. Cellulose structure merges with pectin and hemicellulose. In addition, the cellulose structure is a rich source of carbon.

**Table 2.5** shows the composition of lignocellulose in biomass. Lignocellulose materials are generally used as the precursor for production of activated carbon such as coconut shell, rice straw, hardwood, and sugarcane bagasse etc. These materials composed of low hemicellulose and high cellulose content, which decreases the lost yield product.

**Table 2.5** the composition of lignocellulose in biomass

Biomass	Celluloses (%)	Hemicelluloses (%)	Lignin (%)	Ref
Cattail leave	63	8.7	9.6	[43]
Rice straw	32-41	15-24	10-18	[43]
Hardwood	40-45	18-40	18-28	[43]
Bagasse	26-56	24-34	10-26	[43]
Coconut shell	30.58	26.70	33.30	[43]
Wheat straw	30	50	15	[43]

## 2.10 Pore characteristic of activated carbon

Porous material has an extensive range of diameter for application. Classification of pores is one of the main requirements of a general investigation of porous material, which are classified by using criteria given to the pore size of the porous material. IUPAC is standard to determine the pore size ranges depend on various diameter, which the classification of various pore types are defined as follows: [44]

- Microporous material define the pore diameter less than 2 nanometers
- Mesoporous materials define the pore diameter between 2 to 50 nm.
- Macroporous materials define the pore diameter of greater than 50 nm.

The exothermic reaction occurs in adsorption isotherm for investigating the adsorption behavior through the curve. The absorption equilibrium study mostly starts with the classification of temperature. This classification of the pore is essential



for theoretical that describes adsorption phenomena. BET method can explain the surface area. Nevertheless, the IUPAC will imply the isotherm type leads to describe the behavior of the adsorption. Classification of Isotherm has separated 6 types according to IUPAC standard, as shown in **Figure 2.4**. [45]

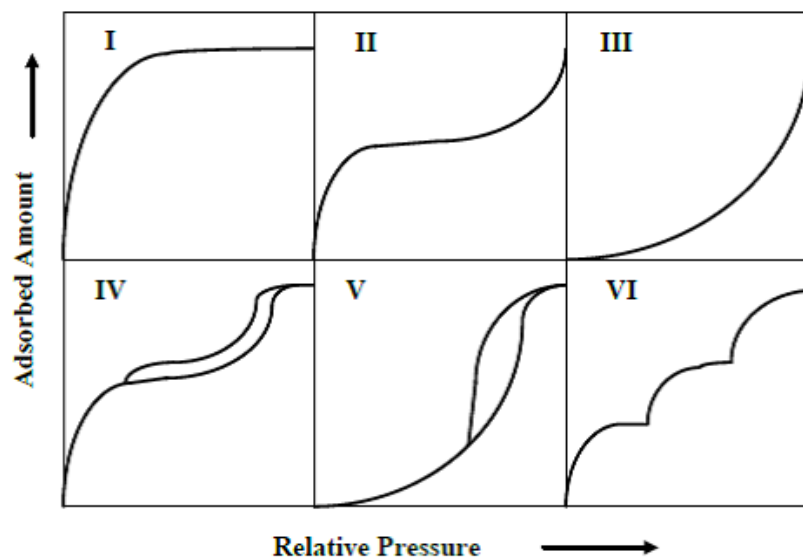


**Figure 2.4** Types of physisorption isotherms according to the IUPAC classification

Type I represents microporous materials. Adsorption of monolayer has a chemisorption behavior, which refers to Langmuir isotherm. The amount of gas adsorption quickly rises under relative pressures ( $P/P_0$ ). The isotherm adsorption increases slightly when the relative pressure approximates 1 because the pores are saturated with molecules gas. The material absorbs gas in small size pores (pore widths below 2 nm) such as activated carbon and zeolites.

Type II represents s-shape isotherm, which typically identified fewer porosity materials or macroporous materials. The behavior of isotherm is physical adsorption that capillary and pore condensation occur when relative pressure approach 1. The complete adsorption of monolayer exhibits the knee curve or inflection point at relatively low values of  $P/P_0$  (0.1 to 0.3). When the relative pressure is higher, the gas molecules adsorb on the monolayer, known as a multilayer adsorption process.

Type III represents isotherm as a concave lens curve, which are typical of nonporous materials. The adsorption of monolayer are weak attractive forces.

Type IV represents mesoporous structures (pore widths from 2 to 50 nm) because the isotherm shows hysteresis loops associated with pore capillary condensation. Surface curvature on vapor pressure provides adsorption-desorption isotherm at the hysteresis loop. The first step of the isotherm, adsorption at low relative pressure exhibits similar to type II, while the adsorption rapidly raises at high relative pressure.

Type V nearly the same Type IV isotherm and is are similar to type III because the attractive forces of monolayer adsorption that are relatively weak.

Type VI is a stepped isotherm according to the layer to layer adsorption. The curve of isotherm bases on the relative pressure and adsorption temperature. Typically, the gas are adsorbed at temperature is close to the melting point.

### **2.11 Literature reviews**

In this reviews, the associated information partial hydrogenation of soybean FAME to H-FAME using supported metal catalysts has been suggested. Furthermore, the synthesis of activated carbon from biomass and its use as a supporting material of catalyst has been reviewed.

Transportation is an essential part of the economic extension in the world since the transportation sector consume large amounts of fossil fuel energy such as gasoline and diesel fuel. The import of petroleum-based fuel tends to rise each year resulting in enormous budget losses. In addition, the combustion of these fuels release pollutant into the environment ( $\text{CO}_2$ , CO,  $\text{SO}_2$ , PM and HC). Hence, biofuel can be used to replace petroleum-based fuels. In particular, biodiesel is fuel for diesel engines with the advantages of oxygenated, environment-friendly and non-toxic. Nevertheless, In Thailand is restricted to a 7 % blend ratio of biodiesel fuel because the injector and the engine system can damage from higher blend ratio. This problem has reason from the biodiesel with a high amount of polyunsaturated FAME, which is easily oxidized to form slurry-like deposits and clogged the injector or fuel filter. Also, biodiesel may contain acids and water, which can lead to engine corrosion. To overcome this problem, researchers have studied biodiesel partial

hydrogenation of polyunsaturated FAME, which improve oxidation stability. Besides, partial hydrogenation slightly affects the cold flow properties because it operates at low temperature and pressure. However, mild condition provides low conversion of polyunsaturated FAME. Hence, a catalyst is required to obtain the desired product, which depends on the activity and selectivity of cis-isomer. Many researchers report that the most excellent catalytic activity in hydrogenation used noble metals (e.g. Pd and Pt) over  $\text{Al}_2\text{O}_3$ , zeolites,  $\text{SiO}_2$ , MCM-41 and AC supported. The overview of current studies about this focus are summarized in all ideas.

Artita N. R. et al. [46] studied that Pd/MCM-41-silatrane shown a higher catalytic activity (TOF) than Pd/MCM-41- $\text{SiO}_2$  for the partial hydrogenation of soybean biodiesel at  $100^\circ\text{C}$  and 0.4 MPa  $\text{H}_2$  within 4 h because Pd particles on MCM-41- $\text{SiO}_2$  presented preferable metal distribution than Pd/MCM-41-silatrane as shown in **Table 2.6**. Pd/MCM-41- $\text{SiO}_2$  catalyst revealed the dispersion of smaller Pd particles that interact more stably with MCM-4- $\text{SiO}_2$  support. Moreover, **Table 2.7** shown the Pd particle size 12.7 nm organized on the outer surface and migrated into some pores. It can be indicated to the Pd particles, which appear internal enough large pore channels of the  $\text{SiO}_2$  support, provide a higher C18:0 (greater degree of complete hydrogenation) and trans-C18:1 isomer. Although Pd/MCM-41- $\text{SiO}_2$  catalyst enhances the higher oxidative stability, the cloud point revealed a poor than Pd/MCM-41-silatrane.

**Table 2.6** Physical properties of the support and Pd catalyst

	MCM-41- $\text{SiO}_2$ support	MCM-41-silatrane support	Pd/MCM-41- $\text{SiO}_2$	Pd/MCM-41-silatrane	Pd(0.5)/ MCM-41- $\text{SiO}_2$	Pd(1)/ MCM-41- $\text{SiO}_2$	Pd(2)/ MCM-41- $\text{SiO}_2$
Surface area ( $\text{m}^2/\text{g}$ )	1342	1,215	655.3	720.4	956.5	740.3	834.6
Pore volume ( $\text{cm}^3/\text{g}$ )	1.75	0.92	1.42	0.46	1.56	0.53	1.20
Pore diameter (nm)	2.5	2.5	1.0	1.7	1.0	1.0	1.0
Metal dispersion (%)	-	-	3.82	2.17	4.31	3.69	2.46
Pd particle size (nm)	-	-	12.7	22.4	11.3	13.1	19.7

**Table 2.7** FAME compositions, TOFs, and ratio of trans/cis C18:1 of Pd/MCM-41-SiO<sub>2</sub> and Pd/MCM-41-silatrane.

	Feed	At C18:2 conversion 40%		At C18:2 conversion 60%	
		Pd/MCM-41-SiO <sub>2</sub>	Pd/MCM-41-silatrane	Pd/MCM-41-SiO <sub>2</sub>	Pd/MCM-41-silatrane
FAME composition					
C18:2 (wt.%)	50.95	30.54	29.95	20.69	20.00
C18:3 (wt.%)	5.43	1.18	0.97	0.30	0.29
C18:1 (wt.%)	29.16	45.54	45.79	57.44	55.21
– <i>Trans</i>	–	7.19	7.77	11.55	11.27
– <i>Cis</i>	25.16	38.19	37.99	45.67	44.05
C18:0 (wt.%)	3.68	4.74	4.41	5.48	4.62
TOF ( $\times 10^4 \text{ h}^{-1}$ )	–	2.42	2.48	2.38	2.52
Degree of complete Hydrogenation (%)	–	2.33	1.59	3.13	1.70
Ratio of <i>trans/cis</i> C18:1	–	0.19	0.20	0.25	0.26

Natthida N. et al. [47] study the partial hydrogenation of rapeseed BDF in a batch reactor under the reaction conditions of 80°C, 0.3 MPa and 200 ml/min H<sub>2</sub> flow rate. The catalyst was prepared by incipient wetness impregnation, calcined at 300°C for 3 h, and reduced at 300°C for 2 h. Pd/Al<sub>2</sub>O<sub>3</sub> revealed high sulfur inhibitory than Pd/SiO<sub>2</sub>-Al<sub>2</sub>O<sub>3</sub> because stronger acidic site provide an electron deficit of Pd metal. The acidic supports a higher degree of S tolerance because the strong adsorption between Al<sub>2</sub>O<sub>3</sub> and reactants that blocked the entrance of sulfur to the Pd surface. Besides, the selectivity of cis-unsaturated FAME could enhance by acidic supports and the addition of S. Moreover, Improving oxidative stability from 1.89 h to 33.48 h after 1 h of hydrogenation reaction. In contrast, the cloud point and pour point of H-FAME were worse at the temperature of -3 to 15°C and from -11 to 12°C, respectively.

Natthida N. et. al [48] reported that 2 wt.% Pd/C catalyst provides good partial hydrogenation activity. **Figure 2.5** showed the behavior of consecutive reactions from C18:3 to C18:2, C18:1, and C18:0. The partial hydrogenation of C18:2 and C18:3 in a batch reactor produced higher selectivity of C18:1 than the continuous flow reactor while the selectivity of C18:1 of both reactors was similar at the low conversion (78%). Although, the batch reactor is high conversion and high selectivity towards C18:1, the continuous flow reactor enhanced conversion rates 4-5 times greater than in a batch reactor. It can describe that the oil contact with the catalyst surface in a continuous flow reactor is higher than the batch reactor. However, a continuous flow reactor is more useful because it was the lower operating time when compared to the batch reactor.

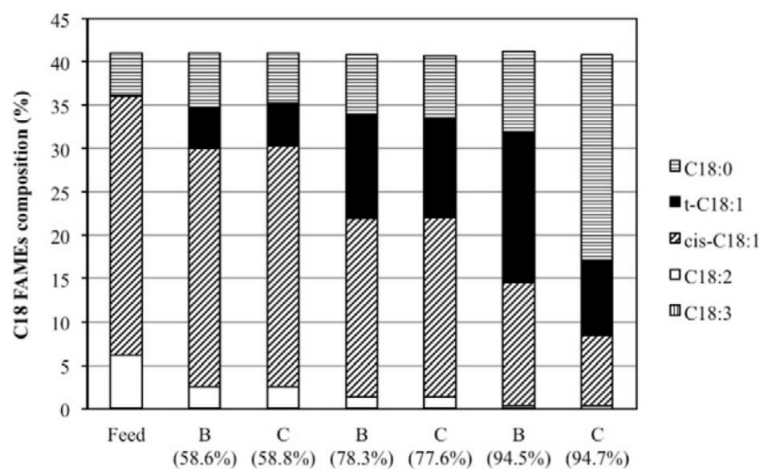


**Figure 2.5** Composition of biodiesel feed and H-FAME derived from batch (B) and continuous-flow (C) reactors at different conversions of C18:2 and C18:3

Although Pd catalyst as an excellent selection for partial hydrogenation enhanced high hydrogenation activity, it is sensitive to poison in the feedstock. Deactivation of catalyst based on the acidity of the support, and the size and electronic property of Pd particles. Moreover, the noble metal is costly than transition metal catalyst (e.g., Ni, Cu, Co, Mo, and W), which is interesting in the hydrogenation reaction. Many researchers have investigated the potentiality of transition metal catalyst.

Jakkrapong J. et al. [49] investigated the 10 wt% Ni/SiO<sub>2</sub> catalyst prepared by incipient wetness impregnation was employed as a catalyst for partial hydrogenation at 100°C for 4 h for upgrading the waste cooking oil biodiesel. The researcher reported that the Ni catalyst had raised the selectivity of both cis-monounsaturated and trans-monounsaturated FAME. The highest TOF (TOF=486 h<sup>-1</sup>) revealed at 1 h because it had a high amount of active Ni vacancies. TOF value (TOF=203 h<sup>-1</sup>) reduced at 4 h because the deactivation of catalyst slightly decreased the performance. Furthermore, Ni/SiO<sub>2</sub> catalyst can enhance the biodiesel yield from 97.56 % of waste cooking oil biodiesel to 98.09 % of hydrogenated FAME.

Ni catalyst enhanced the activity in hydrogenation reactions at low hydrogen concentration, which significantly promoted the selectivity of cis isomer and easily separated from the product by filtration. However, Ni catalyst provided a low conversion and short lifetime [50]. It well knows that the behavior of Ni is high

selectivity of saturated stearic acid (C18:0), which affected to lubricants of hydrogenated biodiesel. A.F. Trasarti et al [51] reported that Cu/SiO<sub>2</sub> catalyst has efficiently improve liquid-phase soybean oil hydrogenation. Cu/SiO<sub>2</sub> catalyst was selectively hydrogenated C18:3 and C18:2 to monounsaturated C18:1, without formation stearic acid (C18:0). It could improve oxidation stability while keeping cold flow properties. Nevertheless, the hydrogenated activity slightly decreased because Cu particles highly agglomerated into the pore and reduced mass-transfer between oil and catalyst. Therefore, the large porous structure of silica affects the access of oil molecules.

Problems of monometallic catalysts involved low activity and selectivity of cis-isomer content in hydrogenated biodiesel. Many researchers studied to improve the bimetallic catalyst because the second metal can modify the perfect geometric structure and electronic effect of catalyst. Metals were interesting in promoting a catalyst such as Mo, Pb, V, Ag and Ni, which are reported as follows:

Shane M. et al. [52] studied the hydrogenation of sunflower oil over the PtNi/SiO<sub>2</sub> under H<sub>2</sub> pressure 3 bar and operating at 200°C for 2–3 h. PtNi/SiO<sub>2</sub> catalyst was the favorable influence on the selectivity of C18:1 because PtNi/SiO<sub>2</sub> catalyst provided 23 % trans C18:1 content compared to Pt/SiO<sub>2</sub> generate 26.5% trans C18:1. Ni as inactive sites could prevent the high active Pt particles, which decrease the activity of the catalyst. Ni element in the structure exhibited weak interaction between C18:1 and the catalysts. In typical, the performance of the PtNi/SiO<sub>2</sub> catalysts similar to the monometallic Pt/SiO<sub>2</sub> catalyst, which both Pt and Ni atoms were individual monometallic particles.

María B.F. et. al. [53] reported that Pd-Mo/ $\gamma$ -Al<sub>2</sub>O<sub>3</sub> and Pd-V/ $\gamma$ -Al<sub>2</sub>O<sub>3</sub> catalysts provided a similar activity compared with the corresponding Pd monometallic catalyst, and enhance the selectivity toward trans-isomers. The Mo and V facilitated to generate the adsorbed initial state after the hydrogenation occurred on the Pd surface. In contrast, Pd-Pb/-Al<sub>2</sub>O<sub>3</sub> revealed the worst hydrogenation activity because Pd formed Pd-Pb alloy structure with dimensional limitations of space lattice for

hydrogenation of double bonds. Pd-Mo/ $\gamma$ -Al<sub>2</sub>O<sub>3</sub> catalyst was the most performance catalyst for the selectivity of cis-isomers.

Chachchaya T. et al. [54] studied PdMg/SiO<sub>2</sub>, NiMg/SiO<sub>2</sub> and PtMg/SiO<sub>2</sub> catalyst for partial hydrogenation of soybean biodiesel at 80–120°C. under 4 bar H<sub>2</sub> pressure. Pd-Mg/SiO<sub>2</sub> and Pt-Mg/SiO<sub>2</sub> provide higher the conversion of C18:3 and C18:2 when compare to without Mg modifying. In contrast, Ni-Mg/SiO<sub>2</sub> exhibited lower conversion because Ni catalyst significantly working under strong conditions. Pd-Mg/SiO<sub>2</sub> remarkably improved the selectivity of cis-C18:1 because Mg could promote electron transfer from the support to the metal result in strong metal-support adsorption. For this reason, it reduces the production of trans-C18:1, which exhibited excellent oxidative stability than the catalysts without Mg modify.

Yue Z. et al. [55] report that Cu-Ag/SBA 15 catalyst was higher selectivity of C18:2 about 1.8 times than with Cu-Pd/SBA15 for hydrogenation of soybean oil. Ni-Ag/SBA 15 catalyst the selectivity of the C18:2 about 1.3 times higher than with Cu-Pd/SBA15. This clearly described that the precious metal promoter was useful in enhancing the distribution of the primary catalyst in the carrier and efficiently decreased the production of trans isomer. Ni-Ag/SBA 15 provided the content of oleic acid was to 50.27% and the content of TFA was lower to 10.43%.

Although active sites influence the catalytic activity and selectivity of cis isomers, the pore size of support also has a significant effect on the catalyst dispersion and mass transfer of oil molecules. In previous researches, the use of supporting materials is an inorganic material with a low surface area (100-300 m<sup>2</sup>/g) and pore size, such as zeolite, silica and alumina. It causes hydrogenation reactions around the pore mouth, because the pores are narrow. Carbon material is interesting for partial hydrogenation because the surface area is up to 1000 m<sup>2</sup>/g and pore size in the range of 2-50 nm. Activated carbon synthesized from biomass was popularly employed as a support for several research fields. Hence, studying the conditions for the production of activated carbon, including parameters such as temperature, residence time and chemical activation processes that control the properties of the

activated carbon products. Many researchers investigated the production of activated carbon from agricultural residues following the literature below.

I. Ghouma et al. [56] studied the adsorption capacity and  $\text{NO}_x$  reduction of activated carbon from olive seed that generated the pore structure via chemical activation with  $\text{H}_3\text{PO}_4$  and physical with steam and carbon dioxide under the reaction temperature conditions (180, 220 and 260 ° C) and reaction time (2, 4 and 6 hours). Activated carbon has been studied for structural and chemical properties with analyzers as follows SEM, XPS, XRD, CHNS elemental analyzer, NMR and Raman. It was found that the steam activation method generally developed mesopore, which provided the highest  $\text{NO}_x$  gas adsorption capacity. The phosphoric acid activation mostly generated micropore and the highest  $\text{NO}_2$  reduction capability because it formed anhydride acid function group.

S.M. Yakout et al. [57] studied the concentration of phosphoric acid (60 wt%, 70 wt% and 80 wt%) affects the pore structure and the surface chemical properties of the activated carbon from the olive stone. Activated carbon was analyzed using  $\text{N}_2$  adsorption technique at 77 K, indicating that pore size, pore volume and surface area enhanced when the concentration of phosphoric acid increased, which can generate microporosity. **Table 2.8** shows the physical properties of activated carbon using phosphoric acid with a concentration of 80 wt% enhanced surface area ( $S_{\text{BET}}$ ) up to  $1218 \text{ m}^2\text{g}^{-1}$ , pore volume ( $V_{\text{total}}$ )  $0.6 \text{ cm}^3\text{g}^{-1}$  and pore size ( $r$ ) 1.3. nm

**Table 2.8** Physical properties of activated carbon from olive stones

Carbon	$S_{\text{BET}}$ ( $\text{m}^2/\text{g}$ )	$r$ (nm)	$V_{\text{total}}$ ( $\text{cc}/\text{g}$ )	$V_{\text{micro}}$ ( $\text{cc}/\text{g}$ )	$V_{\text{meso}}$ ( $\text{cc}/\text{g}$ )
OS6	257	0.954	0.123	0.11	0.012
OS7	779	1.0	0.35	0.32	0.03
OS8	1218	1.1	0.6	0.5	0.1

X. Jin et al. [58] studied the chemical activation with  $\text{K}_2\text{CO}_3$  and KOH (40 % solution) using different ratios for the preparation of activated carbon from lignin. Activated carbon was synthesized by soaking for 16 hours and carbonization at 500-900 ° C for 20-50 min. **Table 2.9** shows the activated carbon was investigated properties by BET and Iodine number technique. It observed that activated carbon with  $\text{K}_2\text{CO}_3$  at 800 ° C for 50 min was more effective for the absorption of methyl blue



and iodine than activated by KOH at the same conditions under the temperature of more than 600 °C leads to the elimination of CO and generated a larger surface area.

**Table 2.9** Physical properties and dye absorption of activated carbon

Chemical agents	$S_{\text{BET}}$ ( $\text{m}^2/\text{g}$ )	Non-microporous surface ( $\text{m}^2/\text{g}$ )	Pore diameter (nm)	Methylene blue ( $\text{mL}/0.1 \text{ g}$ )	Iodine ( $\text{m}^2/\text{g}$ )	% Yield
$\text{K}_2\text{CO}_3$	1104	417	2	10.6	1310	19.8
KOH	917	213	2.5	9.6	1180	18.7

Azadeh B.N et al. [59] studied the chemical activation with NaOH and KOH of pulp under the conditions of reaction temperature 600-1000°C, reaction time 1.5 h and ratio of chemicals to carbon 2:1, 3:1, 1:1. **Table 2.10** indicated that the increased temperature generated high surface area. On the contrary, the surface area reduced when the activation temperature reaches 1,000 °C because of the collapse of the pores. Also, the ratio of chemicals to carbon 1: 1 was insufficient to generate a high surface area. NaOH and KOH generated activated carbon with a surface area of 2600 and 1600 square  $\text{m}^2\text{g}^{-1}$ , respectively and activation yield 50% and 48%, respectively. Hence, NaOH was significantly more effective compared to KOH.

**Table 2.10** Effect of activation condition and physical properties of activated carbon

Activation temperature	NaOH:C impregnation ratio	Activation time (h)	SSA ( $\text{m}^2 \cdot \text{g}^{-1}$ )	Activation yield (%)	Pore volume ( $\text{cm}^3 \cdot \text{g}^{-1}$ )	Micropore volume ( $\text{cm}^3 \cdot \text{g}^{-1}$ )	Mesopore volume ( $\text{cm}^3 \cdot \text{g}^{-1}$ )
800 °C	2:1	<b>1</b>	2100	52	1.19	0.64	0.55
800 °C	2:1	<b>1.5</b>	2600	50	1.33	0.62	0.69
800 °C	<b>3:1</b>	2	2300	46	1.12	0.56	0.55
800 °C	<b>2:1</b>	<b>2</b>	2300	49	1.17	0.55	0.62
800 °C	<b>1:1</b>	2	500	76	0.63	0.42	0.21
<b>600 °C</b>	2:1	2	2100	48	1.54	0.75	0.79
<b>1000 °C</b>	2:1	2	600	54	0.50	0.11	0.39

R. Acosta et al. [60] studied the chemical activation of pyrolysis oil with KOH for the production of activated carbon using the activation temperature of 600 - 800°C. BET, CHNS The maximum surface area derived from the BET analysis was 814  $\text{m}^2\text{g}^{-1}$  for the KOH activated carbon at 800 °C under  $\text{N}_2$ . Increasing the temperature activation provided the oxidizing potassium hydroxide to potassium (K), while the

substrate reduces to CO and CO<sub>2</sub>, which increases the mesoporous. Including increasing the chemical ratio provided carbon yield decreased.



## CHAPTER 3

### RESEARCH METHODOLOGY

#### 3.1 Preparation of activated carbon

Cattail leave (CL) were derived from Ladkrabang, dried at ambient temperature to constant weight. The dried CL were cut and crushed to powder. Then, The CL powder were sieved to separate the particle size of 2  $\mu\text{m}$ . The sieved CL 30 g and DI water 60 ml were packed into the autoclave for hydrothermal at 200°C for 12 h under self-generated pressure. After the finish reaction, the autoclave quickly was cooled to room temperature. The hydrochar (HC) were dried to eliminate moisture in the oven at 90°C for 12 h. The dried HC 10 g were stirred at 80°C in 100 ml of  $\text{H}_2\text{SO}_4$ ,  $\text{H}_3\text{PO}_4$ , KOH and NaOH solution with a concentration of 2 M, 4 M, and 6 M. The mixture of HC were filtered through Buchner funnel with the vacuum pump, then were dried to evaporate the solution. The dried HC were placed in the heat zone position within the horizontal tube furnace (**Figure 3.1**) using a nitrogen flow rate of 100 ml/min. The sample were kept at different temperatures (500°C, 700°C, and 900°C) for 2 h with heating rate 10°C/min. Finally, activated carbon severally were washed with 0.5 M HCl and distilled water until neutral [61, 62].

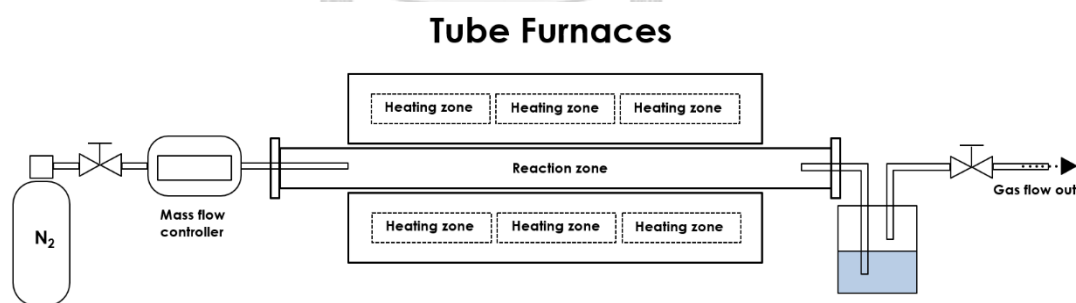


**Figure 3.1** Schematic diagram of Horizontal tube furnace for chemical activation of Cattail leave to produce activated carbon

#### Characterization

As-prepared activated carbon has been investigated by proximate and ultimate analysis, scanning electron microscope (SEM), Fourier transform infrared spectroscopy (FTIR) and Nitrogen sorption to investigate the characteristic of the AC

to produce as catalyst support. The specification of the characterization techniques are explained as follows,

### 3.1.1 Proximate and ultimate analysis

Proximate analysis usually is used for the characterization composition of activated carbon and biomass by thermogravimetric, which loss of weight can explicate from thermal degradation of the sample under inert or oxygen gas. The composition of carbon consists of moisture, ash, and volatile matter and fixed carbon content. Traditionally, the moisture content indicates the mass of water in dry samples which are determined by ASTM E-871 method (ASTM, 2014). Volatile matter evaporates into organic compounds such as CO, H<sub>2</sub>, and CH<sub>4</sub>. ASTM E-872 and ASTM E-1755 is the method for the measurement of the volatile matter in the sample. Ash means the inorganic compound, which residual remains after complete oxidization of the sample. Ash content is analyzed with D-1102 or UNE-EN 14775 [63]. Fixed carbon content defined by difference using the balance following this equation: %FC = 100-%M%VM-%A [64]. The dried sample 0.1 g was heated 2 steps. First, the temperature was heated from 30 to 800°C with ramp rate 10 °C/min under N<sub>2</sub> atmosphere for pyrolysis and to remove the volatile and moisture. Finally, the inert gas was replaced with an air atmosphere and the sample were oxidized after 800 to 1000°C for combustion. [65]

Ultimate analysis estimates the composition of activated carbon, solid or gaseous, which is expressed in the form of proportions of chemical element. Amount of carbon (C), hydrogen (H), oxygen (O), Nitrogen (N) determined by using CHN elemental analyzer (CHNS628 series). The amount of the carbon includes combustion of gas released from organic substances. The amount of hydrogen also involves the organic coal that is present in the form of moisture and water [64]. The different of all composition can calculate the oxygen percentage, and the following formula directly obtains that of oxygen as shown: O = 100 - (C + H + N) [66]. The sample 5 mg quickly burned from 30 to 950 °C with heating rate 10 °C/min under He and O<sub>2</sub> atmosphere.

### 3.1.2 Surface characteristics

The porosity and pore structure of activated carbon can be measured by using nitrogen sorption. Brunauer–Emmett–Teller (BET model) commonly calculates the BET surface area ( $S_{\text{BET}}$ ). Pore size distribution was obtained through the BJH model. The amount of nitrogen adsorbed on solid surfaces operated at 77 K of liquid nitrogen. The relative pressure is in the range of 0.05–0.35, which is fit for Brunauer–Emmett–Teller (BET) equations, where  $P$  is the partial pressure of nitrogen and  $P_0$  is the saturated vapor pressure of nitrogen. [67] The micropore volume ( $V_{\text{mic}}$ ) can be tested through the t-plot model. The total pore volume ( $V_{\text{t}}$ ) was estimated by capillary condensation of liquid at the relative pressure of 0.99. Mesopore volume ( $V_{\text{mes}}$ ) is calculated by the difference between micropore volume and total pore volume. The sample (0.01 g) was dried at 90°C overnight and carried into the sample cell, followed by closing with seal fit. Nitrogen gas was adsorbed until the full pore after that the sample was degassed at 250°C to remove gas. Finally, the software computed the parameter by the theoretical model.

### 3.1.3 Surface functional and morphology analysis

Fourier transform infrared (FTIR) spectroscopy investigates the structure of an unknown from the vibration bond of organic or inorganic molecules while absorbing waves in the middle infrared range [68]. A surface functional group was analyzed by PerkinElmer UATR Two using ATR transmission mode. IR scan in the range of 400 to 4000  $\text{cm}^{-1}$  with a scan rate of 8 cycles. The powder was pressed into a flat plate on ATR crystal material such as diamond.

Scanning electron microscope (SEM) was used to analyze the morphology by EVO MA10. The sample was taped on a carbon tape that stuck on specimen stubs and coated with gold (Au) under a vacuum atmosphere by sputtering to enhance the conductive surface. The coated sample was scanned by the secondary electron with operating at 10 kV. The magnification of electron beam was 500x, 1000x, and 2000x, which electron was focused into a small beam to generate the high-resolution images.

### 3.2 Catalyst preparation

Activated carbon with KOH 4 M at 900°C were used as support material for catalyst loading. Ammonium molybdate  $[(\text{NH}_4)_6\text{Mo}_7\text{O}_{24}\cdot 4\text{H}_2\text{O}]$ , Nickel (II) nitrate  $[\text{Ni}(\text{NO}_3)_2\cdot 6\text{H}_2\text{O}]$ , Copper (II) nitrate hexahydrate  $[(\text{Cu}(\text{NO}_3)_2)\cdot 6\text{H}_2\text{O}]$ , and Iron (III) nitrate hexahydrate  $[(\text{Fe}(\text{NO}_3)_3)\cdot 9\text{H}_2\text{O}]$ , purity "≥ " 98 were used as precursor of metal. Catalyst were synthesized by wet impregnation and reflux. 50 ml The monometallic catalyst were impregnated metal 10 wt% for Mo, Ni, Cu, and Fe catalyst, which precursor solution were mixed with activated carbon 5 g at 60°C and dried by a rotary evaporator with vacuum atmospheres until completely evaporation. Then, catalyst were calcined at 500°C for 3 h under  $\text{N}_2$ . The bimetallic catalyst were synthesized with various metal loading ratio of 2.5:7.5, 5:5 and 7.5:2:5 wt.% with 2 step. First, ammonium molybdate  $[(\text{NH}_4)_6\text{Mo}_7\text{O}_{24}\cdot 4\text{H}_2\text{O}]$  50 ml were refluxed with activated carbon 5 g at 60°C, dried by a rotary evaporator with vacuum atmospheres until completely evaporation and calcined at 500°C for 2 h under nitrogen using a ramping rate of 5 °C/min. for 2.5 wt.%, 5 wt.%, and 5 wt.% Mo catalyst. Next, Nickel (II) nitrate  $[\text{Ni}(\text{NO}_3)_2\cdot 6\text{H}_2\text{O}]$ , Copper (II) nitrate hexahydrate  $[(\text{Cu}(\text{NO}_3)_2)\cdot 6\text{H}_2\text{O}]$ , and Iron (III) nitrate hexahydrate  $[(\text{Fe}(\text{NO}_3)_3)\cdot 9\text{H}_2\text{O}]$ , purity "≥ " 98 were impregnated on Mo/C by rotary evaporator at 60°C and calcined at 600°C for 2 h using a ramping rate of 5 °C/min under nitrogen to obtain Mo:Me (Me = Ni, Cu, and Fe) catalyst with 5:5 wt.% ratio.

#### Catalyst characterization

The prepared catalyst has been studied using different techniques, such as X-ray diffraction (XRD), scanning electron microscope-energy dispersive spectrometry (SEM-EDS),  $\text{N}_2$  adsorption/desorption and temperature programmed reduction (TPR), CO chemisorption to examine the attributes of the catalyst for partial hydrogenation of soybean oils, which will be described in detail as follows,

##### 3.2.1 X-ray diffraction (XRD)

The x-ray diffraction technique was used to investigate the information about critical features such as phase identification, crystal structure and crystallite size of prepared catalyst. X-ray diffractogram obtained by Rigaku SmartLab X-ray

diffractometer with Guidance software. The source of x-ray is Cu-K $\alpha$  radiation ( $\lambda = 1.5418 \text{ \AA}$ ) with an accelerating voltage of 40 kV and the current of 40 mA. X-ray sources and detectors scanned from 10 to 90° with theta-2-theta mode in steps of 0.02°/s. The Debye–Scherrer equation can determine the average crystallite size of catalyst.

### 3.2.2 Energy dispersive spectrometry (EDS)

The elemental composition of the catalyst is mostly used for qualitative analysis from X-rays fluorescent. Energy dispersive spectrometry was installed with SEM. Moreover, EDS contributed information about the distribution of catalyst from the EDS mapping mode, including the atomic ratio of elemental.

### 3.2.3 H<sub>2</sub> temperature-programmed reduction (H<sub>2</sub>-TPR)

H<sub>2</sub>-TPR technique operated by TP-5000-II with a thermal conductivity detector (TCD). Before investigates, the catalysts of 0.1 g and quartz wool of 0.03 g were put in a U-quartz tube reactor and pretreated under a N<sub>2</sub> steam with a flow rate of 25 mL/min using heating rate 10°C/min. The samples were hold at 300°C for 1 h to remove impurity and then cooled to room temperature. H<sub>2</sub> flowed through the sample while it was being heated from 30°C to 800°C at a heating rate of 10 °C/min in 25 mL/min H<sub>2</sub> flow for 30 min. Final the sample was cooled down to 25°C to obtain product.

### 3.2.4 CO chemisorption

Metal dispersion of catalysts were performed using an Ohkura Riken R6015-S that were represented as the ratio of the total number of metal atoms on the metal surface. Metal dispersion were calculated by assuming a CO to surface metal atom ratio of 1:1 [69]. Quartz wool 0.03 g and catalyst 0.1 g contained in a U-quartz tube reactor. Samples were reduced at the same temperature as the H<sub>2</sub>-TPR technique in H<sub>2</sub> flow rate 25 mL/min with heating rate 10°C/min for 3 h and then cooled to 25 °C in a nitrogen flow. The CO gas 20  $\mu\text{L}$  were injected until the adsorption achieved saturation at 30°C. The outlet gas of CO were detected by a thermal conductivity detector (TCD), which were observed by the mass spectrometer. The amount of CO adsorption was calculated by the difference between the amount detected at the

outlet and the total amount of CO injected at the inlet. The catalyst particle size and metal dispersion was calculated using the cubic particle model [70].

### 3.3 Transesterification of soybean oil

Fatty acid of soybean oil obtained from Thai Vegetable Oil PLC were used as biodiesel feed for transesterification reaction. Soybean oil of 100 ml carried in a 500 mL three-necked round-bottomed flask connecting with the condenser for methanol condense (**Figure 3.3**). Soybean oil were heated to 60°C in the heating mantle. The potassium hydroxide (1% w/w of oil) were stirred in methanol with 9:1 methanol to oil molar ratio until completely dissolve the mixture. Then the mixture were added in three-necked round-bottomed flask while heating at 60°C with stirring at 500 rpm for 1 h and cool down. After the completion of the reaction, the mixture was placed in the separatory funnel until the phase separation between biodiesel and glycerol, where the lower glycerol phase was eliminated. The obtained product was washed with 60°C distilled water several times to remove the excess methanol, soap and potassium hydroxide until neutral. Finally, the water in product was entirely adsorbed by anhydrous magnesium sulphate ( $\text{MgSO}_4$ ) to derived soybean FAME.

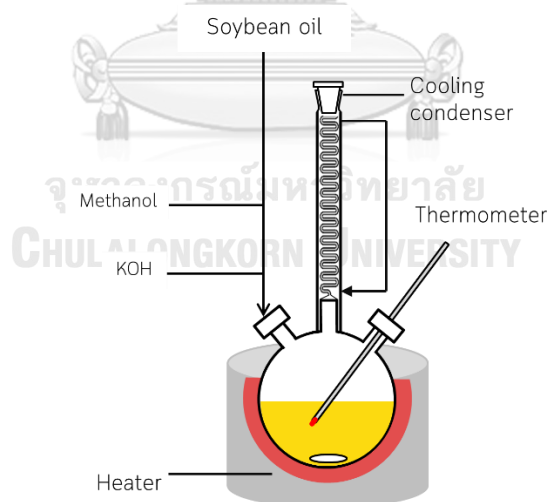


**Figure 3.2** Schematic diagram of transesterification in three-necked round-bottomed flask.

### 3.4 Experimental set up for partial hydrogenation

A custom-made continuous-flow trickle-bed reactor was constructed by using the stainless steel 316, with 7 mm I.D. and 300 mm length. A schematic diagram of



experimental apparatus was displayed in **Figure 3.3**. The reactor system comprised of feed unit, reaction test unit, and product separation unit. The heating system was controlled by K-type temperature controller in electrical tube furnace. While, the pressure of reactor was controlled by back-pressure regulator. The feed rate was controlled by using a HPLC pump and the gas flow rate was used to control mass flow of gasses for the reaction. Technically, the catalysts were packed in the middle of reactor tube in order to reach the uniform temperature distribution.

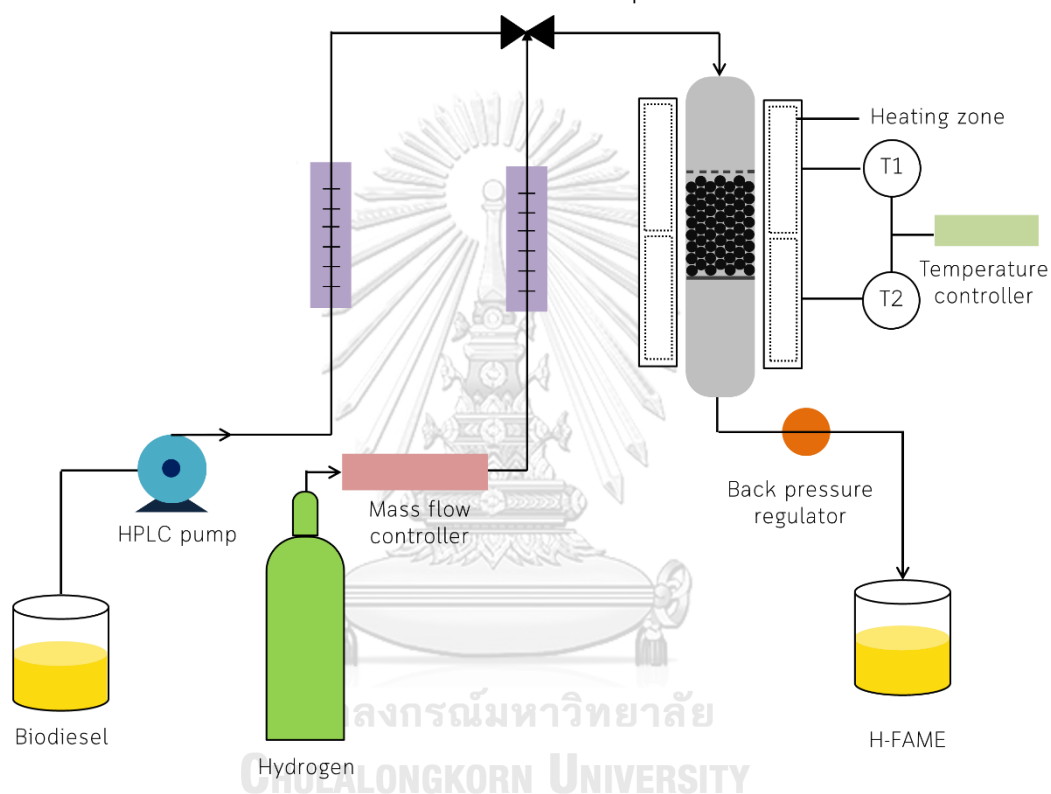


**Figure 3.3** Schematic diagram of continuous-flow trickle-bed reactor.

### 3.5 Test of catalyst in partial hydrogenation of soybean FAME

The catalysts 1 g were packed inside the reactor and reduced under influence of  $H_2$  for 3 h at desired temperature before use in the catalytic tests. The reactor was introduced the pressurized to 0.4 MPa  $H_2$  partial pressure. After that, the temperature was increased to 100 °C and was controlled by a temperature controller. Then, the soybean biodiesel was passed through the catalyst bed by a HPLC pump with a flow rate 40 g/h. The flow rate of  $H_2$  was controlled by a mass flow controller at 100 ml/min. The liquid product was collected every 1 h for analysis.

### Biodiesel analysis

Composition in the biodiesel before and after the partial hydrogenation reaction was collected and investigated the composition by using gas chromatograph GC-2010 installed with a flame ionization detector and capillary column (HP-88, 100 m x 0.25 mm x 0.2  $\mu$ m). Helium was employed as carrier gas with a flow rate of 53.8 mL/min. Samples of 1  $\mu$ l were injected into oven at 170°C. After 40 min, the injector temperature increased to 230°C with 4°C/min. The detector temperature was fixed at 250°C with a split ratio of 50 and maintained for 2.5 min with the total analysis time of 65 min. FAME composition was identified by reference to the retention time. The quantity of the FAME composition is defined and calculated from the ratio of the area under the maximum peak.

Oxidation stability of the product was analyzed by the measurement of the induction period (IP) by the 743 Rancimat. 7.5 g sample was stored in a flask and heated to 110°C while flowing to a stream of 10 L/h air. The air is passing through the sample and then fed into the collection vessel containing 60 ml of DI and a probe to measure conductivity. Oxidation stability was presented at the induction period (IP) described as the time differences between at the start of the test and the immediate increment in the conductivity of the solution in the collection flask. The IP value is generally represented in time and long IP times of biodiesel fuels indicate high stability to oxidation จุฬาลงกรณ์มหาวิทยาลัย

Cloud point (CP) is the temperature at the crystallite appearance with a cloudy appearance. It indicated the initial temperature appearance of wax crystals during the sample is cooled. The behavior of solid wax provided the oil and clogged fuel filters and injectors in engines.

Cold flow properties of biodiesel before and after partial hydrogenation including cloud point and pour point were investigated by using a Tanaka mini pour/cloud point tester Series MPC-102, which was developed according to ASTM D6749

## CHAPTER 4

### RESULTS AND DISCUSSION

#### 4.1 Synthesis of activation carbon

Cattail leave (CL) were used as a feedstock to produce activated carbon (AC) via hydrothermal and chemical activation. The effect of the chemical activation parameter (activating agent, temperature and concentration) is clarified in this section. Furthermore, the effect of hydrothermal process was briefly described. AC has been investigated for the physical and chemical properties (porosity, morphology, surface functional group, proximate and ultimate analysis), in which the optimum condition of chemical activation was chosen to synthesize the catalyst supporting material.

##### 4.1.1 Effect of hydrothermal process

**Table 4.1** shows the chemical composition of cattail leave (CL) and hydrochar (HC). The carbon content of HC increased from 39.95 to 45.45 wt% while oxygen and hydrogen content decreased from 53.85 to 48.32 wt% and 4.46 to 4.40 wt%, respectively. Thermogravimetric analyses of CL and HC are presented in **Figure 4.12**. In the first step, moisture content and light mass volatile of all sample evaporated during 30–150°C due to dehydration reaction. Hemicellulose has an amorphous structure, which can be decomposed easily at 200–280°C and oxygen compound is released such as CH<sub>4</sub>, H<sub>2</sub>O, CO, CO<sub>2</sub>, SO<sub>2</sub> and SO<sub>3</sub> [71, 72]. Loss of volatile matter (VM) increased the fixed carbon (FC) from 20.31 to 33.28. while the moisture slightly diminished at 110°C, which would be further investigated using a fourier transforms infrared (FTIR).

**Table 4.1** Ultimate and proximate analysis of cattail leave and hydrochar.

Sample	Ultimate analysis (wt%)				Proximate analysis (wt%)			
	C	H	N	O*	FC%	VM%	M%	A%
CL	39.95	4.46	1.74	53.85	20.31	75.90	1.58	2.21
HC	45.45	4.40	1.83	48.32	33.28	62.31	1.63	2.78

FTIR spectra of the CL and HC are shown in **Figure 4.1**. The functional group of lignocellulose were explained using the data in the **table 4.2**. The main compositions of CL were hemicellulose, cellulose and lignin about 8.7%, 63% and 9.6%, respectively. The symmetrical C-O stretching at 1290-950  $\text{cm}^{-1}$  greatly disappeared because the amorphous structure of hemicellulose significantly decomposed at 180-200°C. The O-H stretching is slightly reduced (3680-3000  $\text{cm}^{-1}$ ) because orderly arranged cellulose will begin to decompose at 230°C [62]. Moreover, the remaining C=C and C=O stretching (1600 and 1700  $\text{cm}^{-1}$ ) indicate the carbonyl and aromatic ring, in which lignin structure is hardly decomposed during a hydrothermal process.

**Table 4.2** Functional group of lignocellulose [73]

Wavenumber ( $\text{cm}^{-1}$ )	Functional group	Description
3680-3000	O-H stretching	Hydroxyl or carboxyl groups, alcohol from cellulose or phenols from lignin
2925	C-H stretching	Aliphatic
1700	C=O stretching	Carbonyl, ester or carboxyl from cellulose and lignin
1600	C=C stretching	Aromatic skeletal present in lignin
1290-950	C-O stretching	Ester from hemicellulose
860-724	C-H bending	Aromatic

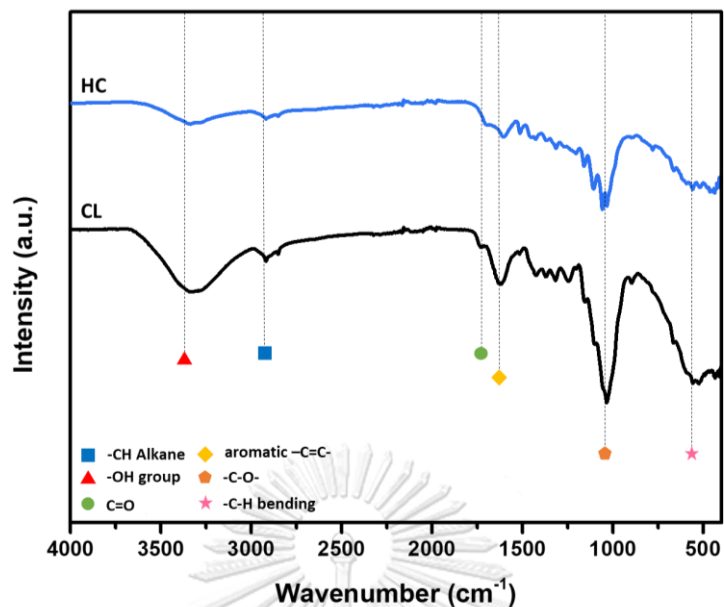


Figure 4.1 FTIR spectra of CL and HC

The surface morphology of the CL in **Figure 4.2 (a)** reveals that CL contains smooth fibers. After the hydrothermal process, **Figure 4.2 (b)** confirms that the cell wall of fiber has shrunk because the bond of hemicellulose has been broken via a hydrolysis reaction. At the same time, cellulose remained in the cell wall structure and sustained the fibers. Therefore, the hydrothermal process significantly impacted the destroy of hemicellulose component because it was an amorphous structure with low thermal stability.

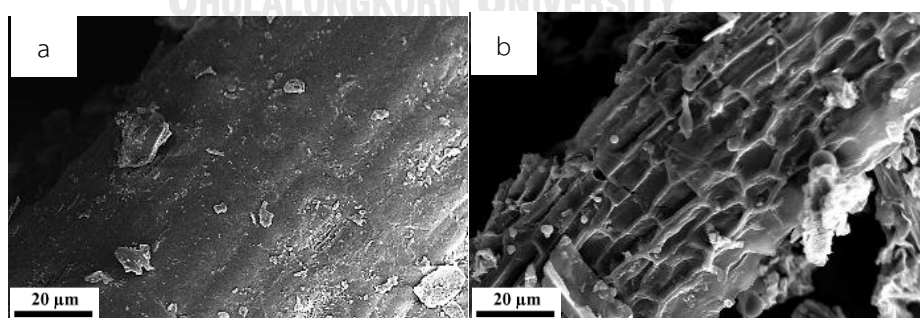


Figure 4.2 SEM images of (a) CL and (b) HC at 500x magnification.

#### 4.1.2 Effect of activating agent

The study of acid and alkaline activating agents was focused at 500°C and 900°C, respectively because the acid activating agent efficiently activated at 500°C. On the other hand, an alkaline activating agent efficiently activated at 900°C. **Table 4.3** shows BET surface area, pore size, micropore volume ( $V_{\text{micro}}$ ), mesopore volume ( $V_{\text{meso}}$ ) and total pore volume ( $V_{\text{total}}$ ) of activated carbon treated with a different activating agent (phosphoric acid (HP), sulfuric acid (HS), potassium hydroxide (KO) and sodium hydroxide (NO)). Acid activation generated almost all micropores (<2 nm), while alkali activation highly promoted mesopores (2-50 nm). According to the IUPAC classification in **Figure 4.2**, HP500-4 and HS500-4 sample were classified into type I, in which the characteristic of isotherm was like inverse L-shape. These results explain that amount of adsorption rapidly enhanced at a low relative pressure of approximately 0.03 corresponds to the formation of a monolayer. As a result, the gas molecules rapidly filled the large micropores, while a small amount of gas absorbed in narrow mesopore at relatively high pressure. Acid activating agent acted as oxidizing agent that reacted on surface of lignocellulose. The results indicated that HP500-4 has nearly doubled the BET surface area and total pore volume of HS500-4 because dehydration of sulfuric acid provided excess water vaporization and low gasification of biomass [74]. Therefore, phosphoric acid is more effective on surface reaction than sulfuric acid for promoting wider micropores micropore with a surface area 845.33 m<sup>2</sup>g<sup>-1</sup> and a pore size of 1.152 nm.

When comparing with alkaline activation, the shape of the adsorption isotherm were classified into type IV with a hysteresis loop, which indicated the mesopore volume. In this case, the adsorption of molecule gas on the mesopore wall were initially monolayer-multilayer. The hysteresis loop indicated that gas molecules were filled by the capillary condensation mechanism. The pore condensation was the phenomenon that gas condensed to a liquid-like phase within a pore at  $P$  lower than the  $P_0$  of the bulk liquid. This result was observed that the position of the curve of KO900-4 was higher than NO900-4 because KO900-4 has larger surface area and pore size than NO900-4, corresponding to **Table 4.3**. Different atomic sizes of Na and K significantly affect the expansion of the pores, in which the

atomic size of K (0.231 nm) was larger than Na (0.186 nm). This reason described the intercalation of the K atom with is larger in size. It was mobile and fill the gap in between the graphene layer. Thus, the expansion within pore by KOH was greater than NaOH activation. Whereas, the metallic Na slightly penetrated within the lignocellulosic structure [59]. The residual KOH, metallic K, salts, and impurity after the activation were eliminated by washing until neutral. Finally, the AC was separated and dried to obtain a high surface area carbon. KOH900-4 has the maximum  $S_{\text{BET}}$  of  $1323.5 \text{ m}^2\text{g}^{-1}$ , while NaOH activation created a  $S_{\text{BET}}$  of  $1219.61 \text{ m}^2\text{g}^{-1}$ . From the previous result, the alkaline activation was more advantageous than acid activation because it developed the mesoporous material with the connected pore. [75].

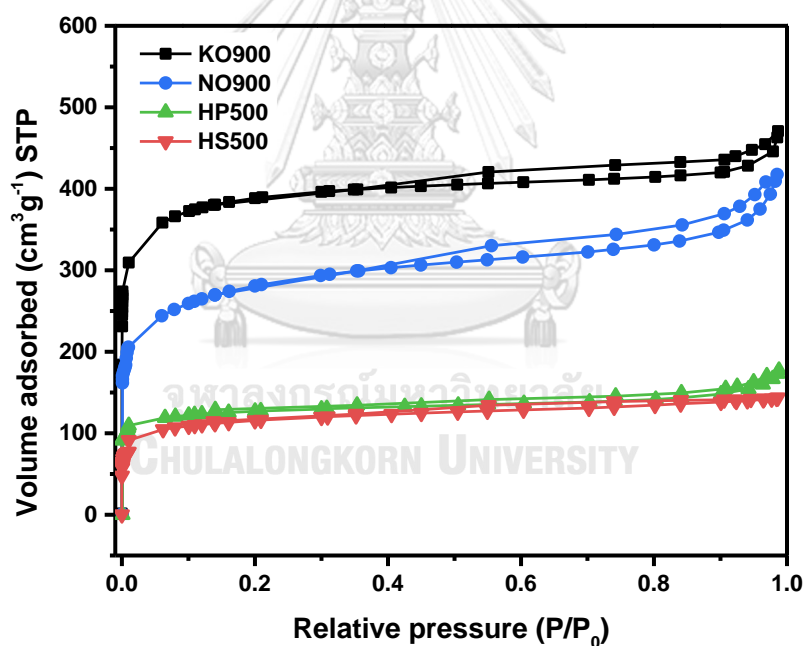


Figure 4.3 Adsorption isotherms of  $\text{N}_2$  on activated carbon at 77 K

**Table 4.3** Textural properties of activated carbon

Sample	BET SA (m <sup>2</sup> g <sup>-1</sup> )	Pore size diameter (nm)	V <sub>total</sub> (cm <sup>3</sup> g <sup>-1</sup> )	V <sub>micro</sub> (cm <sup>3</sup> g <sup>-1</sup> )	V <sub>meso</sub> (cm <sup>3</sup> g <sup>-1</sup> )	V <sub>micro</sub> (%)	V <sub>meso</sub> (%)
KO900-4	1323.58	2.780	0.783	0.062	0.721	7.92	92.08
NO900-4	1219.61	2.596	0.672	0.244	0.428	36.30	63.69
HS500-4	429.64	1.006	0.267	0.120	0.146	45.32	54.68
HP500-4	845.33	1.152	0.454	0.333	0.166	63.44	36.56

Figure 4.4 shows FTIR spectra of activated carbon with sulfuric acid, phosphoric acid, sodium hydroxide and potassium hydroxide. All sample show the disappearance of broadband between 1290-950 cm<sup>-1</sup> attributed to the C-O stretching, which indicated the decomposition of hemicellulose. The disintegration of peak located at 3680-3000 cm<sup>-1</sup> was ascribed O-H stretching, because cellulose completely decompose after activation process. HP500-4 sample shows the peaks at 1114 cm<sup>-1</sup> and 1220 cm<sup>-1</sup> are attributed to the P=O, O-C stretching vibration in P-O-C (aromatic) linkage, and P=OOH in phosphate ester. The peak at 1080 cm<sup>-1</sup> indicated the appearance of the P-O-P of polyphosphate, while phosphoric acid penetrated among the formation of phosphate esters on the cellulose side-chains and cross-links [76]. These results indicated that phosphoric acid functions both as an acid catalyst for bond cleavage and the formation of cross-links via cyclization and condensation reactions. Furthermore, cross-link biopolymer fragments connected with phosphate and polyphosphate bridge. Moreover, the disappearance of O-H stretching (3680-3000 cm<sup>-1</sup>) indicated that phosphoric acid promoted the decomposition of cellulose via dehydration reaction [57]. NO900-4 and KO900-5 appeared at a similar peak, in which are difficult to be describe the difference of the intensity. Both samples activated by the KOH and NaOH illustrated the peak at 1600 cm<sup>-1</sup>, which was attributed to C=C stretching vibration of an aromatic ring structure. The peak at 1700 cm<sup>-1</sup> was ascribed to the C=O stretching vibration indicated in the carbonyl, ester or carboxyl group. These peaks remained on the surface of sample after activation at 900°C, which slightly decomposed of functional group.



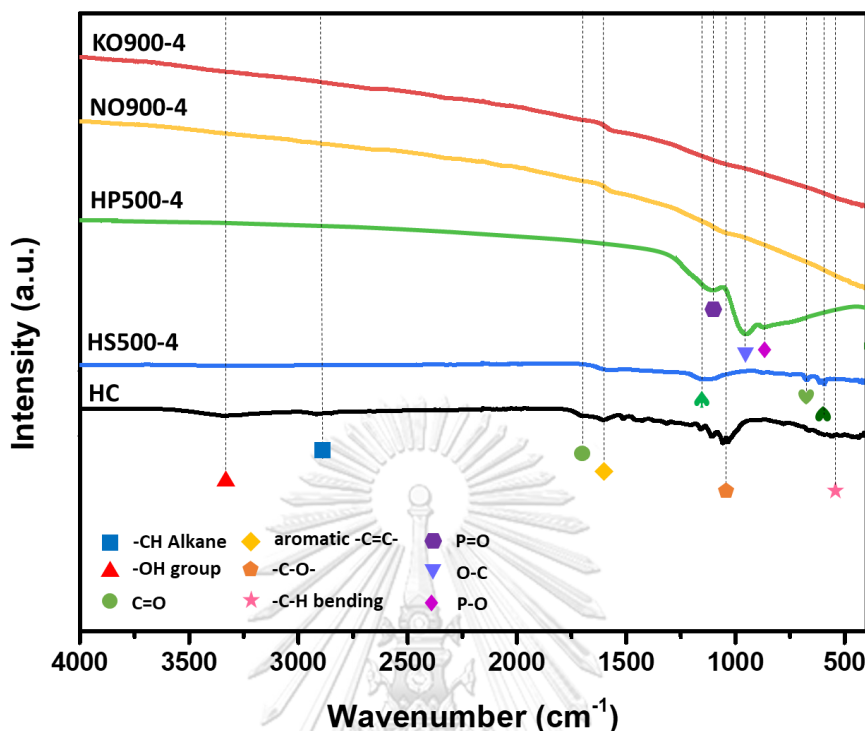
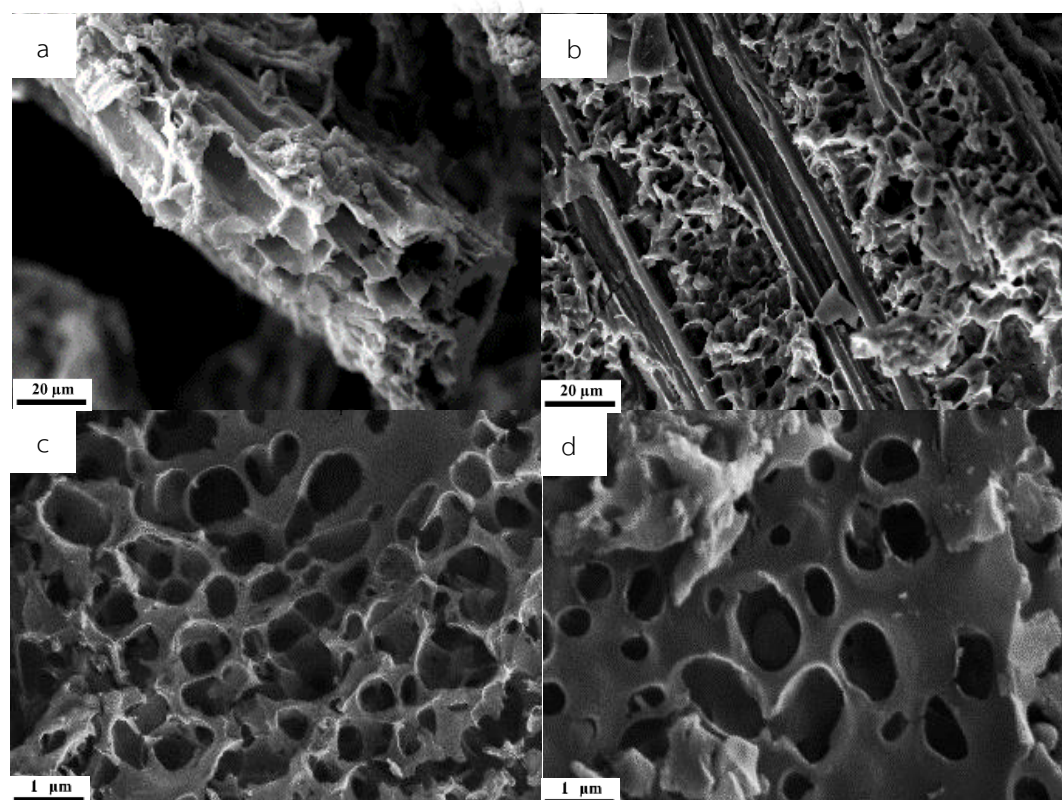


Figure 4.4 FTIR spectre of activated carbon

Figure 4.2 (b) reveals that HP500-4 structure shows some pores because hemicellulose and lignin transformed to volatile substance, while cellulose remained after chemical activation. These results implied that phosphoric acid inhibited the production of the levo-glucosan, which prevented the decomposition of cellulose into volatile products. Moreover, the formation of the pore irregularly distributed in each area of carbon, which may be caused by the presence of phosphate acting as a good flame retardant. While phosphate esters were generated during the reaction of phosphoric acid and inserted between the hydrogen bond of cellulose according to function group analysis with FTIR. Although, the pore of HP500-4 sample thoroughly dispersed on the surface while some close pores also occurred. KOH and NaOH activation generated the connected pore within the carbon matrix as shown in **Figure 4.2 (c) and (d)**. These results described that alkaline hydroxide activating agents did not decompose during the activation process while releasing the volatile such as CO, CO<sub>2</sub>, H<sub>2</sub>, and H<sub>2</sub>O. The obtained product led to the formation of the small pore via

dehydration and gasification reaction. Moreover, metal carbonate was reduced to metal atom, which can be intercalated within the carbon layer and generated the connect pore. It was clear that the pore distribution of KO900-4 was more uniform than NO900-4 on internal and external solid. Besides, the formation of pore also depends on the precursor with different structures and compositions. Consequently, KOH was specific for lignocellulose activation when compared to NaOH. From the previous results, we can conclude that KOH and  $H_3PO_4$  are good activating agents which achieved the highest mesopore and micropore, respectively.



**Figure 4.5.** SEM images of (a) HS500-4, (b) HP500-4 at 500x, (c) KO900-4 and (d) NO900-4

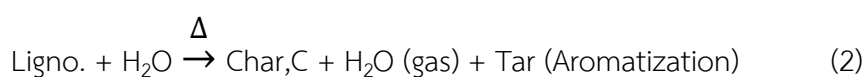
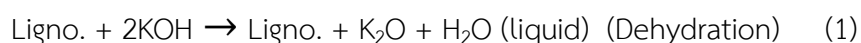
#### 4.1.3 Effect of temperature

The effect of activation temperature was reported in **table 4.4**. At the activation temperature of 500-900°C, it was observed that the surface area and micropore size up to 845.33 m<sup>2</sup>/g and 1.152 nm, followed by decreasing of surface

area and pore volume above 700°C. These results describe that the formation of phosphate ester cross-linked inserted between biopolymer fragment, which provided the expansion of micropore. With a further increase in temperature, phosphate linkages decomposed from the pore structure because of low thermal stability. After acid was removed, resulting in reduced porosity of HP700-4 and HP900-4 sample about 50% and 65%. Essentially, the mechanism of phosphoric acid activation described the following as: phosphoric acid significantly affects the decomposition of amorphous hemicellulose and lignin, while inhibited degradation of cellulose. Typically, the phosphorous compounds function as a fire retardant in a cellulose.

The reaction between phosphoric acid and cellulose began at 280 °C, the small polyaromatic units linked by phosphate and polyphosphate bridges. At 430°C, the acid catalyst broke the hydrogen bond of cellulose and formed cross-links via cyclization and condensation, which led to the formation of polyaromatic units. At 700°C, the micropore volume significantly decreased with no obvious influence on the mesopore volume. Above 700 °C, the micropore volume did not decrease any further. A reduction of mesopore volume is correlated to the shrinkage of the cell walls. This result occurs from the phosphate compound on the surface evaporated to volatile [77].

In contrast, the surface area and total pore volume were developed from KOH activation at high temperature because the activating agent did not decompose and depart from the surface of carbon. KOH effectively operated at 900°C for promoting the mesopore and the pore network in carbons. The activation mechanism of KOH occurred via the following reaction [78]:





The initial reaction can be released the main product, such as H<sub>2</sub>, H<sub>2</sub>O, CO, CO<sub>2</sub>, potassium oxide (K<sub>2</sub>O), and potassium carbonate (K<sub>2</sub>CO<sub>3</sub>) during activation below 800°C. In the first equation, the structure of lignocellulose was deformed while KOH was converted to K<sub>2</sub>O via dehydration, cracking and partial polymerization reaction at 400°C. Then, the char and steam were obtained from transformation of the lignocellulose through aromatization under pyrolysis reaction in eq. (2), which slightly generated the pore on the carbon surface. The steam in Equation (2) reacted with carbon in Equation (3), which released H<sub>2</sub> and CO from 600-700°C through the steam activation process. As a result, the pore size diameter of micropore expanded and transformed to mesopore from 1.403 to 2.494 nm, which increased the surface area and mesopore volume of KO700-4 sample to 995.32 and 79.6%, respectively. CO<sub>2</sub> and K<sub>2</sub>O were formed during the activation process, which were used as the reactant for K<sub>2</sub>CO<sub>3</sub> production in equation (5). Furthermore, carbon reacts with CO<sub>2</sub> to form CO at 800°C, which provides even more connected pores [79].



Above 700°C, potassium oxide (K<sub>2</sub>O) is reduced by carbon or hydrogen to form metallic potassium as in Equations (7) and (8). After that, the metallic potassium is mobile within the carbon matrix at 900°C, which can be intercalated between graphene layer. As a result, the pores in the carbon expanded and connected together [80, 81]. At 900°C, the mesopore volume almost enhanced 2 times while micropore volume notably decreased to become the mesopore. **Table 4.3** confirmed that the surface area and mesopore volume of KO900-4 were 1323.58 m<sup>2</sup>/g and 92.1%, respectively. Therefore, the high temperature was important to

develop the porosity via KOH activation. In contrast,  $H_3PO_4$  activation was suppressed when increasing the activation temperature.

**Table 4.4** Textural properties of activated carbon

Sample	$S_{BET}$ ( $m^2g^{-1}$ )	Pore size diameter (nm)	$V_{total}$ ( $cm^3g^{-1}$ )	$V_{mic.}$ ( $cm^3g^{-1}$ )	$V_{mes.}$ ( $cm^3g^{-1}$ )	$V_{mic.}$ (%)	$V_{mes.}$ (%)
KO500-4	323.97	1.403	0.211	0.096	0.115	45.5	54.5
KO700-4	995.32	2.494	0.499	0.102	0.397	20.4	79.6
KO900-4	1323.58	2.780	0.783	0.062	0.721	7.9	92.1
HP500-4	845.33	1.152	0.454	0.333	0.166	73.3	26.7
HP700-4	396.15	1.013	0.221	0.111	0.110	50.2	49.8
HP900-4	164.45	0.783	0.163	0.105	0.058	64.4	35.6

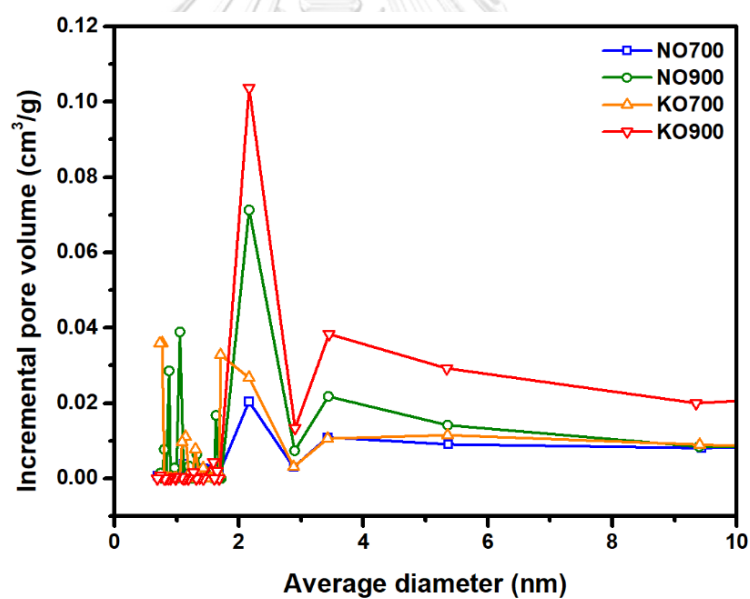


**Figure 4.6** The pore size distribution of activated carbon with base activation

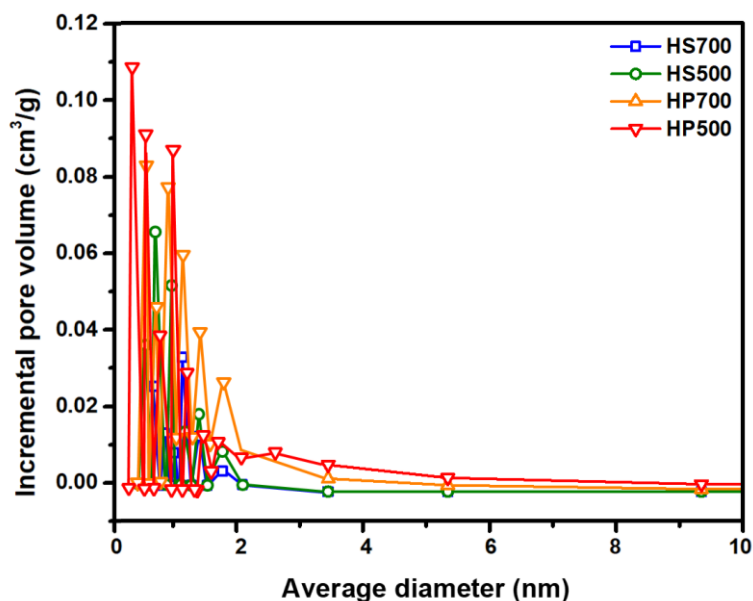


Figure 4.7 The pore size distribution of activated carbon with acidic activation

Figure 4.8 shows the functional group of activated carbon (HP500-4, HP700-4 and HP900-4) obtained from different activating temperature with phosphoric acid. During activation in the range 150-500°C, the peak of C-O stretching at 1290-950  $\text{cm}^{-1}$  disappeared because glycosidic bond of hemicellulose were hydrolyzed by acid catalyst. Meanwhile, aryl-ether bonds in lignin were cleaved according to reducing of O-H stretching at 3680-3000  $\text{cm}^{-1}$ . When these bonds were broken, the volatile  $\text{CO}_2$ , CO, and  $\text{CH}_4$  was released. The formation of phosphate groups and polyphosphate esters, including polyaromatics, was described earlier in Section 4.1.2. Above 500°C, the FTIR spectra revealed a decrease in the intensity of peak attributed to phosphate esters (1080  $\text{cm}^{-1}$ ). The decomposition of phosphate esters at high temperature result in the break of the aromatic cluster via cyclization and condensation reactions, which disappeared in the broadband of P=O, O-C stretching vibration in P-O-C (1114  $\text{cm}^{-1}$  and 1220  $\text{cm}^{-1}$ ). These results reduced the porosity of activated carbon because of the structure contraction.

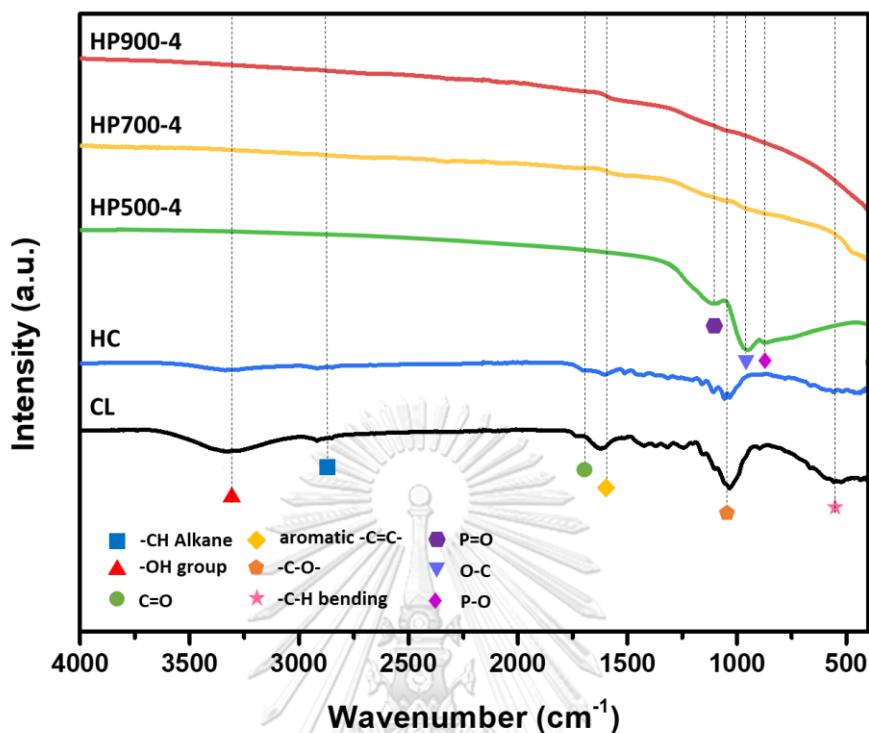
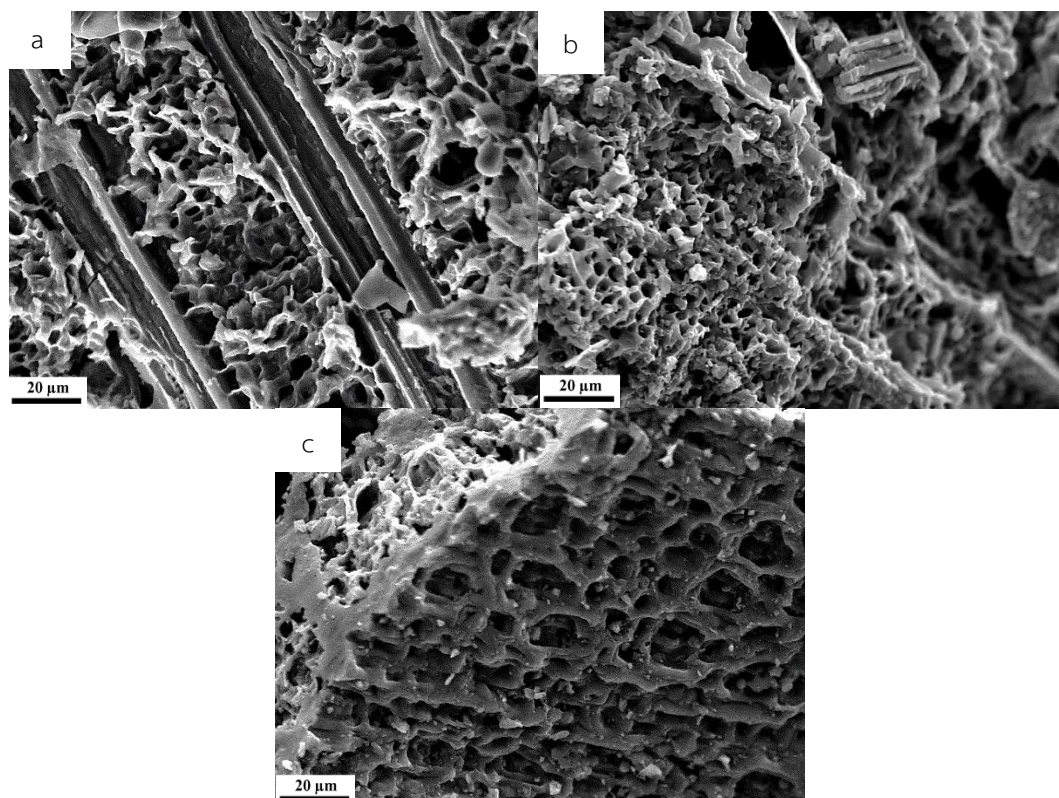


Figure 4.8 FTIR spectra of activated carbon with acidic activation

Figure 4.9 shows the morphology of activated carbon (HP500-4, HP700-4 and HP900-4) obtained from chemical activation with phosphoric acid at 500-900°C. From section 4.1.2 describe the morphology of activated carbon obtained from chemical activation with phosphoric acid at 500 previously. When increasing of activation temperature above 500°C, the pore wall began to contract because phosphate compounds were removed from the structure in Figure 4.9 (b). These results expected that effect of micropore volume decreased. Then, the pore wall collapsed and closed the side pore at 900°C, which provided the decreasing porosity shown in Figure 4.9 (c).



**Figure 4.9** SEM images of activated carbon of (a) HP500-4, (b) HP700-4, and (c) HP900-4

**Figure 4.10** shows the functional group of activated carbon (KO500-4, KO700-4, and KO900-4) obtained from 500-900°C with potassium hydroxide. After KOH activation at 500 °C remained a strong band at 1600 and 860-724  $\text{cm}^{-1}$ , which attributed the C=C stretching and C-H bending of aromatic in the lignin. These results described that cellulose structure was destroyed via dehydration, cracking, and partial polymerization reaction. The intensity of hydroxyl group (-OH) and aliphatic alkane (-CH) significantly reduced because the cellulose completely decomposed during physical activation above 700°C. Meanwhile, the C=C stretching required an activation temperature up to 800°C for destroying the lignin structure. Lignin was a complex structure with a decomposed temperature range of 300-800°C. Therefore, lignin completely destroyed when the activation temperature of 900°C.



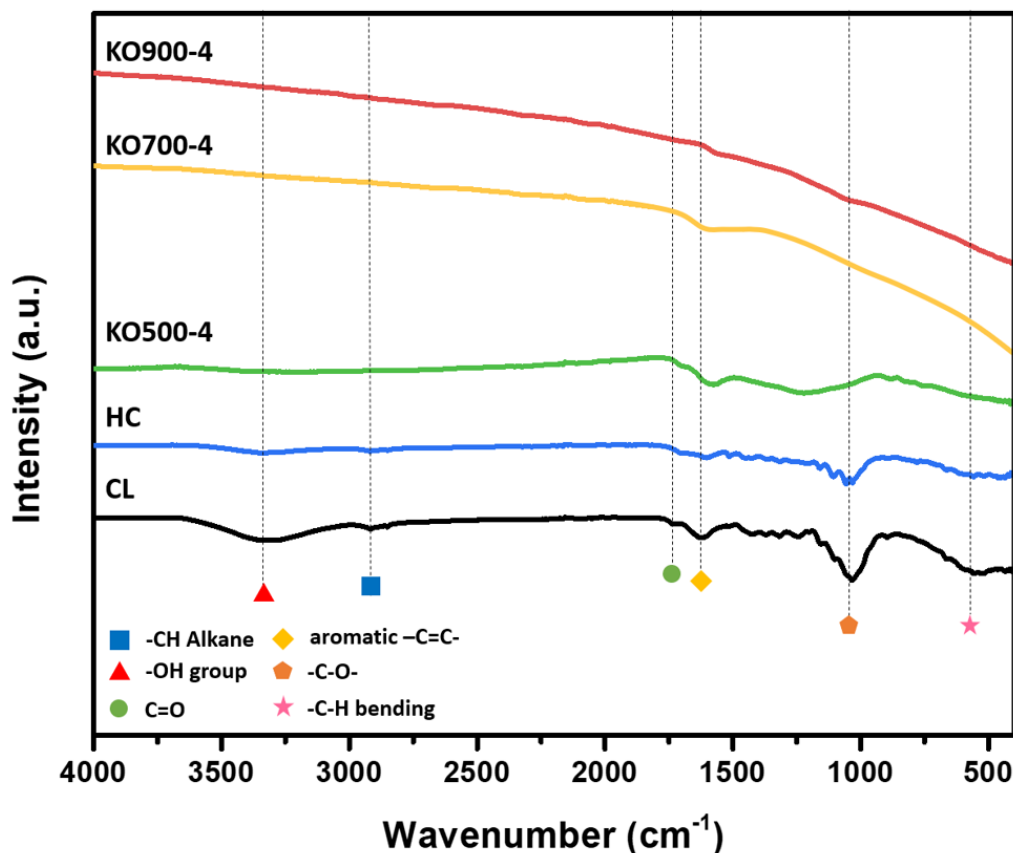
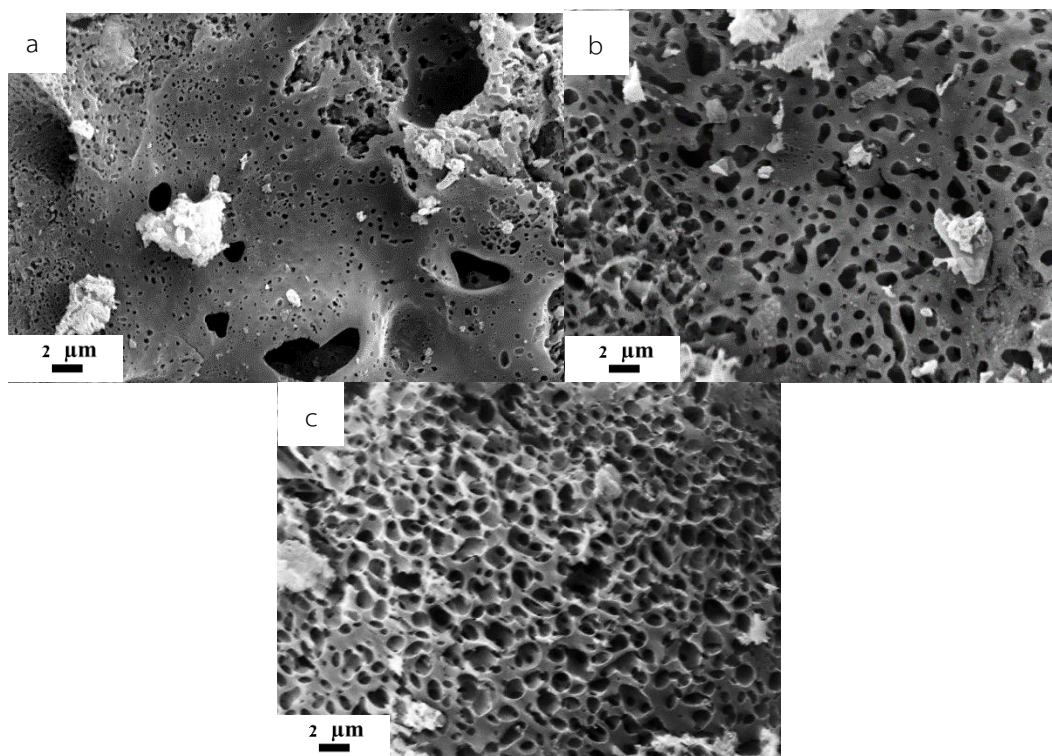


Figure 4.10 FTIR spectra of activated carbon with base activation

The morphology of activated carbon (KO500-4, KO700-4 and KO900-4) obtained from 500-900°C with potassium hydroxide. The SEM images of AC are shown in Figure 4.11 (a-c). When reaching the activation temperature 500°C, KO500-4 gradually began to generate small pores at the external surface because the volatile matter was released from char, which lead to the development of small pore on surface. After increasing the temperature to 700°C, a diffusion of CO<sub>2</sub> and steam into pores via physical activation occurred, which led to an extension of pores as shown in Figure 4.11 (b). It revealed the uniform pore distribution on the surface. An increase of pore size emerged by the aggregation of small pores. At 900°C, metallic K were intercalated within internal pores, which formed connected pore structure. KO900-4 exhibited that the pores were completely linked throughout the bulk material [27]. These results promoted the surface area and the diffusion of the molecule into the inner structure. Therefore, the activation temperature at 900°C has

significantly influenced to the formation of pore because the KOH activating agents performed the most efficiently.



**Figure 4.11** SEM images of activated carbon with basic activation.

**Figure 4.12** shows the thermogravimetric analysis of activated carbon obtained by KOH activation at 500-900°C. The weight loss between 30-150°C was mainly from the loss of moisture and light volatile. The high volatile degraded toward CO, CO<sub>2</sub>, and some hydrocarbon (CH<sub>4</sub>, C<sub>2</sub>H<sub>4</sub>, and C<sub>2</sub>H<sub>6</sub>) at 200-500°C. The weight loss of KO500-4 was greater than KO700-4 and KO900-4 because cellulose and lignin still remained mostly in the structure even after activation at 500°C. At 800°C, air was introduced instead of N<sub>2</sub> atmosphere, a rapid oxidation occurred resulting in a rapid weight loss of all the sample. The fixed carbon completely decomposed, becoming ash (MgO, CaO, K<sub>2</sub>O, and SO<sub>3</sub>) via oxidation reaction. These results show that KO900-4 contains the highest fixed carbon and the lowest volatile content. Consequently, the high activation temperature remarkably influenced the loss of volatile content and the rise of fixed carbon.

**Table 4.5** shows the element composition of activated carbon. During activation, the non-carbon content (H, O and N) were slightly eliminated in gases form by devolatilization. The loss of O content corresponded to the release of volatile matter. In contrast, the higher activation temperature enhanced the C content and fixed carbon in the aromatic structure. H content slightly decreased via dehydrogenation reaction, while O content significantly reduced via deoxygenation. At 900°C observed that O content reduced to 7.34 wt% while C content increased to 86.35 wt%

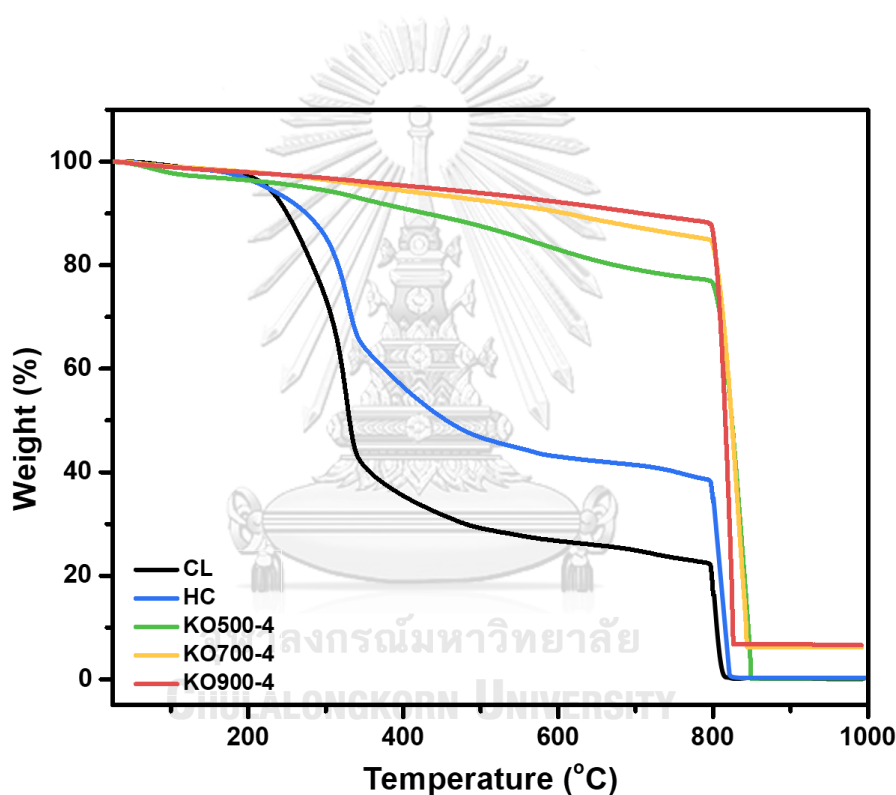


**Figure 4.12** Thermal Gravimetric Analysis of activated carbon.

#### 4.1.4 Effect of concentration

**Figure 4.13** shows the morphology of activated carbon prepared with potassium hydroxide at 900°C at different concentrations (2, 4 and 6 M). **Figure 4.13(a)** The KO900-2 appeared irregularly porous on the external structure because  $K^+$  ions were insufficient to penetrate the carbon sheet at low concentration. In contrast, KO900-6 revealed fractures in the pore structure because excess potassium

metal blocked in the pores, leading to collapse during activation. Accordingly, activation with 4 M KOH promoted the most porosity without the collapse of the pore wall.

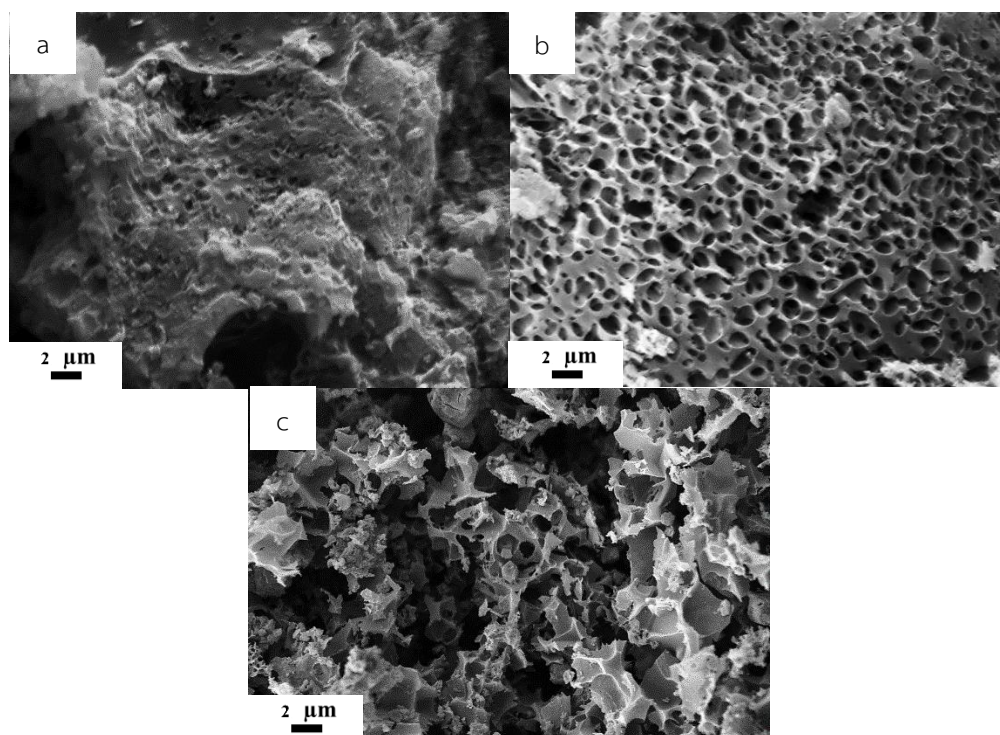


**Figure 4.13** SEM image of activated carbon prepared at various KOH concentration

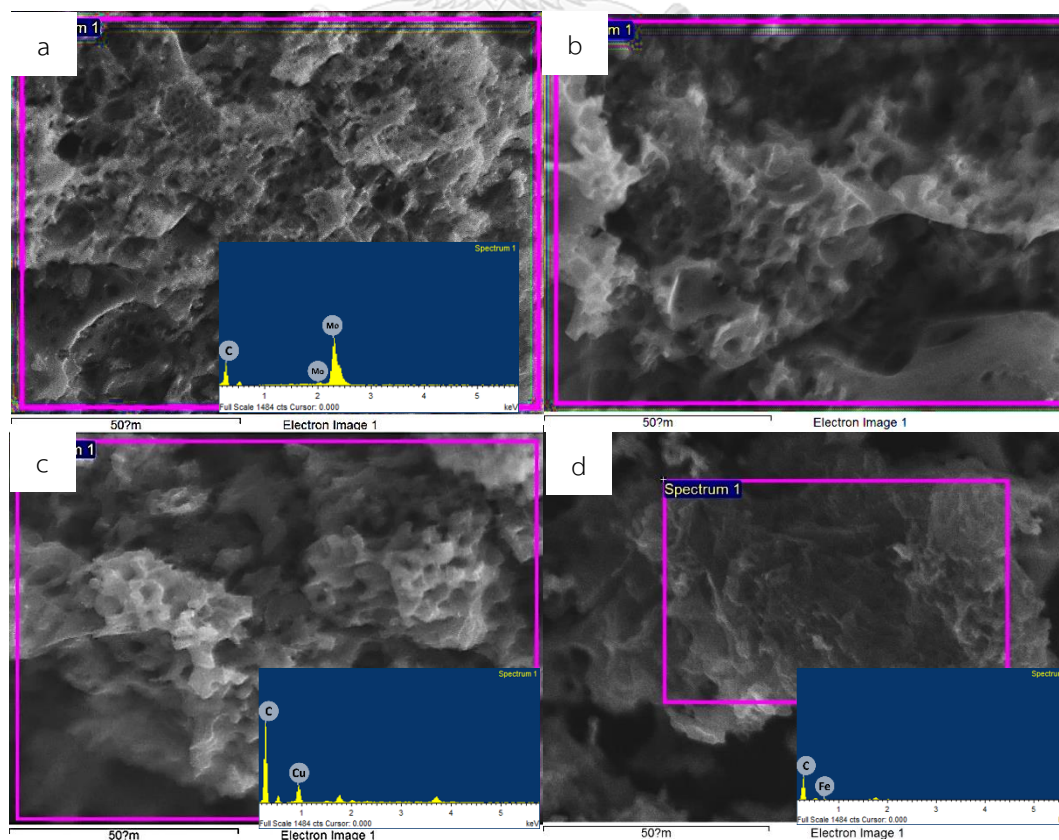
**Table 4.5** confirms that the excess concentration (KO900-6) reduced the fixed carbon because the alkaline metal residues became ash after combustion. The remained ash consist of MgO, CaO, K<sub>2</sub>O, and SO<sub>3</sub>, which blocked pores and reduced carbon yield. Although low concentrations (KO900-2) produced a small amount of ash, it has high volatile matter and low constant carbon content. Thus, KO900-4 indicates fixed carbon up to 81.18 wt% while volatile remained only 10.41 wt%. The above experiments concluded that the activated carbon prepared with 4 M of KOH at 900°C was suitable as a support due to its highest surface area and porosity.

**Table 4.5** Ultimate and proximate analysis of AC with basic activation.

Sample	Ultimate analysis (wt%)				Proximate analysis (wt%)			
	C	H	N	O*	FC%	VM%	M%	A%
KO500-4	58.86	4.69	1.69	34.76	72.89	19.97	1.01	6.13
KO700-4	69.19	4.18	1.31	25.32	78.64	13.67	1.43	6.26
KO900-4	86.35	4.67	1.64	7.34	81.18	10.41	1.59	6.82
KO900-2	77.61	4.26	1.49	16.64	79.84	13.98	1.29	4.89
KO900-6	81.63	4.22	1.28	12.87	78.98	7.64	1.85	11.53

#### 4.2 Preparation of metal catalyst impregnated on AC

The catalyst (Mo/C, Ni/C, Cu/C, Fe/C, MoNi/C, MoCu/C and MoFe/C) were prepared via rotary evaporation. The catalysts were analyzed using EDX H<sub>2</sub>-TPR, XRD, TEM, BET, and H<sub>2</sub> chemisorption, which could study the presence of metal on the support (e.g. reduction temperature, crystal structure, elemental composition and metal dispersion). Moreover, the properties of the catalyst could confirm the optimum conditions for partial hydrogenation reactions.



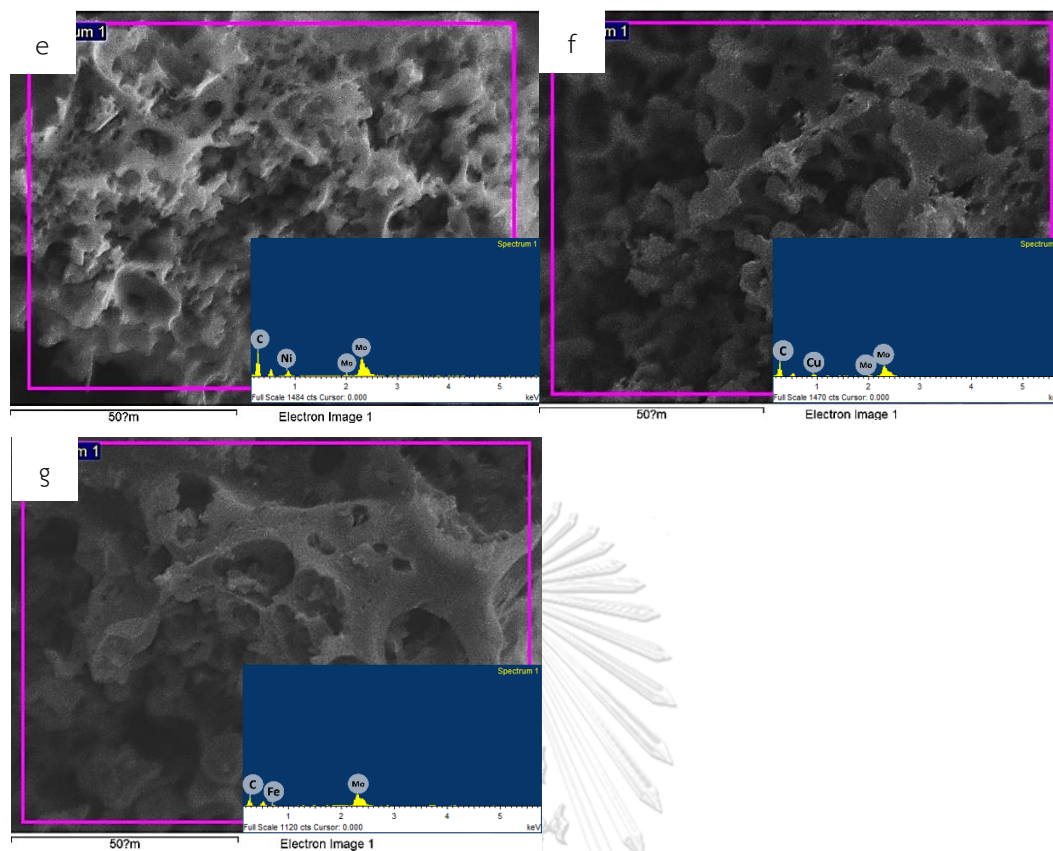
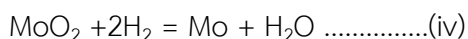
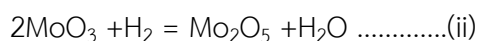


**Figure 4.14** SEM image of mono and bimetallic (a) Mo/C, (b) Ni/C, (c) Cu/C, (d) Fe, (e) MoNi/C, (f) MoCu/C and (g) MoFe catalyst

The surface morphology and elemental composition of catalyst were investigated using scanning electron microscope and energy dispersive spectroscopy. **Figure 4.14** shows the presence of catalysts on the support, which confirmed the elemental content from the EDS technique. The result confirm that the impregnation of metal particle was successful.

Reducibility of catalyst were analyzed using hydrogen temperature-programmed reduction technique. **Figure 4.15** reveals the TPR profiles of Ni/C, MoNi/C and Mo/C. The TPR profiles of Ni/C catalyst presented three reduction band in the temperature of 193°C, 344°C and 512 °C, which were indicated the reduction of metal oxide to metallic Ni. The bulk NiO was reduced at the temperature below 350°C while the strong interaction of NiO required the high temperature at 512°C for production of Ni<sup>0</sup>. The H<sub>2</sub> consumption of Mo/C catalyst around 448°C has been assigned to the reduction temperature of Mo oxide. The TPR profile of MoNi/C catalyst shown two

broad peaks, which overlapped at temperature of 470°C and 562°C. Initial step, the weak interaction of octahedral molybdenum ( $\text{Mo}^{6+}$ ) with support were easily reduced to tetrahedral molybdenum ( $\text{Mo}^{5+}$ ). Hence, the reduction of  $\text{MoO}_3$  to Mo metal were presented as follow:



Moreover, the  $\text{Ni}^{2+}$  were reduced to  $\text{Ni}^0$  at 570°C. The  $\text{Ni}^0$  species were more active than  $\text{Mo}^{4+}$  species because  $\text{Mo}^{4+}$  required a higher temperature (>800°C) for the formation of  $\text{Mo}^0$  species. The position of the Mo peak were shifted to the higher temperature (448°C to 470°C) because the interaction of  $\text{MoO}_3$  for MoNi/C catalyst was stronger than Mo/C catalyst [82]. Besides, the secondary peak of Ni shifted to a higher temperature (512°C to 586°C) because of the strong interaction of  $\text{Ni}^0$ [83]. These results confirm that the MoNi/C catalyst exhibited the higher interaction between metal and the support.

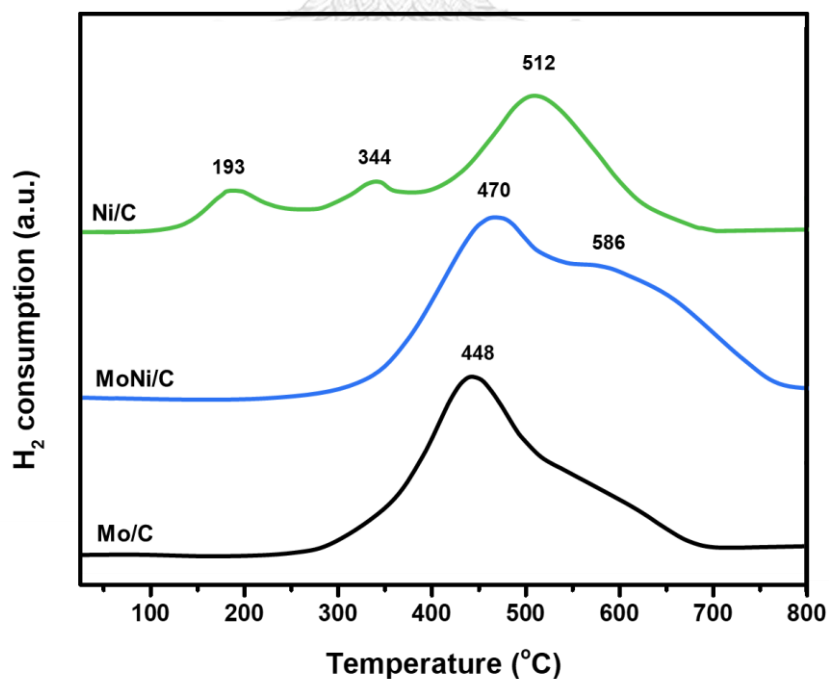


Figure 4.15 TPR-H<sub>2</sub> profiles of Ni/C, MoNi/C and Mo/C catalyst.

Figure 4.16 shows the TPR profiles of Cu/C, MoCu/C and Mo/C. The TPR profiles of Cu/C catalyst are located three different temperature at 201°C, 374°C, and 538°C. The first peak in the temperature range of 100–280°C can be attributed to the reduction of CuO species, which  $\text{Cu}^{+2}$  were reduced to  $\text{Cu}^{+1}$ . Above 400°C, the intermediate  $\text{Cu}^{+1}$  was completely reduced to the metallic  $\text{Cu}^0$  at the third peak. The reduction temperature of Cu was higher than Ni because of the agglomeration of the Cu particles on the support. The peak of Mo and Cu for MoCu/C catalyst overlapped in the temperature range of 400–600°C. The peak of  $\text{Cu}^0$  reduction were shifted to higher temperature an increase of interaction between the support. The accumulation of Cu particles decreased because of the presence of Mo metal.

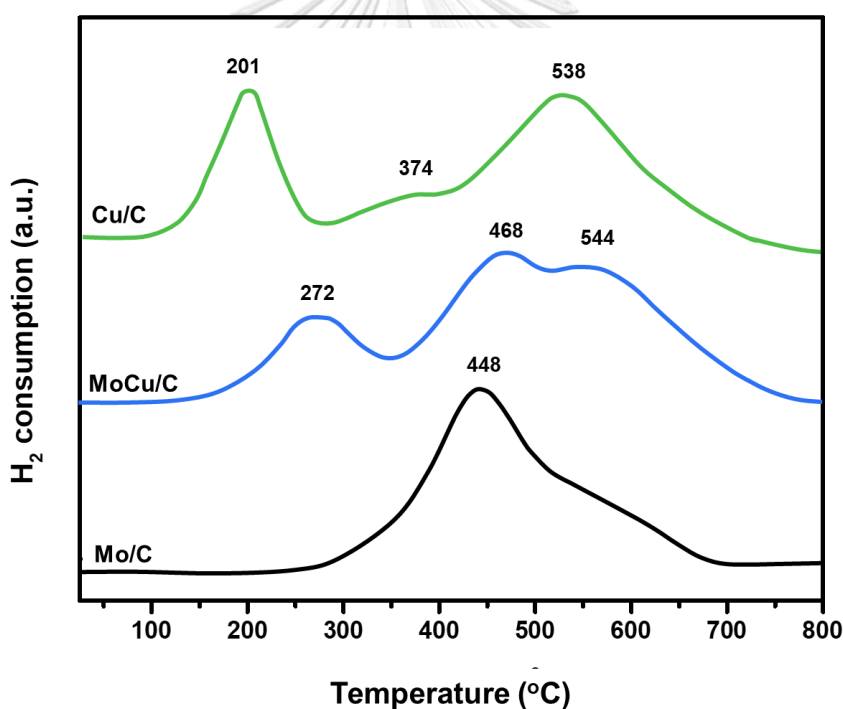


Figure 4.16 TPR- $\text{H}_2$  profiles of Cu/C, MoCu/C and Mo/C catalyst.

Figure 4.17 shows the TPR profiles of Fe/C, MoFe/C and Mo/C catalyst. The TPR profiles of Fe/C catalyst can be revealed two peaks at 554°C and 647°C. The first peak (554°C) was attributed to the reduction of  $\text{Fe}_3\text{O}_4$  to FeO while the last peak (647°C) was ascribed to the reduction of FeO to metallic Fe. The reduction temperature of Fe metal was higher than Ni and Cu metal because the large grain size of Fe. The peak of Mo and Fe in MoFe/C catalyst overlapped in the temperature



range of 450-700°C. The reduction temperature of the MoFe/C catalyst slightly increased compared to the Fe/C catalyst because the stronger interaction of Mo and Fe on the support.

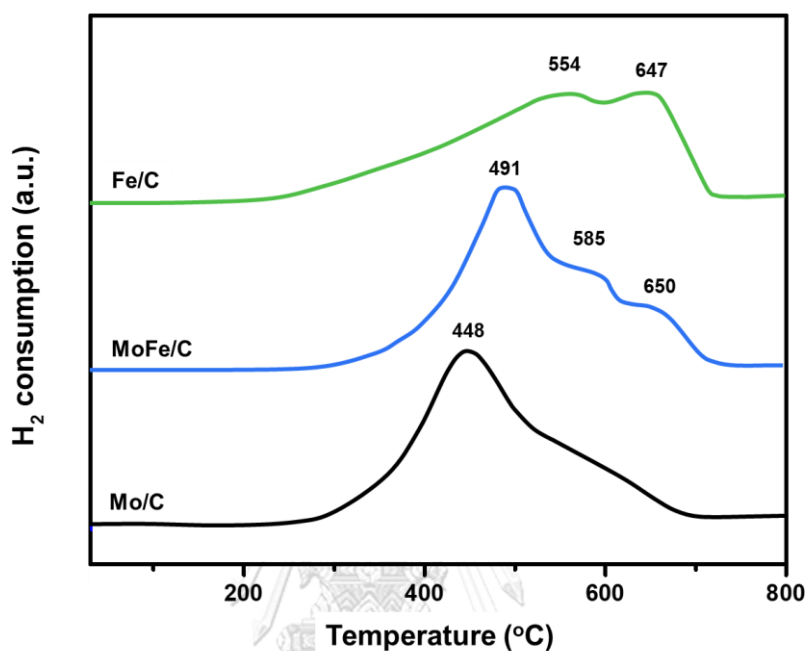


Figure 4.17 TPR-H<sub>2</sub> profiles of Fe/C, MoFe/C and Mo/C catalyst.

The formation of metal catalyst was identified in the  $2\theta$  range of 10-80° using X-ray diffraction. Figure 4.18 revealed the XRD pattern Mo/C, MoCu, Cu/C, MoNi/C, Ni/C, MoFe and Fe/C catalyst. No peak of carbon appeared in all samples because of the amorphous structure. The peak of Mo metal exhibited at 34.74°, 39.15°, 62.32°, 69.89° and 74.88°, which indicated the highest intensity of Mo (111). Moreover, the peak of MoO<sub>2</sub> can be observed at 41.65°, 38.86°, and 53.54° because MoO<sub>2</sub> required a reducing temperature above 1000°C. The peak of Ni metal at 44.78°, 52.36°, and 74.12° corresponded to (111), (220), and (200) while the peak of Cu at 43.05° and 51.29° were indicated (111), (200) plane. The XRD pattern of Fe metal exhibited at 35.28°, 41.07°, 42.11°, 44.24°, 45.02°, 48.39°, 53.39° and 76.21°, which the highest intensity of Fe at attributed (110) plane. The XRD pattern of the bimetallic catalyst

were indicated the no alloy phase. Furthermore, the reduction of crystallinity in bimetallic catalysts decreased the intensity peak.

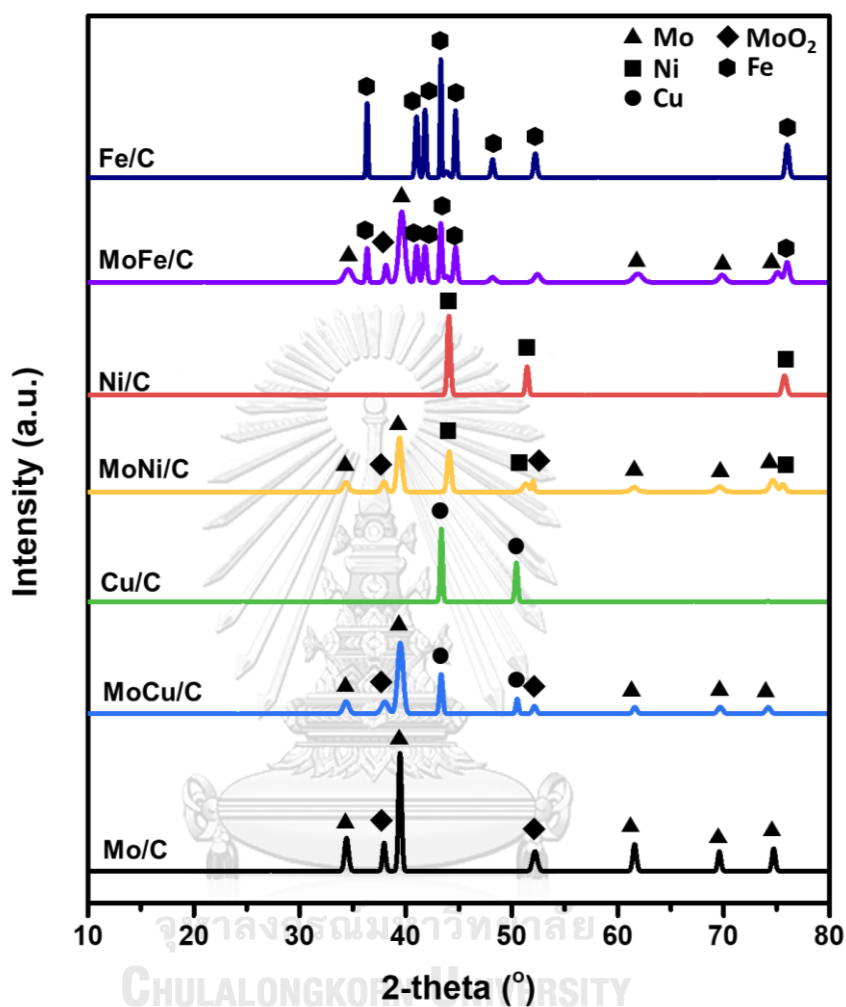


Figure 4.18 XRD patterns of Mo/C, MoCu, Cu/C, MoNi/C, Ni/C, MoFe and Fe/C catalyst.

The crystallite size evaluated by the Debye–Scherrer equation in Table 4.7. The crystallite size of the bimetallic catalyst (MoNi, MoCu, and MoFe) were smaller than the monometallic because the growth of the grain size were interrupted by Mo metallic. The Mo catalyst has the smallest crystallite size of 12.17 nm compared to Ni, Cu, and Fe because of the high dispersion of Mo on carbon support about 36.07% from the H<sub>2</sub> chemisorption technique. In contrast, the crystallite size of the Fe and Cu catalysts significantly increased to 39.89 and 41.02 nm, because the Fe and Cu

particles highly agglomerated on the support. Moreover, Cu and Fe metal with large particles blocked within the pore, which provided the low surface area and low metal dispersion. This could be explained that the increase of crystallite size was associated with the increase in the particle size.

**Table 4.6** Characteristics of catalysts

Catalyst	$S_{\text{BET}}^a$ ( $\text{m}^2\text{g}^{-1}$ )	$V_t^a$ ( $\text{cm}^3\text{g}^{-1}$ )	$D_{\text{av}}^a$ (nm)	Metal dispersion <sup>b</sup> (%)	Crystallite size of Mo <sup>c</sup> (nm)	Crystallite size of Ni <sup>c</sup> (nm)	Crystallite size of Cu <sup>c</sup> (nm)	Crystallite size of Fe <sup>c</sup> (nm)
Pd/C	403.32	0.51	2.31	48.45	-	-	-	-
Mo/C	343.80	0.37	1.72	39.92	12.17	-	-	-
Ni/C	307.63	0.42	1.89	36.07	-	15.62	-	-
Cu/C	92.64	0.14	0.87	10.56	-	-	41.02	-
Fe/C	53.10	0.11	0.74	6.43	-	-	-	39.89
MoNi/C	469.71	0.59	2.24	43.97	5.87	7.12	-	-
MoCu/C	154.28	0.27	1.12	18.88	8.62	-	25.43	-
MoFe/C	132.76	0.22	1.03	14.32	7.87	-	-	28.32
Carbon	1323.58	0.78	2.78	-	-	-	-	-

<sup>a</sup> Calculated by N<sub>2</sub> adsorption.

<sup>b</sup> Calculated by H<sub>2</sub> chemisorption.

<sup>c</sup> Calculated by X-ray diffraction.

**Table 4.6** exhibits these parameters for the investigation of catalysts after reduction of metal. The N<sub>2</sub> adsorption techniques indicate that the surface properties ( $S_{\text{BET}}$ ,  $V_t$ , and  $D_{\text{av}}$ ) of the catalyst reduced after impregnation because the metal dispersions (%) were inspected using H<sub>2</sub> chemisorption. The decrease of pore volume was related to metal dispersion (%) within the pore. The metal dispersion of monometallic were ordered in descending as follows—Mo, Ni, Cu, and Fe, respectively.

When considering a bimetallic catalyst, the surface area ( $S_{\text{BET}}$ ), pore volume ( $V_t$ ) and pore size ( $D_{\text{av}}$ ) of MoNi/C catalyst increased to 469.71  $\text{m}^2\text{g}^{-1}$ , 0.59  $\text{cm}^3\text{g}^{-1}$  and 2.24 nm, respectively. The metal dispersion increased to 43.97%. In contrast, MoCu/C

and MoFe/C catalysts with pore sizes smaller than 2 nm resulted in 18.44% and 14.32% of metal dispersion, respectively. Therefore, the metal dispersion of molybdenum-based catalysts were ordered as follows: MoNi > MoCu > MoFe, respectively. Moreover, the pore size and metal dispersion of MoNi/C catalyst was similar to Pd/C catalyst around 48.45%.

As described above, this study achieved the synthesis of the molybdenum-based catalysts on carbon support via rotary evaporation technique. The result showed the presence of metal particle with a crystallite structure. The metal dispersion, surface area and pore size of the Mo base catalyst increased in comparison with the monometallic catalyst. In contrast, the reduction of the crystallite size provided a decrease in particle size. The Mo base catalyst significantly affects on catalyst properties and performance of the catalyst. Thus, the activity of the catalyst can be investigated in partial hydrogenation.

### 4.3 Reaction study in partial hydrogenation process

The catalytic activity was estimated by partial hydrogenation reaction for improving the composition of fatty acid methyl ester and fuel properties (ie. oxidation stability, cloud point and, pour point). The as-prepared catalyst were tested the catalytic performance (ie. conversion of polyunsaturated FAME, selectivity of cis C18:1) compared to Pd/C. Moreover, the effect of reaction temperature was studied for the optimum catalyst.

#### 4.3.1 Effect of monometallic catalyst

The type of metal loading on carbon support affect the catalytic activity of partial hydrogenation. The monometallic catalyst (Mo/C, Ni/C, Cu/C, and Fe/C) were examined in partial hydrogenation of soybean FAME at a temperature of 100°C, H<sub>2</sub> pressure of 4 bar, WSHV = 40 h<sup>-1</sup> after 4 h of reaction time. **Figure 4.19** shows the effect of Mo/C Ni/C, Cu/C, and Fe/C on composition of FAME. **Table 4.7** shows that the monometallic catalyst with the conversion of C18:2 and C18:3 are ordered in descending order as follows: Mo/C > Ni/C > Cu/C > Fe/C. The results show that Mo catalysts exhibited higher conversion of polyunsaturated FAME, and selectivity toward trans-C18:1 than Ni, Cu, and Fe catalysts. The large pore size of the Mo/C

catalyst can be promoted the contact between the active site and reactants according to BET and H<sub>2</sub> chemisorption technique. Ni/C catalyst provided the cis C18:1 selectivity of 29.82 wt%, which favorite for the partial hydrogenation reaction. The monounsaturated FAME (C18:1) increased from 25.0 to 33.8 wt% with Mo/C catalyst, which improved oxidation stability from 2.37 h to 20.42 h. On the other hand, the cloud point and pour point increased from 2 to 14 and -1 to 11, respectively because of the increase of trans isomer. Although Cu/C catalyst inhibited the formation of trans-isomer, the product was saturated FAMEs (C18:0) than other catalysts. It can describe that the diffusion of the FAME molecules was limited because the agglomerated Cu particles blocked within the pore. Therefore, the pore size and distribution of active site affect on conversion of polyunsaturated FAME and cis-trans selectivity. The result suggests that the Mo/C catalyst enhanced the highest monounsaturated FAMEs, followed by an increase of 5.02% trans C18:1. **Figure 4.20** reveals that the monometallic catalyst with the selectivity of cis C18:1 are in descending order as follows: Ni > Mo > Cu > Fe. The formation saturated FAMEs and trans-monounsaturated FAME affect on the cold flow properties of biodiesel, which required the bimetallic catalyst for improving cis-monounsaturated FAME without decreasing the oxidation stability.

**Table 4.7** FAMEs composition and some fuel properties of soybean FAME and biodiesel product after reaction with monometallic catalyst

FAME composition (%)	Soybean FAME	Soybean H-FAME			
	Feed	Mo	Ni	Cu	Fe
C18:3 (wt%)	5.33	3.34	4.87	5.09	5.23
C18:2 (wt%)	52.15	43.81	48.04	50.34	52.09
C18:1 (wt%)	25.20	33.80	30.1	25.7	25.5
Trans (wt%)	0	5.02	0.26	0	0.22
Cis (wt%)	25.20	28.73	29.82	25.74	25.32
C18:0 (wt%)	4.07	5.24	4.2	6.48	4.1

ratio trans/cis-C18:1	0	0.18	0.01	0	0.01
Conv. of C18:2 (%)	-	18.32	8.35	3.97	0.70
Cloud point (°C)	2	18	9	5	3
Pour point (°C)	-1	14	7	2	0
Oxidation stability (h)	2.37	20.42	7.81	5.02	2.42

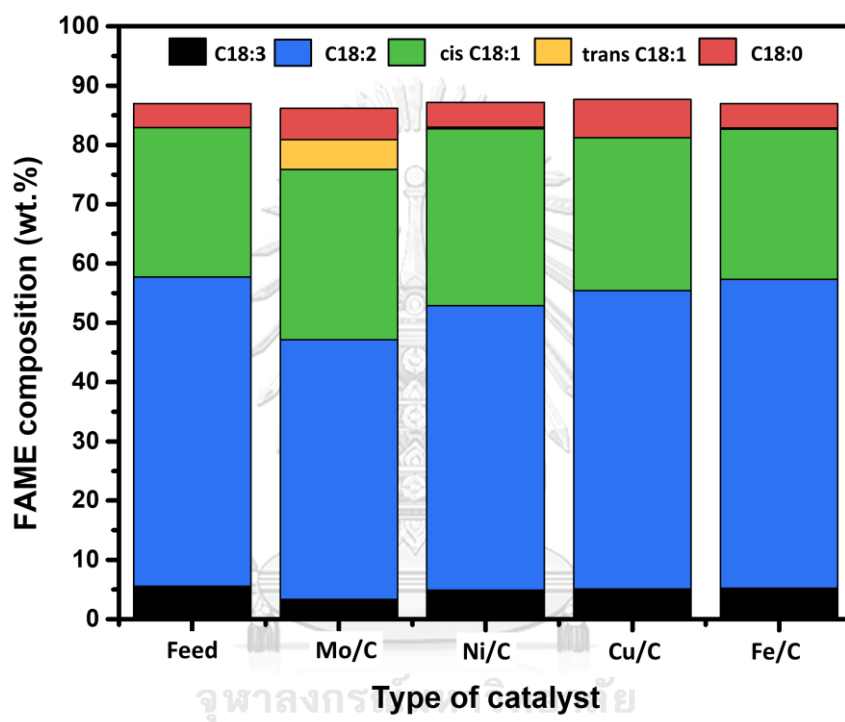
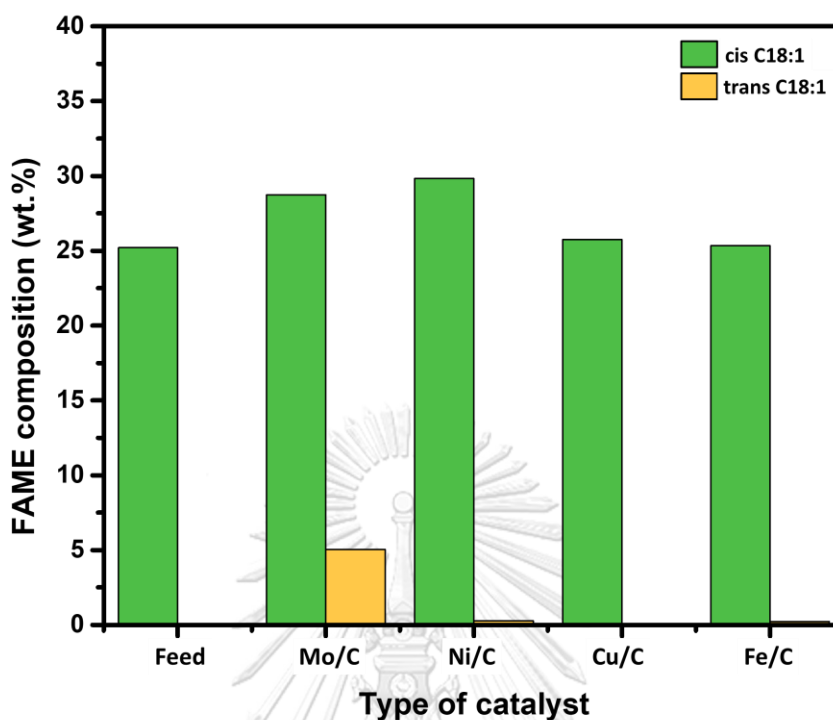


Figure 4.19 Effect of Monometallic catalyst on composition of C18



**Figure 4.20** Effect of monometallic catalyst on composition of cis and trans C18:1 FAMES

#### 4.3.2 Effect of bimetallic catalyst

Problems of monometallic catalysts involved low activity and selectivity of cis-isomer content in hydrogenated biodiesel. Above drawback of monometallic catalysts (ie. low activity and selectivity of cis-isomer content in hydrogenated biodiesel. In this part, the second metal were added to modify the formation of transC18:1 in Mo catalyst. The partial hydrogenation of biodiesel was operated at 100°C, 0.4 bar and 100 ml/min. **Figure 4.21** shows the effect of MoNi/C, MoCu/C, and Mofe/C catalyst on composition of FAME. hydrogen flow rate using bimetallic catalyst (MoNi/C, MoCu/C, and Mofe/C), which promoted Mo metal by the second metal. The Mo encourage the adsorbed initial state after the hydrogenation occurred on the Ni, Cu and Fe surface. **Table 4.8** shows the MoNi/C catalyst exhibited the optimum catalytic activity, which increased 19% of polyunsaturated FAME conversion. These results described that Ni decreased the formation of trans C18:1 because Ni active

site limited the catalytic activity of Mo. num because large particle size and low metal dispersion. Although the Pd/C catalyst exhibited the high activity under the mild condition, the conversion of C18:3 and C18:2 derived the product with selectivity towards C18:0 and trans-isomers. The high amount of C18:0 provided a negative impact on the poor cold flow properties. Therefore, the product were hydrogenated using the MoNi/C catalyst enhanced the oxidation stability while maintaining cold flow properties.

**Table 4.8** FAMEs composition and some fuel properties of soybean FAME and biodiesel product after reaction with bimetallic catalyst

FAME composition (%)	Soybean FAME	Soybean H-FAME			
	Feed	MoNi	MoCu	MoFe	Pd
C18:3 (wt%)	5.53	4.25	4.53	4.26	0.089
C18:2 (wt%)	52.20	42.51	47.18	48.51	0.036
C18:1 (wt%)	25.20	37	28.7	31.00	56.9
Trans (wt%)	0	1.94	1.93	0.94	20.13
Cis (wt%)	25.20	35.05	26.81	30.06	25.2
C18:0 (wt%)	4.07	4.14	6.39	4.15	29.4
ratio trans/cis-C18:1	0	0.06	0.07	0.03	1.05
Conv. of C18:2 (%)		19.00	10.43	8.59	99.22
Cloud point (°C)	2	13	8	5	26
Pour point (°C)	-1	10	6	3	21
Oxidation stability (h)	2.37	14.56	8.21	6.65	40.32



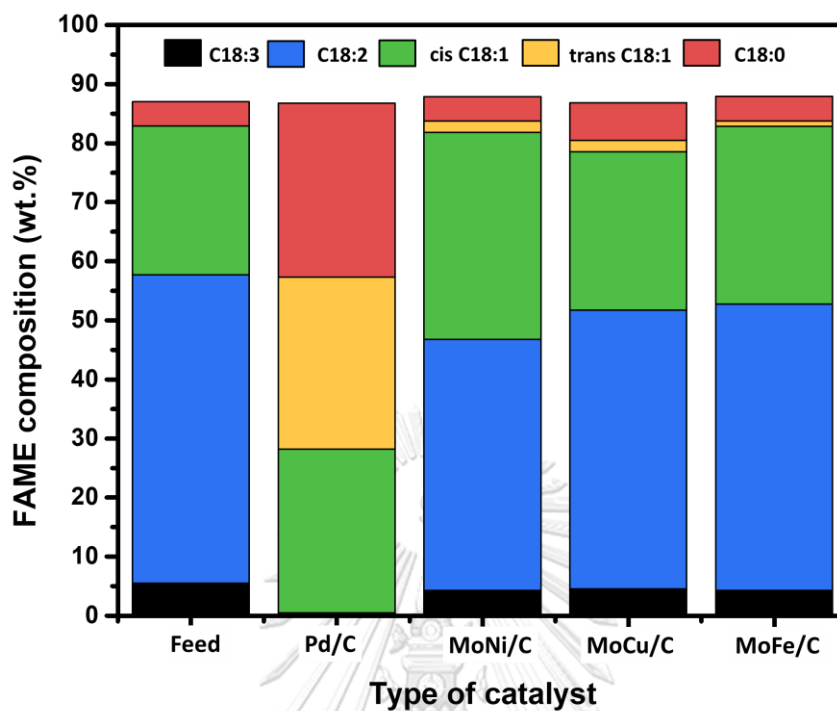


Figure 4.21 Effect of bimetallic catalyst on composition of C18

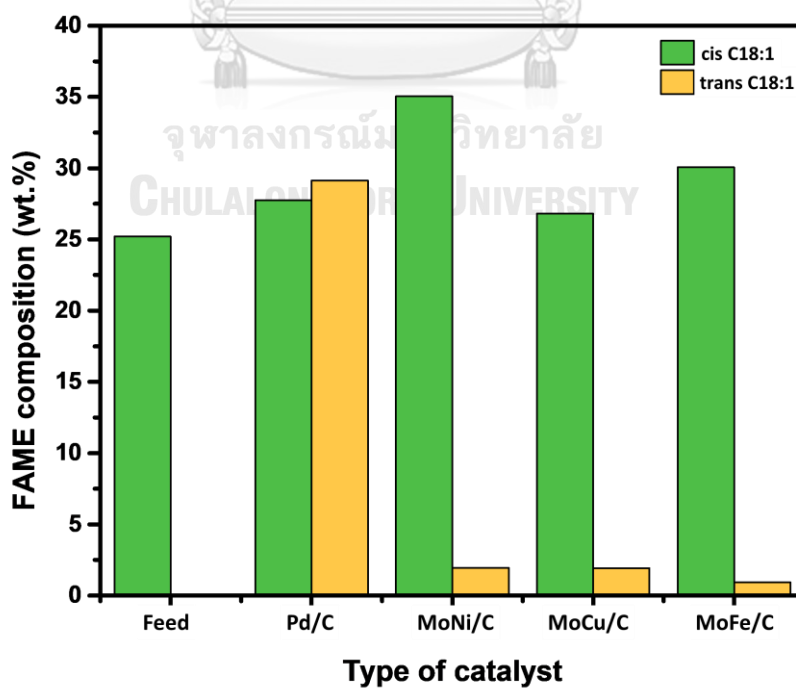


Figure 4.22 Effect of bimetallic catalyst on composition of cis and trans C18:1 FAMES

### 4.3.3 Effect of reaction temperature

The effect of temperature operated using MoNi/C catalyst at 0.4 bar, 100 ml/min, and 40 g/h. **Figure 4.23 and 4.24** show the effect of the reaction temperature on the catalytic activity and cis-C18:1 selectivity ratio and fuel property were varied from 80 to 140°C. **Table 4.9** indicated that the conversion of C18:2 and C18:3 at 80°C, 100°C, 120°C and 140°C were 6.78%, 17.29%, 35.68% and 54.78%, respectively. Although the increasing the reaction temperature improved the conversion of C18:2 and C18:3, the low temperature flow properties worsen. Above 120°C, The cis C18:1 rapidly converted to trans-C18:1 and C18:0, which provided the increase of cloud point and pour point with compromising oxidation stability. The high reaction temperature significantly influences on the isomerization of cis C18:1 because the faster reaction rate provided the high mobility and collisions of molecules according to kinetics principle. In contrast, the formation of trans C18:1 and C18:0 at 80°C and 100°C due to the low isomerization reaction. Therefore, the reaction temperature at 100°C was optimum for improving the fuel properties of soybean FAME, which oxidation stability was significantly from 2.37 h to 14.56 h. Moreover, The increasing of cis-unsaturated FAME increased the cloud point and pour point from 2 to 13°C and -1 to 10 °C

**Table 4.9** FAMEs composition and some fuel properties of soybean FAME and biodiesel product after reaction with MoNi/C catalyst

FAME composition (%)	Soybean FAME	Soybean H-FAME			
	Feed	80	100	120	140
C18:3 (wt.%)	5.33	4.59	4.25	3.33	1.69
C18:2 (wt.%)	52.15	49.23	42.51	36.62	24.31
C18:1 (wt.%)	25.2	27.11	36.99	31.19	40.74
trans	0	0.51	1.94	4.51	9.52
cis	25.2	26.6	35.05	26.68	31.22
C18:0	4.07	4.75	4.14	15.8	18.5
ratio trans/cis-C18:1	-	0.02	0.06	0.17	0.30

Conv. of C18:2	-	6.78	19.00	30.80	87.56
CP	2	4	13	15	25
PP	-1	1	10	11	20
Oxidation stability	2.37	4.12	14.56	19.4	30.64

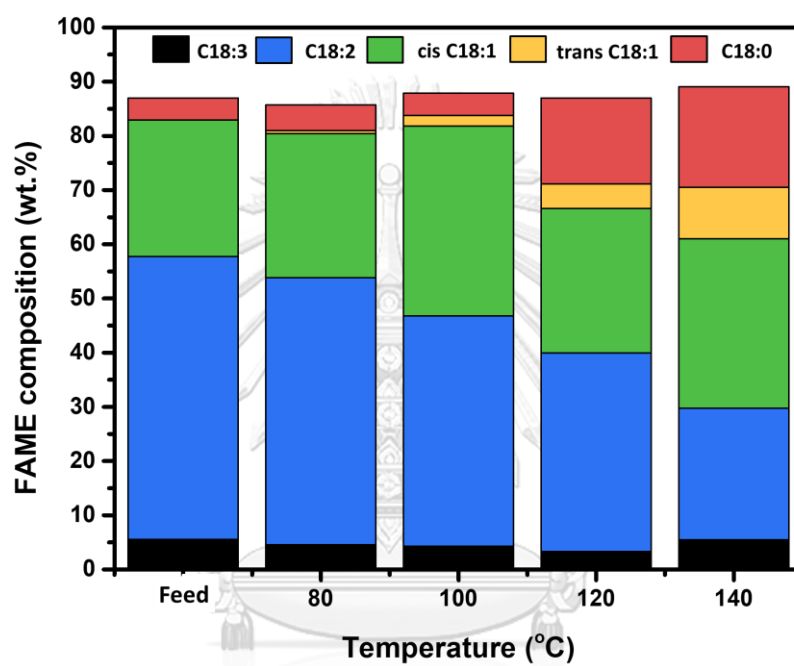


Figure 4.23 Effect of reaction temperature on composition of C18

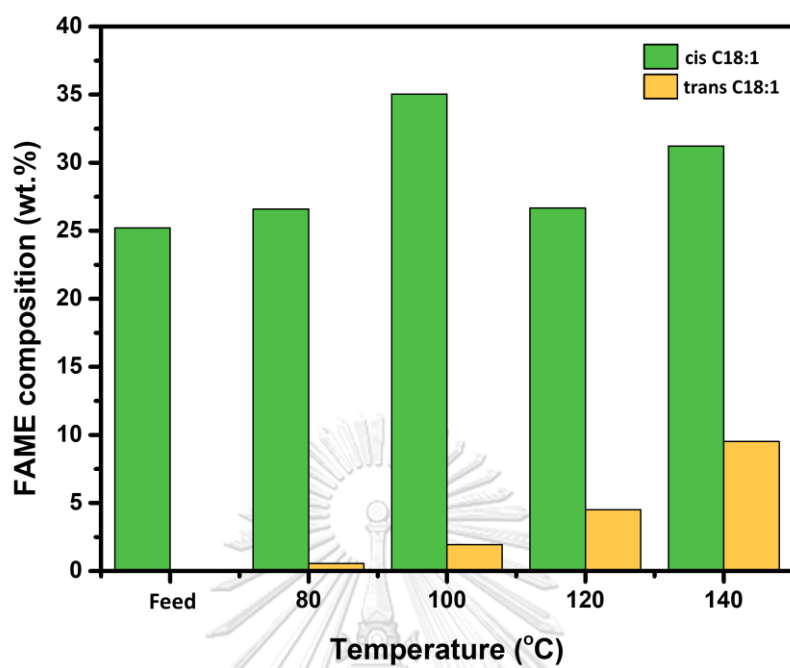


Figure 4.24 Effect of reaction temperature on composition of cis and trans C18:1 FAMES

## CHAPTER 5

### CONCLUSIONS

The experimental results have been described in chapter 4, which involved the synthesis of activated carbon, synthesis of catalyst, reaction study in the partial hydrogenation process. The experimental parameter and optimum condition were summarized in this chapter, including the additional suggestion associated with this research for future studies.

#### 5.1 Conclusions

##### 5.1.1 Synthesis of activated carbon

The synthesis of activated carbon from cattail leave (CL) via chemical activation with the different activating agents (KOH, NaOH, H<sub>3</sub>PO<sub>4</sub>, and H<sub>2</sub>SO<sub>4</sub>) was investigated for the production of carbon support. The report revealed that activation temperature is the main effect of activated carbon properties, rather than concentration of the activating agents. The activated carbon with surface area of 1323.58 m<sup>2</sup>/g obtained from KOH activation with the concentration of 4 M, and the activation temperature of 900°C. The prepared carbon indicated the high carbon content of 81.18% with low ash content. Moreover, the prepared carbon was classified as a mesopore with a pore size of around 2 nm. Therefore, the prepared carbon was used as catalyst support for the partial hydrogenation reaction.

##### 5.1.2 Synthesis of catalyst on activated carbon

The molybdenum base catalyst (MoNi, MoCu, and MoFe) were impregnated on activated carbon via rotary evaporation technique. The microscopic analysis revealed the uniform distribution of MoNi nanoparticle with 7.2 nm of particle size. The surface area and pore size decreased from around 1300 to 470 m<sup>2</sup>/g and 2.7 to 2.2 nm after impregnation with 5:5 wt% of MoNi/C catalyst. The XRD results exhibited the no alloy phase in MoNi/C catalyst with Mo crystallite size of 5.87 nm and Ni crystallite size of 7.12 nm. Furthermore, the MoNi/C catalyst was determined by 43.97% of metal dispersion by H<sub>2</sub> chemisorption, which increased the activity of partial hydrogenation.

### 5.1.3 Reaction study in the partial hydrogenation process

The result confirmed that the MoNi/C catalyst was favorable in partial hydrogenation for improving the oxidation stability and cold flow properties of soybean biodiesel. The MoNi/C catalyst significantly affect the catalytic activity and selectivity of cis C18:1 than other bimetallic catalysts. Besides, the reaction temperature of 100 °C increased polyunsaturated FAME, trans C18:1, and C18:0 to 18%, 1.94, and 4.14%, respectively. MoNi/C catalyst can improve oxidation stability, cloud point, and pour point from 3 to 14 hr, 2 to 13°C, and -1 to 10°C, the biodiesel was able to store for a long time according to US ASTM D6751 and EU EN14214 standards.

## 5.2 Recommendation

- 5.2.1 The production of carbon support from another biomass should be studied.
- 5.2.2 The effect of the pore size of the support on catalytic activity and selectivity of the product should be analyzed.
- 5.2.3 The synthesis of MoNi/C catalyst should be examined to demonstrate the reaction mechanism.
- 5.2.4 The influence of conditions (i.e. reaction time, H<sub>2</sub> pressure, gas flow rate and feed flow rate, etc.) in the partial hydrogenation reaction should be more studied.
- 5.2.5 The catalyst deactivation and long-term catalytic stability test should be further studied to prevent the deactivation of the catalyst.



## APPENDIX A

### RAW MATERIAL DATA

#### A.1 Specification data of soybean oil

Certificated No.: HACCP, ISO 9001, ISO 14001, GMP, FDA,

Customer/Supplier: Thai Vegetable Oil Public Company Limited

Manufacturing process: ICE Condensation Vacuum System (ICS)

Properties : Pure and Natural goodness

Rich in Vitamin E

GMO Free

Cholesterol Free

No Artificial Additives or Preservatives

Trans Fat Free

**Table A.1** Specification of soybean oil

Test item	Result
Free Fatty Acid %	0.05-0.1%
Peroxide Value meq/kg	0.5-1.0 meq/kg
Refractive Index @ 40°C	1.46-1.47
Iodine Value ( $W_{ijs}$ )	123-139
Moisture %	0.05-0.1%
Cold Test	5.5 hrs
OSI @ 110°C	5.5-6.0 hrs
Saponification Value	191-192
Specific Gravity @ 25°C	0.915-0.925
Smoke Point	460-465°F
Flash Point	650-655°F
Fire Point	690-695°F



## A.2 Chemical property of soybean oil

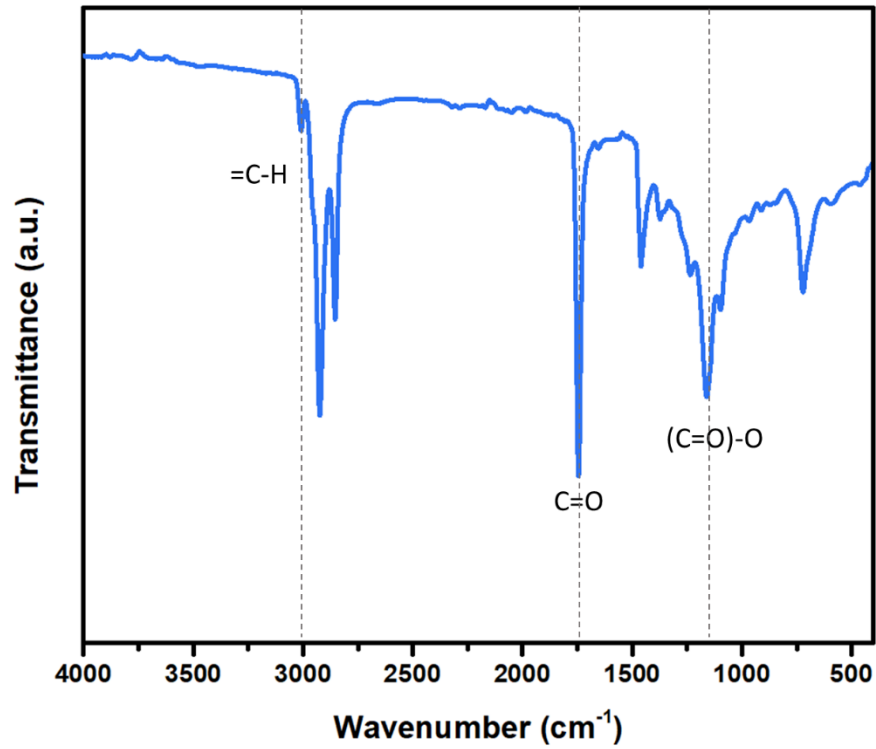


Figure A.1 FTIR spectra of soybean oil

## A.2 Chemical property of soybean biodiesel

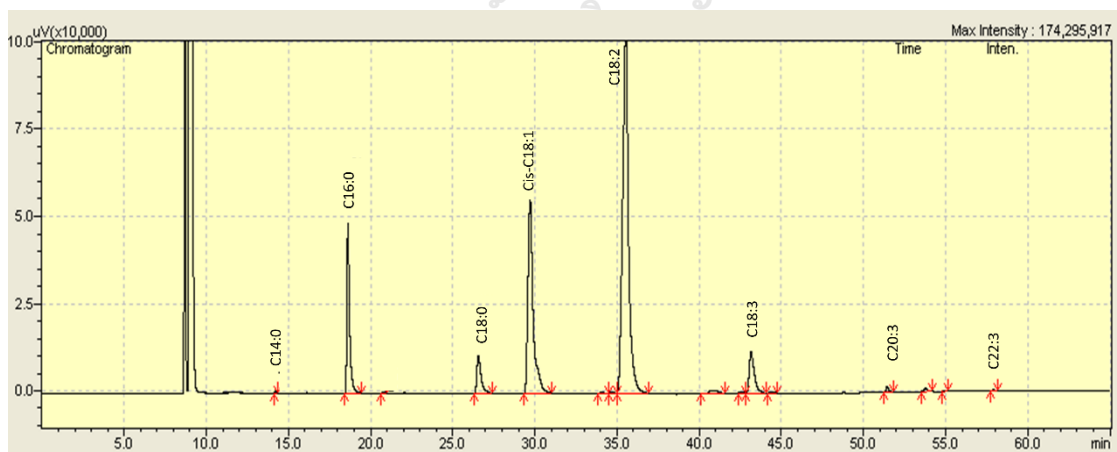


Figure A.2 GC chromatogram of soybean FAME

**Table A.2** Specification of the EAS-ERIA BDF standard

Specifications	Unit	EAS-ERIA
		EEBS:2008
Ester content	mass%	96.5 min.
Density	kg m <sup>-3</sup>	860-900
Viscosity	mm <sup>2</sup> s <sup>-1</sup>	2.00-5.00
Sulfur content	mass%	0.001 max.
Flashpoint	°C	100
Carbon residue (100%)	mass%	0.05 max.
Cetane number		51.0 min.
Sulfated ash	mass%	0.02 max.
Total contamination	mg kg <sup>-1</sup>	24 max.
Copper corrosion		Class-1
Oxidation stability	hrs.	10.0
Iodine value		N.D.
Methyl linolenate	mass%	12.0 max.
Polyunsaturated FAME (with 4+ double bonds)	mass%	N.D.
Monoglyceride content	mass%	0.80 max.
Diglyceride content	mass%	0.20 max.
Triglyceride content	mass%	0.20 max.
Total glycerol content	mass%	0.25 max.
Phosphorus content	mg kg <sup>-1</sup>	10.0 max.
Cloud point	°C	16
Pour point	°C	13

## APPENDIX B

## TEMPERATURE PROFILE

## B.1 Temperature profile of stainless steel horizontal tube reactor

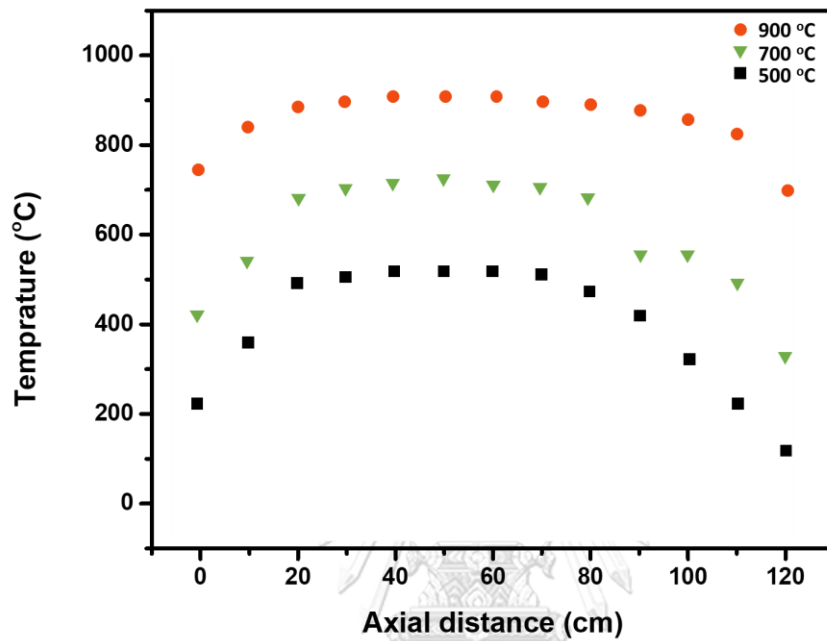


Figure B.1 Temperature profile of stainless steel horizontal tube reactor

Energy used: 4,000 kW/h

APPENDIX C  
BASIC CALCULATION

C.1 Weight hourly space velocity (WHSV)

$$\text{WSHV (h}^{-1}\text{)} = \frac{\text{mass feed flow per hour}}{\text{mass of the catalyst}}$$

In this study :  $\text{WSHV} = 40 \text{ h}^{-1}$

$$\text{WSHV (h}^{-1}\text{)} = \frac{0.667 \text{ g} \cdot \text{min}^{-1}}{1 \text{ g}} \times 60 \text{ min}$$

$$\therefore \text{WSHV (h}^{-1}\text{)} = 40.02 \text{ h}^{-1}$$

C.2 C18:2 conversion

Conversion of C18: 2 and C18: 3

$$= \frac{(\text{C18: 3} + \text{C18: 2})_{\text{before}} - (\text{C18: 3} + \text{C18: 2})_{\text{after}}}{(\text{C18: 3} + \text{C18: 2})_{\text{before}}}$$

C.3 Trans C18:1 to cis C18:1 ratio

$$\text{trans C18: 1/cisC18: 1} = \frac{\text{trans C18: 1}}{\text{cis C18: 1}}$$

## APPENDIX D

## CALCULATION FOR METAL ACTIVE SITES AND DISPERSION

Calculation of metal active sites and metal dispersion on the catalyst can be evaluated by H<sub>2</sub>-chemisorption is as follows equations:

D.1 Calculation of volume of H<sub>2</sub> adsorption on catalyst

$$V_{\text{ads}} = \frac{V_{\text{inj}}}{m} \times \sum_{i=1}^n \left(1 - \frac{A_i}{A_f}\right)$$

Where  $V_{\text{inj}}$  is volume injected, 0.02 cm<sup>3</sup>

$m$  is mass of catalyst used, g

$A_i$  is area of peak  $i$

$A_f$  is area of last peak

## D.2 Calculation of metal active sites

$$\text{Metal active site} = S_f \times \frac{V_{\text{ads}}}{V_g} \times N_A$$

Where  $S_f$  is stoichiometry factor, H<sub>2</sub> adsorbed on metal, H:metal = 2:1

$V_{\text{ads}}$  is volume adsorbed

$V_g$  is molar volume of gas at STP, 22414 cm<sup>3</sup>/mole

$N_A$  is Avogadro's number, 6.023x10<sup>23</sup> molecules/mole

## D.3 Calculation of metal dispersion

$$\text{Metal dispersion (\%)} = 100 \times \frac{\text{weight of metal form H}_2 \text{ adsorbed}}{\text{weight of metal loaded}}$$

$$\%D = 100 \times S_f \times \frac{V_{\text{ads}}}{V_g} \times \frac{MW}{\%M} \times 100 \times 100$$

Where  $S_f$  is stoichiometry factor, H<sub>2</sub> adsorbed on metal, H:metal = 2:1

$V_{\text{ads}}$  is volume adsorbed

$V_g$  is molar volume of gas at STP, 22414 cm<sup>3</sup>/mole

MW is molecular weight of the metal

%M is weight percent of the active metal

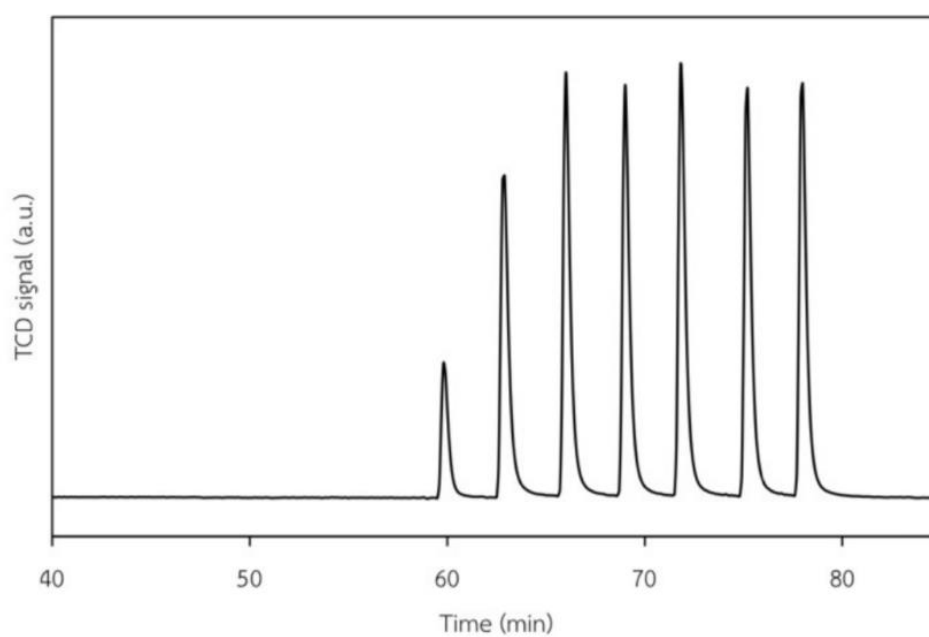
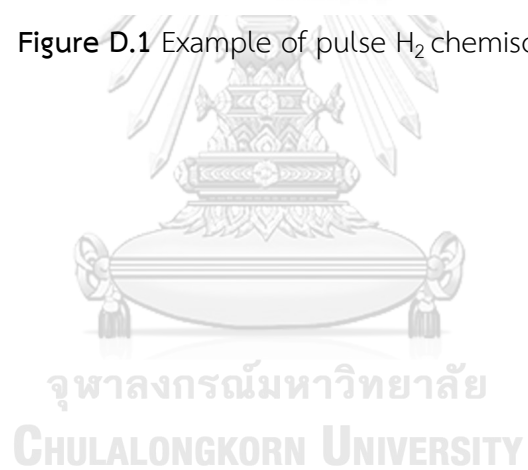


Figure D.1 Example of pulse H<sub>2</sub> chemisorption



## APPENDIX F

## CALCULATION FOR AVERAGE CRYSTALLITE SIZE

## F.1 Calculation of average crystallite size

$$D(2\theta) = \frac{K\lambda}{\beta \cos\theta}$$

Where K is Scherrer constant

$\lambda$  is the wavelength of the X-rays

D is average crystallite size

$\beta$  is peak width, FWHM

$\theta$  is the scattering angle

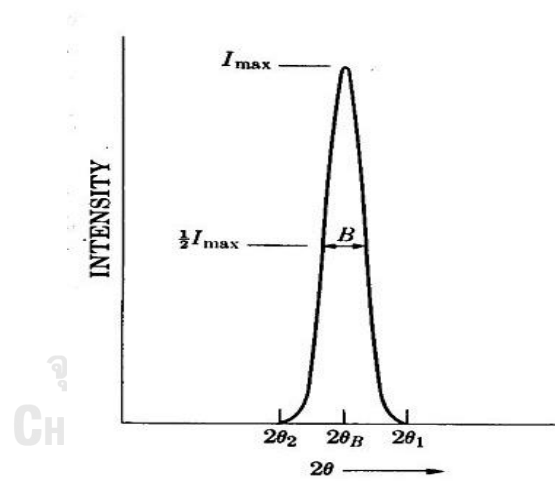


Figure F.1 Example of the full width at half maximum (FWHM)

APPENDIX G  
PUBLICATION

**G.1 International conference**

Dolrudee Jaruwat, Apiluck Eiad-ua, Worapon Kiatkittipong, Atthapon Srifa, Sumittra Charojrochkul and Suttichai Assabumrungrat. “Influence of parameter on the chemical activation of mesoporous carbon material derived from cattail leaves”, 3<sup>rd</sup> International Conference on Functional Materials and Chemical Engineering, December 15-17, 2019, Bangkok, Thailand





## REFERENCES

1. Mofijur, M., et al., *Role of biofuel and their binary (diesel–biodiesel) and ternary (ethanol–biodiesel–diesel) blends on internal combustion engines emission reduction*. Renewable and Sustainable Energy Reviews, 2016. **53**: p. 265-278.
2. Mahmudul, H.M., et al., *Production, characterization and performance of biodiesel as an alternative fuel in diesel engines – A review*. Renewable and Sustainable Energy Reviews, 2017. **72**: p. 497-509.
3. Habibullah, M., et al., *Potential of biodiesel as a renewable energy source in Bangladesh*. Renewable and Sustainable Energy Reviews, 2015. **50**: p. 819-834.
4. Lateef, F.A., et al., *Some physical properties and oxidative stability of biodiesel produced from oil seed crops*. Korean Journal of Chemical Engineering, 2014. **31**(5): p. 725-731.
5. Ruhul, M.A., et al., *Impact of fatty acid composition and physicochemical properties of Jatropha and Alexandrian laurel biodiesel blends: An analysis of performance and emission characteristics*. Journal of Cleaner Production, 2016. **133**: p. 1181-1189.
6. Borsotti, G.N.I., (IT), Capuzzi, Luigi (Novara (IT), IT), Digioia, Francesca (Barengo (NO), IT), *PROCESS FOR THE SELECTIVE HYDROGENATION OF VEGETABLE OILS*. 2016, NOVAMONT S.P.A (Novara, IT): United States.
7. Adu-Mensah, D., et al., *A review on partial hydrogenation of biodiesel and its influence on fuel properties*. Fuel, 2019. **251**: p. 660-668.
8. Rashidi, N.A. and S. Yusup, *An overview of activated carbons utilization for the post-combustion carbon dioxide capture*. Journal of CO2 Utilization, 2016. **13**: p. 1-16.
9. Ameen, M., et al., *Catalytic hydrodeoxygenation of triglycerides: An approach to clean diesel fuel production*. Renewable and Sustainable Energy Reviews, 2017. **80**: p. 1072-1088.
10. Sajjadi, B., A.A.A. Raman, and H. Arandiyan, *A comprehensive review on properties of edible and non-edible vegetable oil-based biodiesel*:

- Composition, specifications and prediction models. Renewable and Sustainable Energy Reviews*, 2016. **63**: p. 62-92.
11. Boateng, L., et al., *Coconut oil and palm oil's role in nutrition, health and national development: A review. Ghana medical journal*, 2016. **50**(3): p. 189-196.
  12. Mancini, A., et al., *Biological and Nutritional Properties of Palm Oil and Palmitic Acid: Effects on Health. Molecules (Basel, Switzerland)*, 2015. **20**: p. 17339-17361.
  13. Ulmasov, T., et al., *15 - High-Oleic, Low-Saturate Soybeans Offer a Sustainable and Nutritionally Enhanced Solution for Food Applications Requiring High Oil Stability*, in *Designing Soybeans for 21st Century Markets*, R.F. Wilson, Editor. 2012, AOCs Press. p. 277-295.
  14. Navarro Ferrando, M.Á., et al., *Response of ApoA-IV in pigs to long-term increased dietary oil intake and to the degree of unsaturation of the fatty acids. The British journal of nutrition*, 2004. **92**: p. 763-9.
  15. Mawatari, T., et al., *High Pressure Rheology of Environmentally Friendly Vegetable Oils. Tribology Letters*, 2013. **51**.
  16. Mahlia, T.M.I., et al., *Patent landscape review on biodiesel production: Technology updates. Renewable and Sustainable Energy Reviews*, 2020. **118**: p. 109526.
  17. Islam, M., et al., *A comprehensive review on biodiesel cold flow properties and oxidation stability along with their improvement processes. RSC Adv.*, 2015. **5**.
  18. Knothe, G. and K.R. Steidley, *The effect of metals and metal oxides on biodiesel oxidative stability from promotion to inhibition. Fuel Processing Technology*, 2018. **177**: p. 75-80.
  19. Kumar, N., *Oxidative stability of biodiesel: Causes, effects and prevention. Fuel*, 2017. **190**: p. 328-350.
  20. Sbihi, H.M., et al., *Study of oxidative stability and cold flow properties of Citrillus colocynthis oil and Camelus dromedaries fat biodiesel blends. Industrial Crops and Products*, 2018. **122**: p. 133-141.
  21. Van Gerpen, J.H. and B.B. He, *14 - Biodiesel and renewable diesel production*

- methods*, in *Advances in Biorefineries*, K. Waldron, Editor. 2014, Woodhead Publishing. p. 441-475.
22. Mofijur, M., et al., *Chapter Fourteen - Assessment of Physical, Chemical, and Tribological Properties of Different Biodiesel Fuels*, in *Clean Energy for Sustainable Development*, M.G. Rasul, A.k. Azad, and S.C. Sharma, Editors. 2017, Academic Press. p. 441-463.
  23. Mumtaz, M.W., et al., *Chapter Fifteen - Biodiesel Production Through Chemical and Biochemical Transesterification: Trends, Technicalities, and Future Perspectives*, in *Clean Energy for Sustainable Development*, M.G. Rasul, A.k. Azad, and S.C. Sharma, Editors. 2017, Academic Press. p. 465-485.
  24. Behr, A., A. Westfechtel, and J. Gomes, *Catalytic Processes for the Technical Use of Natural Fats and Oils*. Chemical Engineering & Technology, 2008. **31**: p. 700-714.
  25. Bello, C., et al., *Homogeneous catalytic hydrogenation of canola oil using a ruthenium catalyst*. Journal of the American Oil Chemists' Society, 1985. **62**(11): p. 1587-1592.
  26. Dijkstra, A., *Revisiting the formation of trans isomers during partial hydrogenation of triacylglycerol oils*. European Journal of Lipid Science and Technology - EUR J LIPID SCI TECHNOL, 2006. **108**: p. 249-264.
  27. Xinzhe, L., et al., *The effect of activation temperature on structure and properties of blue coke-based activated carbon by CO<sub>2</sub> activation*. Green Processing and Synthesis, 2019. **8**(1): p. 837-845.
  28. Tang, Z.-E., et al., *Synthesis of biomass as heterogeneous catalyst for application in biodiesel production: State of the art and fundamental review*. Renewable and Sustainable Energy Reviews, 2018. **92**: p. 235-253.
  29. Rand, D., *Understanding the functions of carbon in the negative active-mass of the lead-acid battery: A review of progress*. 2018.
  30. Contescu, C., et al., *Activated Carbons Derived from High-Temperature Pyrolysis of Lignocellulosic Biomass*. 2018. **4**.
  31. Marsh, H. and F. Rodríguez-Reinoso, *CHAPTER 9 - Production and Reference Material*, in *Activated Carbon*, H. Marsh and F. Rodríguez-Reinoso, Editors. 2006,

- Elsevier Science Ltd: Oxford. p. 454-508.
32. Liu, R.-L., et al., *Biomass-derived highly porous functional carbon fabricated by using a free-standing template for efficient removal of methylene blue*. *Bioresource Technology*, 2014. **154**: p. 138-147.
  33. Janaun, J. and N. Ellis, *Role of silica template in the preparation of sulfonated mesoporous carbon catalysts*. *Applied Catalysis A: General*, 2011. **394**(1): p. 25-31.
  34. Mohamad Nor, N., et al., *Synthesis of activated carbon from lignocellulosic biomass and its applications in air pollution control—a review*. *Journal of Environmental Chemical Engineering*, 2013. **1**(4): p. 658-666.
  35. Hernández-Montoya, V. and A. Bonilla-Petriciolet, *Lignocellulosic precursors used in the synthesis of activated carbon: characterization techniques and applications in the wastewater treatment*. 2012.
  36. Liu, Z., et al., *Production of solid biochar fuel from waste biomass by hydrothermal carbonization*. *Fuel*, 2013. **103**: p. 943-949.
  37. Reza, M.T., et al., *Review Article: Hydrothermal Carbonization of Biomass for Energy and Crop Production*. *Applied Bioenergy*, 2014. **1**.
  38. Reza, M.T., et al., *Hydrothermal carbonization of loblolly pine: reaction chemistry and water balance*. *Biomass Conversion and Biorefinery*, 2014. **4**(4): p. 311-321.
  39. Ngaosuwan, K., J.G. Goodwin, and P. Prasertdham, *A green sulfonated carbon-based catalyst derived from coffee residue for esterification*. *Renewable Energy*, 2016. **86**: p. 262-269.
  40. Härmas, M., et al., *Microporous–mesoporous carbons for energy storage synthesized by activation of carbonaceous material by zinc chloride, potassium hydroxide or mixture of them*. *Journal of Power Sources*, 2016. **326**: p. 624-634.
  41. Ludwinowicz, J. and M. Jaroniec, *Effect of activating agents on the development of microporosity in polymeric-based carbon for CO<sub>2</sub> adsorption*. *Carbon*, 2015. **94**: p. 673-679.
  42. Maneerung, T., et al., *Activated carbon derived from carbon residue from*

- biomass gasification and its application for dye adsorption: Kinetics, isotherms and thermodynamic studies*. Bioresource Technology, 2016. **200**: p. 350-359.
43. Reza, M.T., *Hydrothermal Carbonization of Lignocellulosic Biomass*. 2012: BiblioBazaar.
  44. Zdravkov, B.D., et al., *Pore classification in the characterization of porous materials: A perspective*. Central European Journal of Chemistry, 2007. **5**(2): p. 385-395.
  45. Donohue, M. and G.L. Aranovich, *Classification of Gibbs adsorption isotherms*. Advances in Colloid and Interface Science, 1998. **76**: p. 137-152.
  46. Na Rungsi, A., et al., *Influence of silica sources on structural property and activity of Pd-supported on mesoporous MCM-41 synthesized with an aid of microwave heating for partial hydrogenation of soybean methyl esters*. Applied Catalysis A: General, 2018. **563**: p. 80-90.
  47. Numwong, N., et al., *Effect of Support Acidic Properties on Sulfur Tolerance of Pd Catalysts for Partial Hydrogenation of Rapeseed Oil-Derived FAME*. Journal of the American Oil Chemists' Society, 2012. **89**(11): p. 2117-2120.
  48. Numwong, N., et al., *Partial hydrogenation of polyunsaturated fatty acid methyl esters over Pd/activated carbon: Effect of type of reactor*. Chemical Engineering Journal, 2012. **210**: p. 173-181.
  49. Jitjamnong, J., et al., *Catalytic Activity of Ni/SiO<sub>2</sub> Supported on Partial Hydrogenation of Biodiesel from Waste Cooking Oil*. 2018. **21**: p. 99-106.
  50. Cepeda, E.A., et al., *Selective hydrogenation of sunflower oil over Ni catalysts*. Korean Journal of Chemical Engineering, 2016. **33**(1): p. 80-89.
  51. Trasarti, A.F., et al., *Selective Hydrogenation of Soybean Oil on Copper Catalysts as a Tool Towards Improved Bioproducts*. Journal of the American Oil Chemical Society, 2012. **89**: p. 2245-2252.
  52. McArdle, S., et al., *Hydrogenation of sunflower oil over Pt-Ni bimetallic supported catalysts: Preparation, characterization and catalytic activity*. Applied Catalysis A: General, 2014. **474**: p. 78-86.
  53. Fernández, M.B., et al., *Hydrogenation of edible oil over Pd-Me/Al<sub>2</sub>O<sub>3</sub> catalysts (Me=Mo, V and Pb)*. Journal of Molecular Catalysis A: Chemical, 2005. **233**(1): p.

- 133-139.
54. Thunyaratchatanon, C., et al., *Influence of Mg modifier on cis-trans selectivity in partial hydrogenation of biodiesel using different metal types*. Applied Catalysis A: General, 2016. **520**: p. 170-177.
  55. Zhao, Y., et al., *Preparation of hydrogenated soybean oil of high oleic oil with supported catalysts*. Food Bioscience, 2018. **22**: p. 91-98.
  56. Ghouma, I., et al., *The Potential of Activated Carbon Made of Agro-Industrial Residues in NO<sub>x</sub> Immissions Abatement*. Energies, 2017. **10**: p. 1508.
  57. Yakout, S.M. and G. Sharaf El-Deen, *Characterization of activated carbon prepared by phosphoric acid activation of olive stones*. Arabian Journal of Chemistry, 2016. **9**: p. S1155-S1162.
  58. Jin, X.-J., Z.-M. Yu, and Y. Wu, *PREPARATION OF ACTIVATED CARBON FROM LIGNIN OBTAINED BY STRAW PULPING BY KOH AND K<sub>2</sub>CO<sub>3</sub> CHEMICAL ACTIVATION*. Cellulose Chemistry and Technology, 2012. **46**: p. 79-85.
  59. Namazi, A., D. Allen, and C. Jia, *Benefits of microwave heating method in production of activated carbon*. The Canadian Journal of Chemical Engineering, 2016. **94**.
  60. Acosta, R., et al., *Tetracycline adsorption onto activated carbons produced by KOH activation of tyre pyrolysis char*. Chemosphere, 2016. **149**: p. 168-176.
  61. Longprang, T., et al., *Influence of Base Additive on Nanoporous Carbon Materials via HTC for Catalyst Support*. International Journal of Materials Science and Engineering, 2019. **7**: p. 34-39.
  62. Jaruwat, D., et al., *Effects of hydrothermal temperature and time of hydrochar from Cattail leaves*. AIP Conference Proceedings, 2018. **2010**(1): p. 020016.
  63. García, R., et al., *Biomass proximate analysis using thermogravimetry*. Bioresource Technology, 2013. **139**: p. 1-4.
  64. Speight, J.G., *8 - Assessing fuels for gasification: analytical and quality control techniques for coal*, in *Gasification for Synthetic Fuel Production*, R. Luque and J.G. Speight, Editors. 2015, Woodhead Publishing. p. 175-198.
  65. Velázquez- Martí, B., et al., *Development of biomass fast proximate analysis by thermogravimetric scale*. Renewable Energy, 2018. **126**: p. 954-959.

66. Khandelwal, M. and T.N. Singh, *Prediction of macerals contents of Indian coals from proximate and ultimate analyses using artificial neural networks*. Fuel, 2010. **89**(5): p. 1101-1109.
67. Fu, F., L. Lin, and E. Xu, *4 - Functional pretreatments of natural raw materials*, in *Advanced High Strength Natural Fibre Composites in Construction*, M. Fan and F. Fu, Editors. 2017, Woodhead Publishing. p. 87-114.
68. Peak, D., *FOURIER TRANSFORM INFRARED SPECTROSCOPY*, in *Encyclopedia of Soils in the Environment*, D. Hillel, Editor. 2005, Elsevier: Oxford. p. 80-85.
69. Tanabe, T., et al., *Low temperature CO pulse adsorption for the determination of Pt particle size in a Pt/cerium-based oxide catalyst*. Applied Catalysis A: General, 2009. **370**(1): p. 108-113.
70. Karakaya, C. and O. Deutschmann, *A simple method for CO chemisorption studies under continuous flow: Adsorption and desorption behavior of Pt/Al<sub>2</sub>O<sub>3</sub> catalysts*. Applied Catalysis A: General, 2012. **445-446**: p. 221-230.
71. Başakçılardan Kabakcı, S. and S.S. Baran, *Hydrothermal carbonization of various lignocellulosics: Fuel characteristics of hydrochars and surface characteristics of activated hydrochars*. Waste Management, 2019. **100**: p. 259-268.
72. Wilk, M., et al., *Hydrothermal carbonization characteristics of sewage sludge and lignocellulosic biomass. A comparative study*. Biomass and Bioenergy, 2019. **120**: p. 166-175.
73. Guo, S., et al., *Characteristic evolution of hydrochar from hydrothermal carbonization of corn stalk*. Journal of Analytical and Applied Pyrolysis, 2015. **116**: p. 1-9.
74. Chai, I.V.K., X.Y. Lim, and T. Lee, *Creatinine adsorption by activated carbon fibre (ACF) derived from empty fruit bunch (EFB) fibre*. Journal of Engineering Science and Technology, 2017. **12**: p. 58-70.
75. Raymundo-Piñero, E., et al., *KOH and NaOH activation mechanisms of multiwalled carbon nanotubes with different structural organisation*. Carbon, 2005. **43**(4): p. 786-795.
76. Wang, L., et al., *High surface area porous carbons prepared from hydrochars by phosphoric acid activation*. Bioresource Technology, 2011. **102**(2): p. 1947-1950.

77. Chen, J., et al., *Preparation and Characterization of Activated Carbon from Hydrochar by Phosphoric Acid Activation and its Adsorption Performance in Prehydrolysis Liquor*. BioResources, 2017. **12**: p. 5928-5941.
78. Kaskel, S., *KOH activation of carbon-based materials for energy storage*. J. Mater. Chem., 2012. **22**: p. 23710-23725.
79. El-Hendawy, A.-N.A., *An insight into the KOH activation mechanism through the production of microporous activated carbon for the removal of Pb<sup>2+</sup> cations*. Applied Surface Science, 2009. **255**(6): p. 3723-3730.
80. Hassan, A.F. and A.M. Youssef, 2014. **15**.
81. Islam, M.A., et al., *Mesoporous activated carbon prepared from NaOH activation of rattan (*Lacosperma secundiflorum*) hydrochar for methylene blue removal*. Ecotoxicology and Environmental Safety, 2017. **138**: p. 279-285.
82. Le, M.C., et al., *The Impact of Ce-Zr Addition on Nickel Dispersion and Catalytic Behavior for CO<sub>2</sub> Methanation of Ni/AC Catalyst at Low Temperature*. Journal of Chemistry, 2017. **2017**: p. 4361056.
83. Yin, H., et al., *NiMo/Al<sub>2</sub>O<sub>3</sub> catalyst containing nano-sized zeolite Y for deep hydrodesulfurization and hydrodenitrogenation of diesel*. Journal of Natural Gas Chemistry, 2011. **20**(4): p. 441-448.



## VITA

**NAME** Dolrudee Jaruwat

**DATE OF BIRTH** 29 October 1995

**PLACE OF BIRTH** Samutprakarn

**INSTITUTIONS ATTENDED** Bachelor of Nanomaterial Engineering

**HOME ADDRESS** 1599/112 Taibanmai, Sukhumvit Rd., Taibanmai, Amphur Muang, Samutprakarn.

**PUBLICATION**

[1] Dolrudee Jaruwat, Parncheewa Udomsap, Nuwong Chollacoop and Apiluck Eiadua, Preparation of carbon supported catalyst from cattail leaves for biodiesel fuel upgrading application, Material Today Proceeding.

[2] Dolrudee Jaruwat, Parncheewa Udomsap, Nuwong Chollacoop, Masayoshi Fuji and Apiluck Eiad-ua, Effects of hydrothermal temperature and time of hydrochar from Cattail leaves, AIP conference Proceedings

[3] Dolrudee Jaruwat, Apiluck Eiad-ua, Worapon Kiatkittipong, Atthapon Srifa, Sumittra Charojrochkul and Suttichai Assabumrungrat, Influence of Parameter on The Chemical Activation of Mesoporous Carbon Material Derived from Cattail Leaves, Journal of Functional Materials and Chemical Engineering.

**AWARD RECEIVED** Dolrudee Jaruwat, Parncheewa Udomsap, Nuwong Chollacoop and Apiluck Eiadua, Preparation of carbon supported catalyst from cattail leaves for biodiesel fuel upgrading application, 1st MRS Thailand Intermediat Conference (Best Poster)